

Simulation Studies of Parametric Processes Associated with Ionospheric Stimulated Electromagnetic Radiation

Ahmed A. Hussein

Dissertation submitted to the Faculty of the Virginia Polytechnic Institute and
State University in partial fulfillment of the requirements for the degree of

Doctor of Philosophy
in
Electrical Engineering

Wayne A. Scales, Chair
Ioanis M. Beseieris
Gary S. Brown
Joe Huang
Sedki M. Riad
Yin Yan

September, 1997
Blacksburg, Virginia

Keywords: Ionospheric Modification, Plasma, Numerical Simulations
Copyright 1997, Ahmed A. Hussein

Simulation Studies of Parametric Processes Associated with Ionospheric Electromagnetic Radiation

Ahmed Hussein

(ABSTRACT)

Parametric instability processes are thought to produce Stimulated Electromagnetic Emissions (SEE) during ionospheric heating experiments. The phenomenon is primarily attributed to plasma turbulence excited by the high frequency HF heater in the altitude region where the pump frequency ω_0 is near the plasma upper hybrid frequency ω_{uh} . In this study, parametric instability processes thought to produce SEE are studied using theoretical and electrostatic Particle-In-Cell PIC simulation models. The simulation plasma is driven with a uniform oscillating electric field directed nearly perpendicular to the background geomagnetic field B to consider interactions when ω_{uh} is near electron cyclotron harmonics $n\Omega_{ce}$. The pump frequency and amplitude are varied to consider the effects on the simulation electric field power spectrum.

In this study, theoretical predictions and numerical simulations are used to study the three-wave decay instability process thought to be responsible for the generation of the down-shifted sidebands, the downshifted peak DP and the downshifted maximum DM. In particular, the lower hybrid decay instability LHDI and the ion cyclotron decay instability ICDI are studied in detail. The theory is used to provide the angular regime, with respect to the direction perpendicular to the magnetic field, at which the sidebands develop as well as the frequency and wavenumber regimes of both the LHDI and the ICDI. The effect of the temperature ratio T_e/T_i for both instabilities is discussed. A comparison between the theoretical predictions, the simulation electric field power spectrum and the experimental observations are presented in this study. Time evolution of both the LHDI and the ICDI is also investigated. The theoretical predictions are also used to investigate the cascading of the LHDI and the ICDI. The spectra show consistencies with the experimental observations.

A four-wave parametric decay instability process thought to be responsible for SEE broad up-shifted sideband spectral features is discussed as well. Many theoretical results are presented, in which the effect of stepping the heater frequency closer to the upper hybrid frequency on the angle of maximum growth θ_{max} , the growth rate γ and on both the frequency and wavenumber regimes of the four-wave process is investigated. The simulation electric field power spectrum showed a large amplitude up-shifted sideband and a much smaller amplitude down-shifted sideband, consistent with the experimental observations. Comparisons between the theoretical predictions, the simulation electric field power spectrum and the experimental observations are discussed in detail. The time evolution of the four-wave process is one important aspect that is also presented in this study. The development of density irregularities,

cavities and particle heating is also analyzed and investigated in this study.

Acknowledgments

I would like to express my deepest and sincere gratitude to my advisor, Dr. Wayne Scales for his valuable advice, guidance and encouragement during the course of this work. I sincerely appreciate his time and effort helping me during this research work. Without his support for the past several years, the accomplishment of this dissertation would have been impossible.

I would like to acknowledge Dr. Joe Huang for his valuable advise and useful suggestions and comments during the course of this research work.

I would like also to acknowledge Dr. I. Besieris, Dr. G. Brown, Dr. S. Riad and Dr. Y. Yan for serving in my advisory committee.

I would like to express my deepest appreciation and gratitude to my wife, Iman. I deeply acknowledge her for her constant support, encouragement and understanding.

Last and not least, I would like to express my deepest gratitude and my sincere love to my parents, my brothers and sister back home, for their love, continuous support and encouragement.

This work was supported by the Office of Naval Research ONR at Virginia Tech.

Contents

Contents	v
List of Figures	viii
List of Tables	xiii
1 Introduction	1
1.1 Objectives	2
2 Plasma parameters and SEE	3
2.1 Plasma oscillations and plasma frequency	5
2.2 Cyclotron frequency	6
2.3 Debye shielding	6
2.4 The upper hybrid frequency ω_{uh}	7
2.5 The Bernstein waves	7
2.6 Electrostatic ion waves perpendicular to B_0	7
2.7 Parametric instability	8
2.8 Production of beat currents	10
2.9 Cascading of electron waves	14
2.10 Stimulated Electromagnetic Emission (SEE)	14

2.10.1	Downshifted Maximum (DM)	15
2.10.2	Downshifted Peak (DP)	15
2.10.3	Broad Upshifted Maximum (BUM)	15
2.10.4	Broad Downshifted Maximum (BDM)	16
2.10.5	Continuum feature	16
2.10.6	Upshifted Maximum (UM)	16
2.10.7	Broad Symmetrical Structure (BSS)	16
3	Three-Wave Decay Instability	25
3.1	Theory	25
3.2	Simulation model	29
3.3	Simulation results	35
3.3.1	Simulation results for the LHDI	35
3.3.2	Cascading of the LHDI	43
3.4	Time evolution of the LHDI frequency spectrum	43
3.4.1	Simulation results and temperature effect on the ICDI	43
3.4.2	Cascading of the ICDI	49
3.5	Time evolution of the ICDI frequency spectrum	58
3.6	Summary	58
4	Four-Wave Decay Instability	63
4.1	Theory	63
4.2	Simulation Results	65
4.3	Time evolution of the four-wave decay frequency spectrum	73
4.4	Cyclotron damping	80
4.5	Summary	80

5	Summary and Conclusions	86
5.1	Future work	87
Appendix A Numerical calculations of the susceptibilities and solution of dispersion relations		89
A.1	89
A.2	91
A.3	93
Appendix B THREEWAVE.f program listing		94
Appendix C A description of the 1D numerical electrostatic simulation model		111
C.1	Simulation model	111
C.2	Approximations	113
C.2.1	The use of an artificial mass ratio in our simulations	113
C.2.2	The effect of electron-neutral collisions in the simulation of Stimulated Electromagnetic Emission SEE	113
Appendix D TRANSFORM.m program listing		115
Appendix E FOURWAVE subroutine		121
Appendix F INTERFEROGRAM.f program listing		124
References		129
Vita		131

List of Figures

2.1	A plot showing the variation of the ionospheric density with height [Collin, 1985].	4
2.2	A plot showing the geometry of an ion cyclotron wave propagating nearly at right angles to B_0 [Chen, 1984].	9
2.3	A parallelogram construction illustrating the parametric decay instability process [Chen, 1984].	11
2.4	A physical model for the generation of SEE.	17
2.5	A schematic diagram showing the cascading of the electron waves. . .	18
2.6	The different altitude regions in the generation of SEE.	19
2.7	Two results from experimental data showing the DM and the cascading of the DM.	20
2.8	Two results from experimental data showing the DP and the cascading of the DP.	21
2.9	Experimental data result showing the BUM and BDM features. . . .	22
2.10	A result from experimental data showing the continuum structure. . .	23
2.11	A result from experimental data showing the BSS.	24
3.1	A plot for the dispersion relation for both the lower hybrid wave for the cases (a) $\theta = 0.7\sqrt{m_e/m_i}$ (b) $\theta = 1.0\sqrt{m_e/m_i}$ and (c) $\theta = 1.4\sqrt{m_e/m_i}$ and for the ion cyclotron wave for the case $\theta = 4.0\sqrt{m_e/m_i}$	28
3.2	The dispersion relation for the upper hybrid and electron Bernstein modes and the location of the pump frequency ω_0 for the growth rate shown in Figure (3.3).	30

Figure 3.3	A plot of the growth rate γ vs θ in equation (1) for the case $\omega_0 = 3\Omega_{ce} + 3\omega_{lh}$ and for different temperature ratios T_e/T_i for the LHDI and the ICDI.	31
3.4	A plot of the maximum growth rate γ_{max} vs electron-ion temperature ratio T_e/T_i for the case $\omega_0 = 3\Omega_{ce} + 3\omega_{lh}$ for both ICDI and LHDI. . .	32
3.5	A plot of the growth rate γ vs ω in equation (3.1) for the case $\omega_0 = 3\Omega_{ce} + 3\omega_{lh}$ and for different temperature ratios T_e/T_i for both the ion cyclotron and lower hybrid modes.	33
3.6	A plot of the growth rate γ vs wavelength k in equation (3.1) for the case $\omega_0 = 3\Omega_{ce} + 3\omega_{lh}$ and for different temperature ratios T_e/T_i for both the ion cyclotron and lower hybrid modes.	34
3.7	A schematic 1D electrostatic PIC model for studying SEE parametric processes around electron gyroharmonic frequencies $n\Omega_{ce}$	36
3.8	Simulation result showing the total field energy in the simulation of the LHDI responsible for the DM.	37
3.9	Simulation result showing the kinetic energy for both the ions and electrons in the simulation of the LHDI responsible for the DM. . . .	38
3.10	Simulation result showing the down-shifted sideband for the case $\omega_0 = 3\Omega_{ce} + 3\omega_{lh}$ and $T_e/T_i = 1.0$ which corresponds to the growth rate calculation in Figure (3.3.b).	39
3.11	Simulation result showing the electron density and density irregularities in the simulation of the LHDI responsible for the DM.	40
3.12	Simulation result showing the ion density and density irregularities in the simulation of the LHDI responsible for the DM.	41
3.13	Simulation result showing the electric field strength in the simulation of the LHDI responsible for the DM.	42
3.14	The growth rate versus angle for investigating the cascading of the LHDI for the case $\omega_{uh} = 3\Omega_{ce}$	44
3.15	Simulation run showing the cascading of the down-shifted sideband for the case $\omega_0 = 3\Omega_{ce} + 4\omega_{lh}$ and $\omega_{uh} = 3\Omega_{ce}$	45
3.16	The simulation electric field energy history for the simulation results of the LHDI shown in Figure (3.17,18).	46

Figure 3.17	Three simulation results showing the simulation electric field power spectrum for the LHDI at different instants of time (a) $0 < \omega_{lh}t < 300$ (b) $300 \leq \omega_{lh}t < 600$ (c) $600 \leq \omega_{lh}t < 900$	47
3.18	Three simulation results showing the simulation electric field power spectrum for the LHDI at different instants of time (a) $0 < \omega_{lh}t < 60$ (b) $60 \leq \omega_{lh}t < 200$ (c) $200 \leq \omega_{lh}t < 330$	48
3.19	Three simulation runs showing the down-shifted sideband for the case $\omega_0 = 3\Omega_{ce} + 3\omega_{lh}$ and for (a) $T_e/T_i = 0.2$ (b) $T_e/T_i = 1.0$ (c) $T_e/T_i = 10.0$	50
3.20	Simulation result showing the electron density and density irregularities in the simulation of the ICDI responsible for the DP.	51
3.21	Simulation result showing the ion density and density irregularities in the simulation of the ICDI responsible for the DP.	52
3.22	Simulation result showing the electric field strength in the simulation of the ICDI responsible for the DP.	53
3.23	Simulation result showing the energy history of the kinetic energy for both the ions and electrons in the simulation of the ICDI responsible for the DP.	54
3.24	Simulation result showing the total field energy in the simulation of the ICDI responsible for the DP.	55
3.25	The growth rate versus angle for investigating the cascading of the ICDI for the case $\omega_{uh} = 3\Omega_{ce}$	56
3.26	Simulation run showing the cascading of the down-shifted sideband corresponding to the ICDI for the case $\omega_0 = 3\Omega_{ce} + 5\omega_{lh}$ and $\omega_{uh} = 3\Omega_{ce}$	57
3.27	The simulation electric field energy history for the simulation results of the ICDI shown in Figure (3.28,29).	60
3.28	Three simulation results showing the simulation electric field power spectrum for the ICDI at different instants of time (a) $0 < \omega_{lh}t < 1000$ (b) $1000 \leq \omega_{lh}t < 2000$	61
3.29	Three simulation results showing the simulation electric field power spectrum for the ICDI at different instants of time (a) $0 < \omega_{lh}t < 60$ (b) $60 \leq \omega_{lh}t < 200$ (c) $200 \leq \omega_{lh}t < 330$	62

Figure 4.1	A plot of the growth rate γ in equation (4.1) vs wavelength $k_{\perp}\rho_e$ and the dispersion relation for both the upper hybrid and the electron Bernstein modes for the case $\omega_0 = 4\Omega_{ce} + 3\omega_{lh}$, $\theta_{max} \simeq 3.0\sqrt{m_e/m_i}$ and $v_{osc}/v_{te} = 0.275$	66
4.2	A plot of showing the growth rate γ in equation (4.1) vs θ for the case $\omega_0 = 4\Omega_{ce} + 3\omega_{lh}$ and $v_{osc}/v_{te} = 0.275$	67
4.3	A plot of showing the growth rate γ in equation (4.1) vs ω for the case $\omega_0 = 4\Omega_{ce} + 3\omega_{lh}$, $\theta_{max} \simeq 3.07\sqrt{m_e/m_i}$ and $v_{osc}/v_{te} = 0.275$	68
4.4	A plot showing the variation of the growth rate γ as the pump frequency ω_0 is stepped close to the upper hybrid resonance frequency ω_{uh} for the case $\theta = \theta_{max}$ and $v_{osc}/v_{te} = 0.275$	69
4.5	A plot showing the variation of the angle of maximum growth θ_{max} as the pump frequency ω_0 is stepped close to the upper hybrid resonance frequency ω_{uh} for the case $v_{osc}/v_{te} = 0.275$	70
4.6	A plot showing the variation of the frequency at maximum growth rate as the pump frequency ω_0 is stepped close to the upper hybrid resonance frequency ω_{uh} for the case $\theta = \theta_{max}$ and $v_{osc}/v_{te} = 0.275$	71
4.7	A plot showing the variation of the wavenumber at maximum growth rate as the pump frequency ω_0 is stepped close to the upper hybrid resonance frequency ω_{uh} for the case $\theta = \theta_{max}$ and $v_{osc}/v_{te} = 0.275$	72
4.8	Simulation result showing the total field energy history in the simulation of the up-shifted sidebands.	74
4.9	Simulation result showing the kinetic energy history for both the ions and electrons in the simulation of the up-shifted sidebands.	75
4.10	Simulation electric field power spectrum showing the broad up-shifted spectral feature and the low frequency lower hybrid wave produced by the four-wave decay process described in Figure (4.1).	76
4.11	Simulation result showing the electron density and the development of density cavities in the simulation of the up-shifted sidebands.	77
4.12	Simulation result showing the ion density and the development of density cavities in the simulation of the up-shifted sidebands.	78
4.13	Simulation result showing the electric field strength in the simulation of the up-shifted sidebands.	79

Figure 4.14	An interferogram verifying the wavenumber matching for the four-wave interaction process responsible for the up-shifted sideband shown in Figure (4.10) in the interval $500 < \omega_{lh}t < 505$	82
4.15	Simulation electric field power spectra showing time evolution of the broad up-shifted and broad down-shifted spectral features at different time instants for the cases (a) $0 < \omega_{lh}t < 1000$ (b) $1000 \leq \omega_{lh}t < 2000$ (c) $2000 \leq \omega_{lh}t < 3000$	83
4.16	Simulation electric field power spectra showing time evolution of the broad up-shifted and broad down-shifted spectral features at different time instants for the cases (a) $0 < \omega_{lh}t < 300$ (b) $300 \leq \omega_{lh}t < 600$ (c) $600 \leq \omega_{lh}t < 900$	84
4.17	A result showing the time evolution of the peak amplitude of both the upper hybrid and electron Bernstein modes.	85
C.1	Discretization of the plasma length and naming of grids and particles.	111
C.2	A typical computational cycle for the particle simulation model. . . .	112

List of Tables

2.1 Classification of layers in the ionosphere. 5

Chapter 1

Introduction

The interaction of electromagnetic waves with the ionosphere has been an active research area since the trans-Atlantic experiment by Marconi in 1901. Evidence of ionospheric modification by a powerful radio wave was first observed in 1933 when a powerful transmitting station in Luxemburg was found to modulate signals transmitted from Switzerland to Holand. Baily and Martyn proposed that the signal from the Luxemburg station had increased the ionosphere electron temperature and thus had modulated the radio wave absorption. Since that time, there has been a growing interest in “heating” the ionosphere with high power radio waves.

In the past two decades, a number of heating facilities have been built in Europe, Russia and the United States to study the remote interaction of high frequency electromagnetic waves with the ionospheric plasma. Some of these heating facilities are HIPAS facility in Alaska, the one in Tromsø Norway and in Arecibo, Peurto Rico. The location of these heating facilities depends on the orientation of the Earth’s geomagnetic field. Current topics of interest in ionospheric modification research include such diverse aspects as modification of polar electrojet and ELF/VLF generation, hot electrons and artificial airglow emissions, large scale density and temperature modifications and generation of electrostatic waves, parametric instabilities and production of small scale density irregularities.

Another interesting phenomenon in ionospheric modification is the Stimulated Electromagnetic Emission (SEE). During heating experiments near Tromsø, Norway, it was discovered that when a powerful O-mode electromagnetic pump wave, which has a frequency near the harmonics of electron cyclotron frequency $n\Omega_{ce}$ is injected into the ionosphere from a ground station, secondary electromagnetic waves are generated and can be detected on the ground [Thidé 1982]. These electromagnetic waves have frequencies that are in a relatively small bandwidth around the pump wave frequency. Under varying pump wave and ionospheric conditions, these waves may be at

frequencies above or below the pump frequency. Some of the important SEE features that exhibit down-shifted sidebands are the Downshifted Maximum (DM) and the Downshifted Peak (DP). Some of the up-shifted sidebands are the Broad Upshifted Maximum (BUM) and the Upshifted Maximum (UM). Another feature that exhibits a symmetrical structure is the Broad Symmetrical Structure (BSS). The continuum feature is one important feature that will be discussed later.

1.1 Objectives

In this work we study some of proposed processes associated with SEE generation using particle in cell (PIC) simulation models. The PIC simulation model was used in this study since it includes kinetic modes such as Bernstein modes which are thought to play an important role in producing SEE. It also allows for detailed studying of nonlinear evolution. The emphasis is on DM, DP and the BUM features. Although numerical simulations will ultimately provide important contributions to the understanding of nonlinear processes that are thought to produce SEE and bridge the gap between theoretical development and experimental observations, there have been few studies in the past [*Hussein and Scales 1997* and references therein]. Our emphasis here will be to study the electrostatic parametric processes that ultimately produce currents that radiate as SEE.

The study investigates the effect of varying different plasma parameters that might affect the parametric instability. These parameters include the temperature effect T_e/T_i , the effect of varying the electron cyclotron harmonic $n\Omega_{ce}$ and the effect of varying the pump frequency on the instability process. It also involves using the linear theory predictions which were very useful in providing us with a qualitative information on different physical processes. The theory predictions also proved to be very useful and accurate in guiding the simulations conducted in this research. The dissertation is arranged as follows. This first chapter is an introduction to the study under investigation and our research objectives. The second chapter is an overview on important plasma parameters and SEE. Next chapter discusses the three-wave processes responsible for the down-shifted sidebands. Chapter four discusses the four-wave interaction process responsible for the up-shifted sidebands. Finally, summary and conclusions are discussed.

Chapter 2

Plasma parameters and SEE

The classification of the Earth's upper atmosphere can be categorized into many categories, temperature regime (troposphere, mesosphere, ...), chemical composition regimes (homosphere, heterosphere), ionization regimes (ionosphere, magnetosphere), and dynamics/mixing regimes (barosphere, exosphere).

All of these classification schemes divide the atmosphere into different regions depending on the altitude. Our focus in this work is on the ionization layer known as the ionosphere shown in Figure 2.1. At high altitudes the radiation from the sun causes a considerable amount of photoionization of the upper atmosphere. This results in free electrons and free ions which tend to recombine. In the ionosphere, the recombination of ions and electrons is slow due to low gas densities. Thus, the ionosphere is a region characterized by a high density concentration of both free electrons and ions. In general, any region that has the same characterization is classified as a plasma.

A plasma is often considered as a state of matter. At low temperatures collisions between atoms are rare, and these collisions do not have enough energy to ionize one or both atoms. However, as a gas heats up the number of collisions between atoms, with energy sufficient enough to ionize the atoms, increases. At a certain point the number of ionized atoms will increase enough that there is an abrupt change in the ratio between ionized and neutral atoms. At this point we are no longer talking about a gas, but a plasma. It is possible for a plasma to heat up enough that the number of ionized atoms will exceed the number of neutral atoms, making the plasma fully ionized.

A plasma can also be considered a quasineutral gas of charged and neutral particles which exhibits a collective behavior.

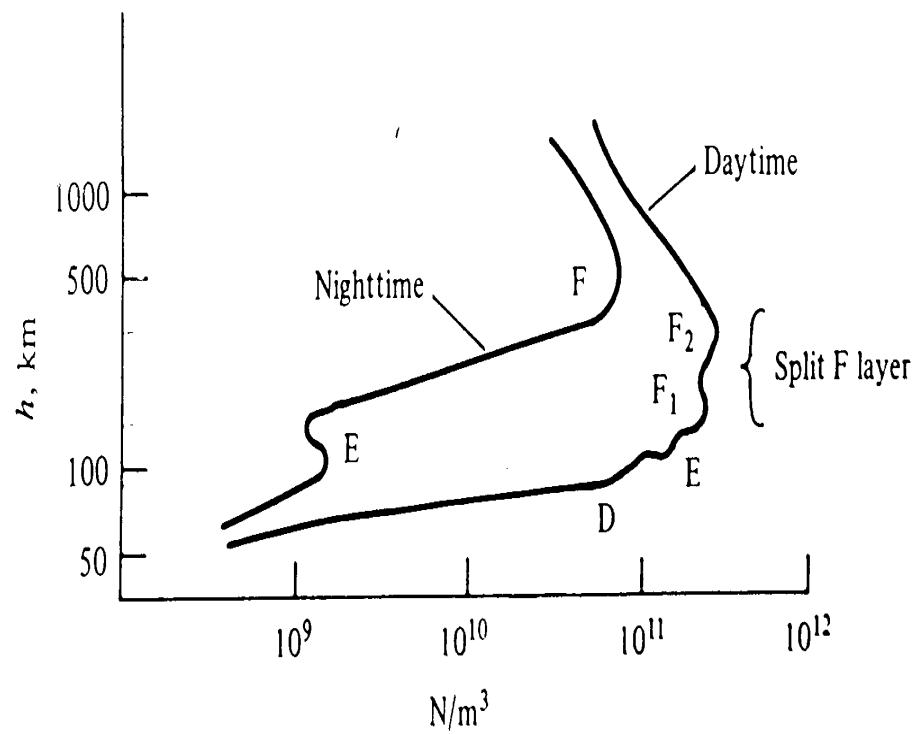


Figure 2.1: A plot showing the variation of the ionospheric density with height [Collin, 1985].

Table 2.1: Classification of layers in the ionosphere.

Ionospheric Layer	Altitude	Electron density
D	60-90 km	$10^8 - 10^{10} \text{ m}^{-3}$
E	105-160 km	several 10^{11} m^{-3}
F1	168-180 km	several $10^{11} - 10^{12} \text{ m}^{-3}$
F2	maximum variable around 300 km	up to several 10^{12} m^{-3}

The ionosphere, being a plasma and a conducting medium, both propagates and reflects radio waves, depending on frequency; thus, allowing for long distance radio communication.

The ionosphere is classified into vertical regions. This vertical structure is continuously changing, and varies from day to night, with the seasons of the year, and with latitude. The ionospheric layers are summarized in Table 2.1.

The E and F layers are the most important layers for radio communications in the frequency range of 3 to 30 MHz. Anything above 40 MHz is able to penetrate through the ionosphere. In the D region, only waves of 2 MHz and below are reflected. This is because the D region has a much lower electron density than the other layers. The D region also has a much larger collision frequency, due to a high neutral density.

Understanding the development of irregularities in the plasma is one of the most active areas of ionospheric research. There are many physical processes that can produce irregularities. One set of physical processes that we are interested in are plasma instabilities. There are several different classifications of plasma instabilities, but all of them are caused by waves produced by free energy in the ionosphere.

In this chapter we shall discuss the important concepts in plasma and its physical parameters.

2.1 Plasma oscillations and plasma frequency

If the electrons in plasma are displaced from a uniform background of ions, electric fields will be built up in such a direction as to restore the neutrality of the plasma by pulling the electrons back to their original positions. Because of their inertia, the electrons will over shoot and oscillate around their equilibrium positions with a frequency known as the plasma frequency ω_p . Their oscillations are so fast such that the massive ions may be assumed fixed. The plasma frequency is given by the

expression:

$$\omega_p^2 = \frac{q^2 n_0}{m \epsilon_0} \quad (2.1)$$

where, ω_p is the plasma frequency, q, n_0, m are the charge, charge density and the mass of the species respectively, and ϵ_0 is the permittivity of free space.

2.2 Cyclotron frequency

If a magnetic field is applied on a charged particle, the particle will experience a cyclotron gyration with a frequency known as the cyclotron frequency Ω_c . The cyclotron frequency is given by:

$$\Omega_c = \frac{qB}{m} \quad (2.2)$$

where, Ω_c is the cyclotron frequency, q, m are the charge and mass of the species respectively, and B is the applied magnetic field strength.

2.3 Debye shielding

A fundamental characteristic of the behavior of the plasma is its ability to shield out electric potentials that are applied to it. Suppose an electric field is applied into a plasma by putting two charged metal surfaces connected to a battery. The charged surfaces would attract potentials of opposite charges and almost immediately a cloud of ions will surround the negatively charged surface and a cloud of electrons will surround the positively charged surface. If the plasma were cold and there were no thermal motions, there would be just as many charges in the cloud as on the surface, and the shielding would be perfect. No electric field in this case would be present in the body of the plasma outside the cloud. On the other hand, if the temperature is finite, the particles that are at the edge of the cloud, where weak electric field is present, would have enough thermal energy to escape from the electrostatic potential well. The edge of the cloud occurs at the radius where the potential energy is approximately equal to the thermal energy KT , where K is Boltzman's constant and T is the temperature of the species, of the particles, and the shielding is not complete. Potentials of the order KT/q can leak into the plasma and cause a finite electric field

to exist [Chen, 1984]. A measure of the plasma shielding is called the Debye length λ_D which is given by :

$$\lambda_D = \sqrt{\frac{\epsilon_0 K T_e}{n q_e^2}} \quad (2.3)$$

which is a measure of the shielding distance. Note that describing the plasma as a quasineutral gas means that its neutral enough to assume $n_i = n_e = n$ where n is the plasma density.

2.4 The upper hybrid frequency ω_{uh}

Assuming high frequency electrostatic electron oscillations propagating at right angles to the background geomagnetic field. These electrostatic electron waves across B will oscillate with the frequency called the upper hybrid frequency, ω_{uh} . The upper hybrid frequency is given by

$$\omega_{uh}^2 = \omega_{pe}^2 + \Omega_{ce}^2 \quad (2.4)$$

where, ω_{uh} is the upper hybrid frequency, ω_{pe} is the electron plasma frequency, and Ω_{ce} is the electron cyclotron frequency. Note that those are different oscillations than those along B which are the usual plasma oscillations with $\omega = \omega_p$.

2.5 The Bernstein waves

These are electrostatic waves propagating at right angles to B at harmonics of the cyclotron frequency, $n\Omega_c$.

2.6 Electrostatic ion waves perpendicular to B_0

Assume k , the wave vector, is almost perpendicular to the background magnetic field B_0 . Assume also an infinite plasma in equilibrium with uniform density, n_0 and magnetic field B_0 . Also the assumption of cold ions is considered, i.e $T_i=0$. The geometry is shown in Figure 2.2. The angle $\pi/2 - \theta$ is taken to be so small that we may take $E = E_1 \hat{x}$ as far as ions are concerned. For the electrons, however it makes a

great difference whether $\pi/2 - \theta$ is zero or small and finite. The electrons have small Larmor radii that they cannot move in the x-direction to preserve charge neutrality; all that the E field does is make them drift back and forth in the y direction. If θ is not exactly $\pi/2$, the electrons can move along the dashed line (along B_0) to carry charge from negative to positive regions in the wave and carry out Debye shielding. The ions cannot do this effectively because their inertia prevents them from moving such a long distance in a wave period. This critical angle $\pi/2 - \theta$ is proportional to the ratio of ions to electrons thermal velocity which is proportional to $\sqrt{m_e/m_i}$. Considering the plasma approximation $n_i = n_e$, the dispersion equation of the ion cyclotron waves is obtained [Chen, 1984], which is given by:

$$\omega^2 = \Omega_{ci}^2 + k^2 v_s^2 \quad (2.5)$$

where, Ω_{ci} is the ion cyclotron frequency, k is the wave number, v_s is the electron oscillating velocity.

Now, consider the case with θ is exactly equal to $\pi/2$, and the electrons are not allowed to preserve their charge neutrality by flowing along the lines of force. Assuming also that the electron mass is finite and considering the plasma approximation $n_i = n_e$, we obtain the frequency called the lower hybrid frequency ω_{lh} [Chen, 1984] which is given by

$$\omega_{lh} \equiv \sqrt{\Omega_{ci}\Omega_{ce}} \quad (2.6)$$

where Ω_{ci} and Ω_{ce} are the ion cyclotron and electron cyclotron frequencies respectively. Note that the lower hybrid oscillations are only observed when θ is very close to $\pi/2$.

2.7 Parametric instability

Ion density fluctuations may couple an electromagnetic wave into an electron plasma wave to give us an electric field \tilde{E} . In turn, the electron plasma wave beats with the electromagnetic wave to generate a spatial variation in the electric field intensity which can enhance the ion density fluctuations via the ponderomotive force. Hence, a feedback loop is formed and depending on the pump amplitude, instability can result. Such instability is called parametric instability, with the parameter being the wave's amplitude. Note that the spatially varying electric field E_0 which is re-

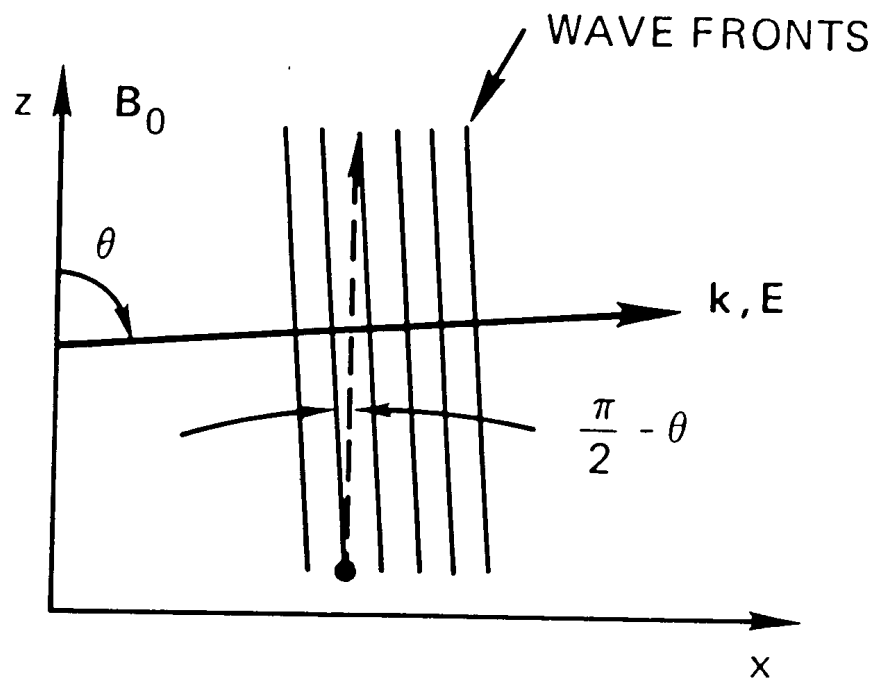


Figure 2.2: A plot showing the geometry of an ion cyclotron wave propagating nearly at right angles to B_0 [Chen, 1984].

sulting from beating of two waves requires a two-wave number matching to produce sustaining instability, the condition is

$$k_0 = k_i + k_s \quad (2.7)$$

where the scripts “0,” “i” and “s” stand for the pump, idler and the signal respectively. In the SEE problem, the electromagnetic wave is the pump, the electron plasma wave is the idler, and E_0 is the signal. The wave number matching condition is equivalent to conservation of momentum. However, the parametric instability has to satisfy the conservation of energy to take place. This translates into the frequency matching condition

$$\omega_0 = \omega_i + \omega_s \quad (2.8)$$

Note also that the instability can occur only when the pump amplitude is above a critical value in order to maintain the feedback growth. Figure 2.3 shows the parallelogram construction for the parametric decay instability process. Here, (ω_0, k_0) is an incident electromagnetic wave of large phase velocity ($\omega_0/k_0 \simeq c$). It excites an electron wave and an ion wave moving in opposite directions. Since $|k_0|$ is small we have $|k_1| \simeq -|k_2|$ and $\omega_0 = \omega_1 + \omega_2$ for this instability.

2.8 Production of beat currents

An electrostatic particle-in-cell simulation model was used to investigate the Stimulated Electromagnetic Emission SEE in our study. To explain the validity of this approach we need to discuss the generation mechanism of SEE. Recent theoretical and simulation studies have predicted that the development of frequency sidebands in the SEE spectrum are produced by interactions between electrostatic waves which are scattered into electromagnetic waves to produce the observed stimulated waves [Zhou *et al.*, 1994, Mjølhus *et al.*, 1994; Goodman *et al.*, 1995]. A theoretical model for SEE generation is shown in Figure (2.4). When an o-mode heater wave is launched into the ionosphere and at the altitude region of the upper hybrid resonance layer, the pump wave excites electrostatic waves at this altitude. These electrostatic waves parametrically decay into low frequency waves and electrostatic high frequency HF sidebands. The conversion from electromagnetic wave (pump wave) into electrostatic waves is called mode conversion and in this case it is called ”direct conversion”. Another mechanism that could also produce these electrostatic waves is the thermal oscillating two stream instability OTSI [Huang and Kuo 1994; Lee and Kuo 1983; Dysthe *et al.* 1982]. The crucial part in the direct conversion is the pre-existing short

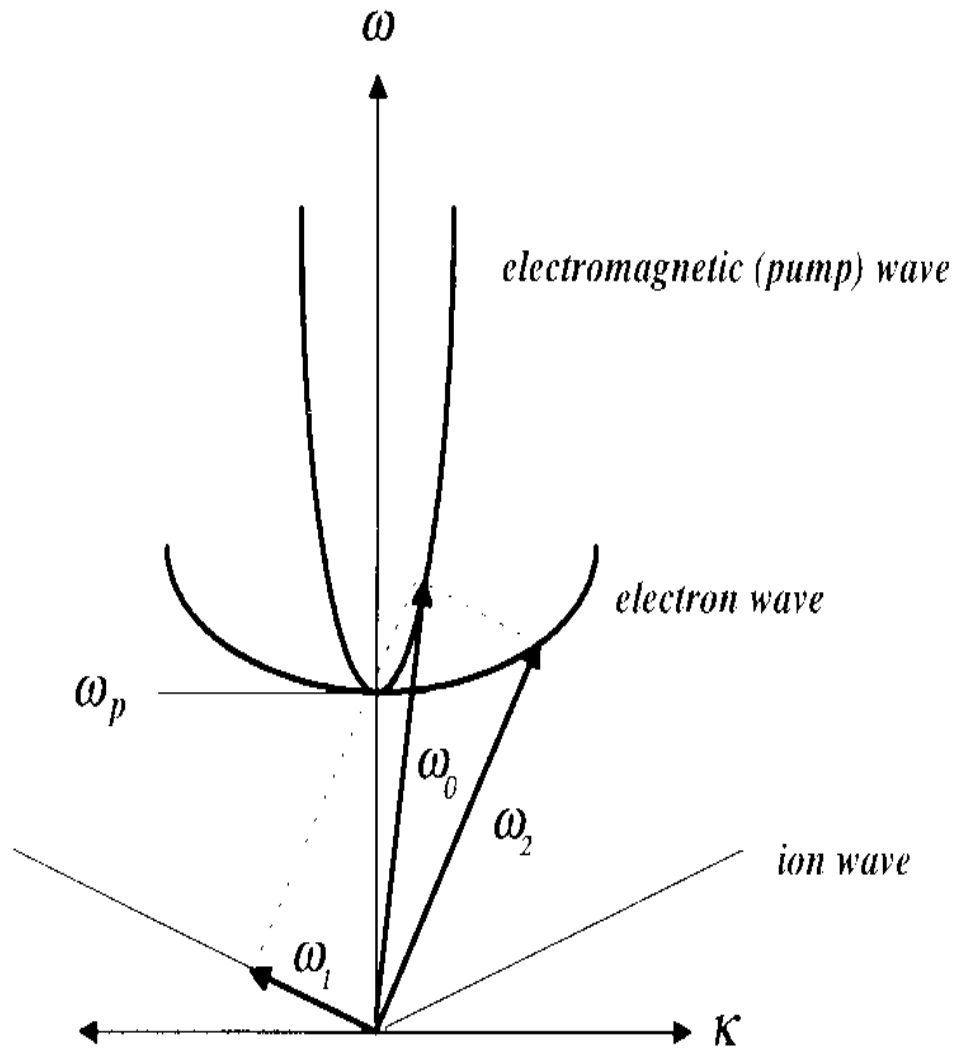


Figure 2.3: A parallelogram construction illustrating the parametric decay instability process [Chen, 1984].

scale ($\sim 1\text{m}$) field aligned density irregularities. Irregularities of a variety of scale sizes (varying over many orders of magnitude) exist in the different regions of the ionosphere. They arise from a number of sources such as wind, gravity, etc. The physical process of the direct conversion is as follows [Antani 1991]. The incident o-wave induces oscillating electron drift in the upper-hybrid resonance layer. This induced electron velocity mixes with the pre-existing density irregularities to generate a source current that plays the role of an in-situ antenna radiating the excited upper hybrid wave

$$J_s = -e \tilde{n}_{el} v_{eh} \quad (2.9)$$

where e is the electron charge, \tilde{n}_{el} is the low frequency electrons density fluctuation and v_{eh} is the high frequency pump induced velocity (oscillating velocity) which is given by

$$v_{eh} = v_0 \exp(i(k_x x - k_z z - \omega_0 t)) \quad (2.10)$$

The low frequency density irregularities produced by the parametric instability propagate in either the forward or backward direction. The low frequency forward propagating density irregularities are given by

$$\delta_{ne}^+ = \delta_{n0} \exp(i(k_x x - \omega_l t)) + c.c. \quad (2.11)$$

where $c.c.$ denotes the complex conjugate. These low frequency forward propagating density irregularities mix with the high frequency electron oscillations to produce a current responsible for producing the down-shifted frequency

$$J^+ \simeq J_0 \exp(i(-k_z z - (\omega_0 - \omega_l)t)) \quad (2.12)$$

The low frequency backwards propagating density irregularities are given by

$$\delta_{ne}^- = \delta_{n0} \exp(i(k_x x + \omega_l t)) + c.c. \quad (2.13)$$

These low frequency backwards propagating density irregularities mix with the high frequency electron oscillations to produce a backward propagating beat current which is responsible for producing the up-shifted frequency

$$J^- \simeq J_0 \exp(i(-k_z z - (\omega_0 + \omega_l)t)) \quad (2.14)$$

These beat currents are responsible for the propagation of the up-shifted and the down-shifted frequencies seen on the ground as SEE. This process is called nonlinear scattering. This process occurs whenever the following frequency and wave matching conditions are satisfied

$$\omega_0 = \omega_{uh} + \omega_n \quad (2.15)$$

$$k_0 = k_{uh} + k_n \quad (2.16)$$

where the subscripts "0" and "n" refer to the pump and the irregularities respectively. The direct conversion process differs from the parametric process in that it has no threshold field power requirement and also it leads to a linear growth that is linear in time. Note that since the direct conversion relies on these irregularities in the ionosphere, which vary with time and position, we can expect that the direct conversion process is not a static process but a process with high degree of fluctuations.

So, from the above discussion, the generation of SEE is through two steps the first and the most important step is the mode conversion "forward conversion", where the electromagnetic o-mode pump wave decays into electrostatic sidebands and low frequency decay mode at the altitude region of the upper hybrid resonance layer. The second step is the "backward conversion" from the electrostatic sideband waves into radiated electromagnetic waves radiated by the currents back to the ground as SEE. So, the reason for using a pure electrostatic model to study SEE is that we are looking at the electrostatic sidebands developed in the altitude region of upper hybrid resonance layer. In this region, most of the physical processes responsible for the generation of the SEE sidebands take place before it is scattered from the field aligned density irregularities and radiated to the ground through backward conversion and seen as SEE.

In essence of the above, we have chosen to use a purely electrostatic rather than a fully electromagnetic model to study SEE. It is also worth mentioning that a pure electrostatic model is computationally more feasible and consequently provides more resolution of the electrostatic parametric processes that produce SEE.

2.9 Cascading of electron waves

During ionospheric heating experiments, it was found that the down-shifted side bands can appear in a cascading or multiple structure [Fejer and Kuo, 1973; Perkins et al., 1974]. The mechanism is attributed to the fact that ω_0 might decay into electrostatic electron waves and low frequency ion waves. These electrostatic upper hybrid/electron Bernstein sidebands may act as a secondary pump that would in turn decay into a second sideband and thereby causing the multiple sideband feature. This mechanism is demonstrated in Figure (2.5).

2.10 Stimulated Electromagnetic Emission (SEE)

Many phenomenon attributed to wave-wave interaction have been observed during ionospheric heating experiments. Stimulated Electromagnetic Emission SEE is a wave-wave process thought to be produced by parametric instabilities. The waves include upper hybrid, lower hybrid, and ion cyclotron waves. The SEE spectrum exhibits sidebands that are up-shifted and down-shifted from the pump wave within roughly about 10 KHz bandwidth. A physical model for the generation mechanism of the SEE is shown in Figure (2.4).

The SEE is a very important diagnostic tool for studying parametric instabilities and other nonlinear physical processes that may occur around the heated region. It was noted that the spectrum from SEE may be used to measure the electric field strength in the heated region. The SEE spectrum was used in many experimental observations to measure the magnitude of the background magnetic field. The results show that the SEE can be a very important diagnostic tool and it is also considered a fundamental plasma phenomenon. A physical model for the SEE and the important altitude regions is shown in Figure (2.6).

The classification of SEE spectral features and the description of their generation through parametric decay instability processes was provided by *Stubbe et al.* [1984]. The SEE spectral sidebands were found to depend on a number of ionospheric parameters in addition to the pump wave. It was also postulated that the sidebands in the SEE spectrum should develop in the altitude region where ω_0 is near the plasma upper hybrid frequency ω_{uh} . It was also found that this spectrum is dependent on the proximity of ω_0 to the harmonics of the electron cyclotron frequency $n\Omega_{ce}$.

Some of the important SEE spectral features sidebands which extend above and below the pump frequency by multiples of the lower hybrid frequency or less than a lower hybrid frequency are described in the following subsections.

2.10.1 Downshifted Maximum (DM)

The downshifted maximum DM is one of the prominent SEE spectral features. This sideband in the SEE spectrum has a frequency shift below the pump frequency approximately equal to the local plasma lower hybrid frequency ω_{lh} . The theoretical studies of the DM considered the generation through the parametric decay of the electromagnetic pump wave into upper hybrid waves. The upper hybrid waves either decay into a lower hybrid wave and an O-mode wave [*Murtaza and Shukla, 1984, Stenflo and Shukla, 1992, Leyser, 1991*] or decay into a lower hybrid wave and an electrostatic upper hybrid electron Bernstein wave which is scattered by field-aligned irregularities into electromagnetic waves that are observed on the ground [*Zhou et al., 1994*]. Some of the experimental results showing the DM and the cascading structure of the DM are shown in Figure (2.7).

2.10.2 Downshifted Peak (DP)

Another SEE spectral feature is the downshifted peak DP. The DP is a downshifted sideband which is usually observed when the pump frequency is very close to the third harmonic of the electron cyclotron frequency $3\Omega_{ce}$. Its offset frequency from the pump is about 2 KHz. It was postulated by *Huang and Kuo [1995]* that the generation mechanism for the DP feature is through parametric decay of an electron Bernstein pump wave into an electron Bernstein sideband wave and a nearly perpendicularly propagating ion acoustic or electrostatic ion cyclotron decay wave. Some experimental results are shown in Figure (2.8). The figure shows the downshifted peak extending below ω_0 by a factor less than a lower hybrid frequency ω_{lh} . It was also noted that the DP may appear in a cascading structure when the upper hybrid resonance frequency is equal to third electron cyclotron harmonic $\omega_{uh} = 3\Omega_{ce}$ (double resonance) and ω_0 is very close to $3\Omega_{ce}$. An experimental result showing the cascading of the DP is also shown in Figure (2.8).

2.10.3 Broad Upshifted Maximum (BUM)

The most important up-shifted feature in the SEE spectrum is the broad upshifted maximum BUM only seen when ω_0 is above $n\Omega_{ce}$. It was noted by *Leyser et al [1989]* that the BUM feature could be generated through a four-wave interaction process involving two pump photons or upper hybrid plasmons, a decay mode at $n\Omega_{ce}$, and the stimulated radiation at ω_{BUM} . When the heater frequency ω_0 is above an electron cyclotron harmonic $n\Omega_{ce}$, frequency up-shifted upper hybrid waves and frequency down-shifted electron Bernstein waves can be excited above the upper

hybrid resonance layer via the considered four-wave process. *Huang and Kuo* [1994] have proposed that the BUM is produced in the region where the pump frequency is about the mean of the upper hybrid wave frequency and the electron Bernstein wave frequency. A low frequency electrostatic oscillation in the frequency regime of ω_{lh} is also generated. Figure (2.9) shows the BUM during a heating experiment.

2.10.4 Broad Downshifted Maximum (BDM)

It is a broad down-shifted sideband which is often observed accompanying the presence of the BUM. It has a broad frequency spread like the BUM with a smaller amplitude. Figure (2.9) shows the BDM during a heating experiment.

2.10.5 Continuum feature

It is an asymmetric feature, with more energy on the down-shifted side. The width of the down shifted portion of the continuum is strongly variable, ranging from a few KHz, Narrow Continuum NC, to as much as 100 KHz, Broad Continuum BC. A result from experimental data for the continuum feature is shown in Figure (2.10).

2.10.6 Upshifted Maximum (UM)

It is an up-shifted sideband mostly seen with the DM. The frequency shift of the UM from the pump frequency is about 5 to 9 KHz. This feature is much weaker than the DM. Figure (2.11) shows the UM during a heating experiment.

2.10.7 Broad Symmetrical Structure (BSS)

It is a symmetrical structure composed of two equal sidebands symmetrical about the pump frequency by about 15 to 30 KHz. The BSS has the narrowest pump frequency range of existence among all the primary features and occurs for pump frequencies in the range of 40 KHz near $3 f_{ce}$, which is very similar to the DP feature. An experimental result for the BSS is shown in Figure (2.11).

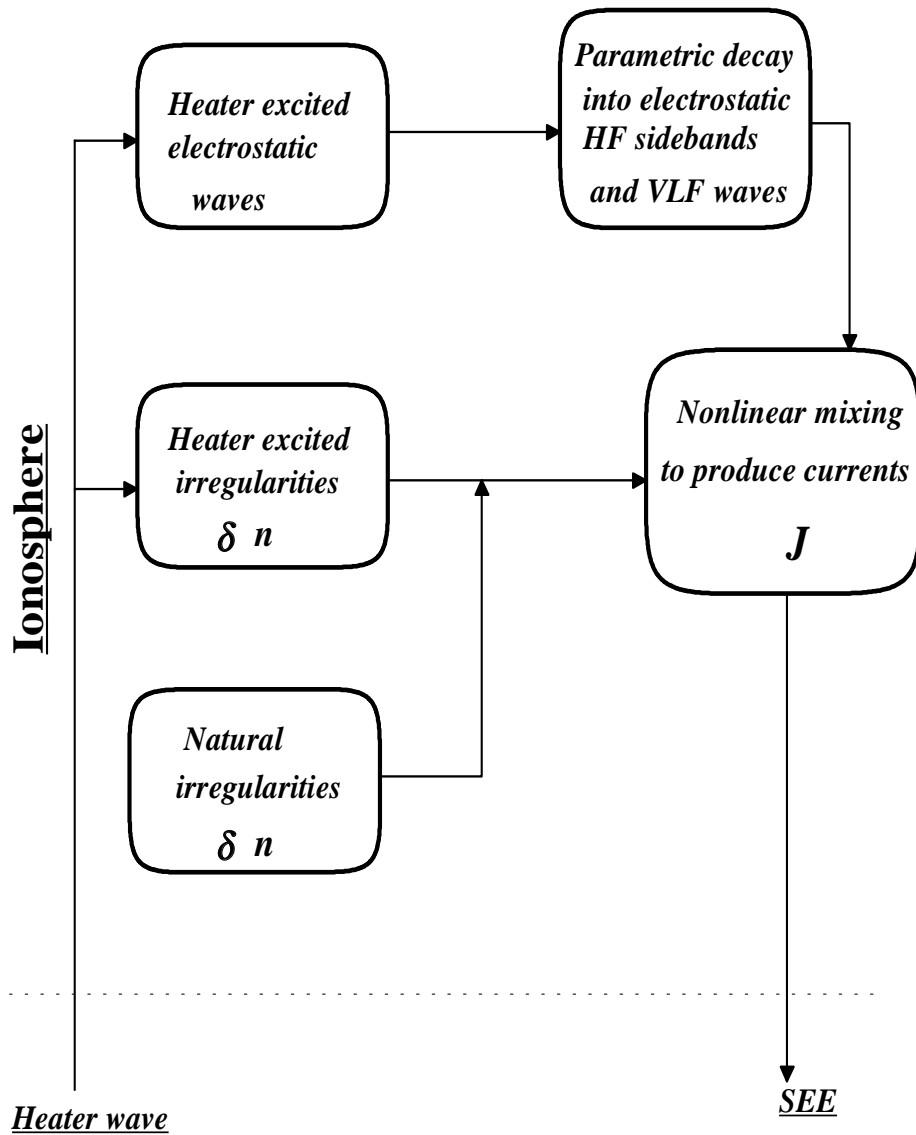


Figure 2.4: A physical model for the generation of SEE.

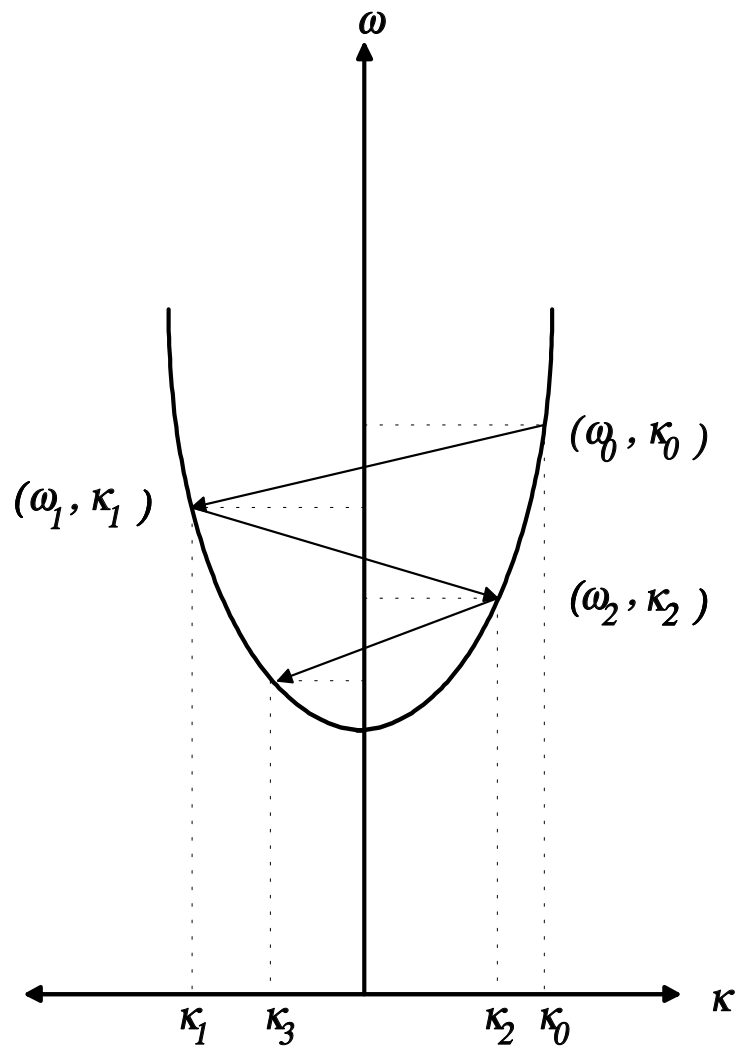


Figure 2.5: A schematic diagram showing the cascading of the electron waves.

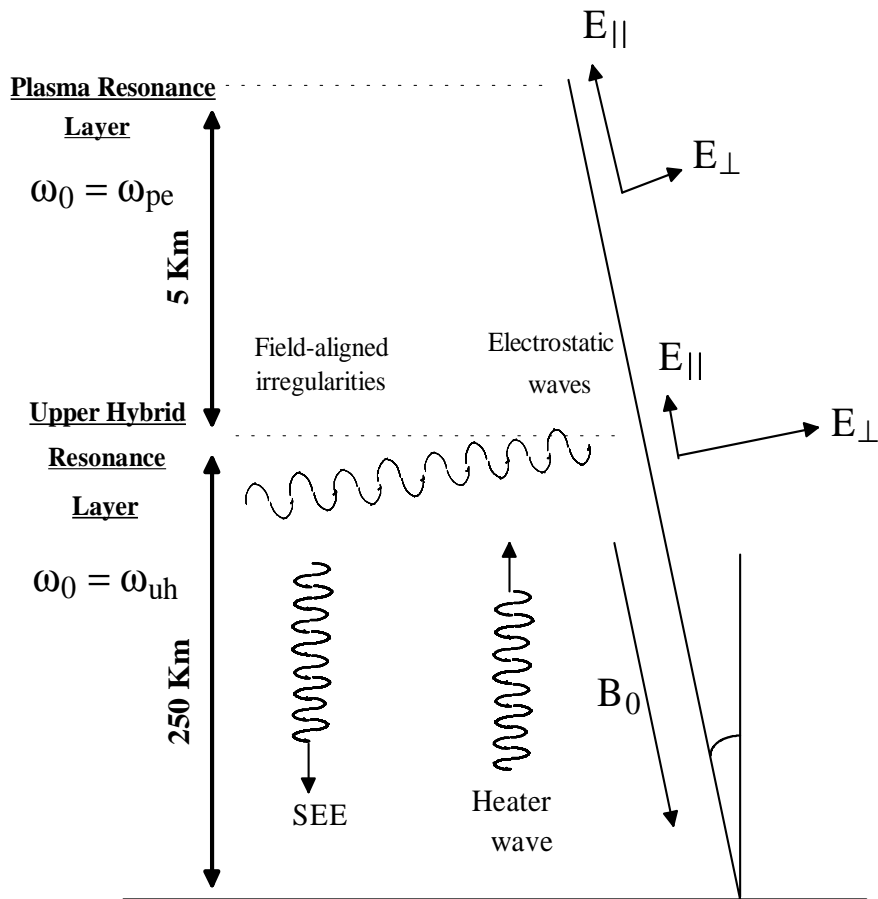
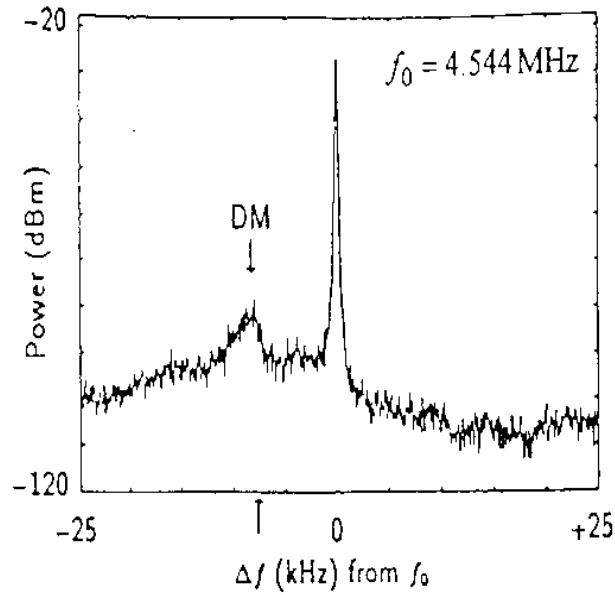


Figure 2.6: The different altitude regions in the generation of SEE.

Downshifted Maximum (DM) [Thide` et al., 1982]



Downshifted Maximum (DM) [Leyser et al., 1990]

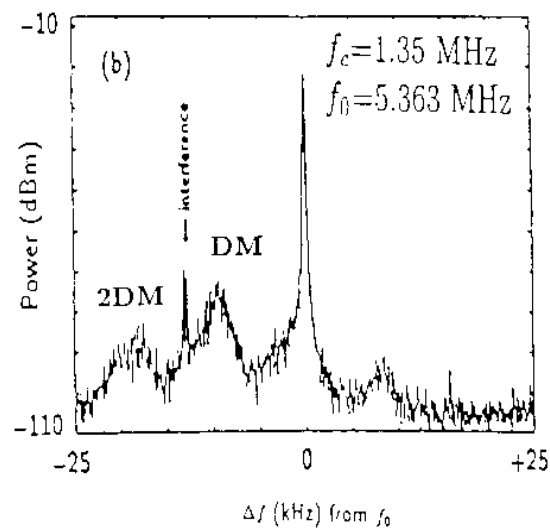


Figure 2.7: Two results from experimental data showing the DM and the cascading of the DM.

Downshifted Peak (DP) [Leyser et al., 1990]

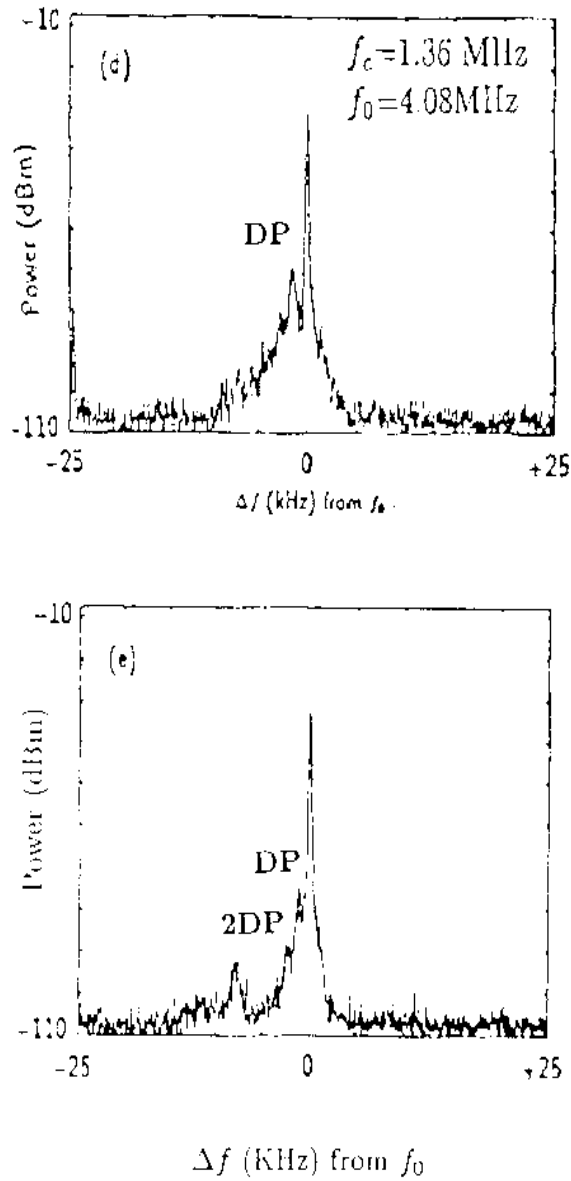


Figure 2.8: Two results from experimental data showing the DP and the cascading of the DP.

Broad Upshifted Maximum (BUM) [Stubbe et al. 1984]

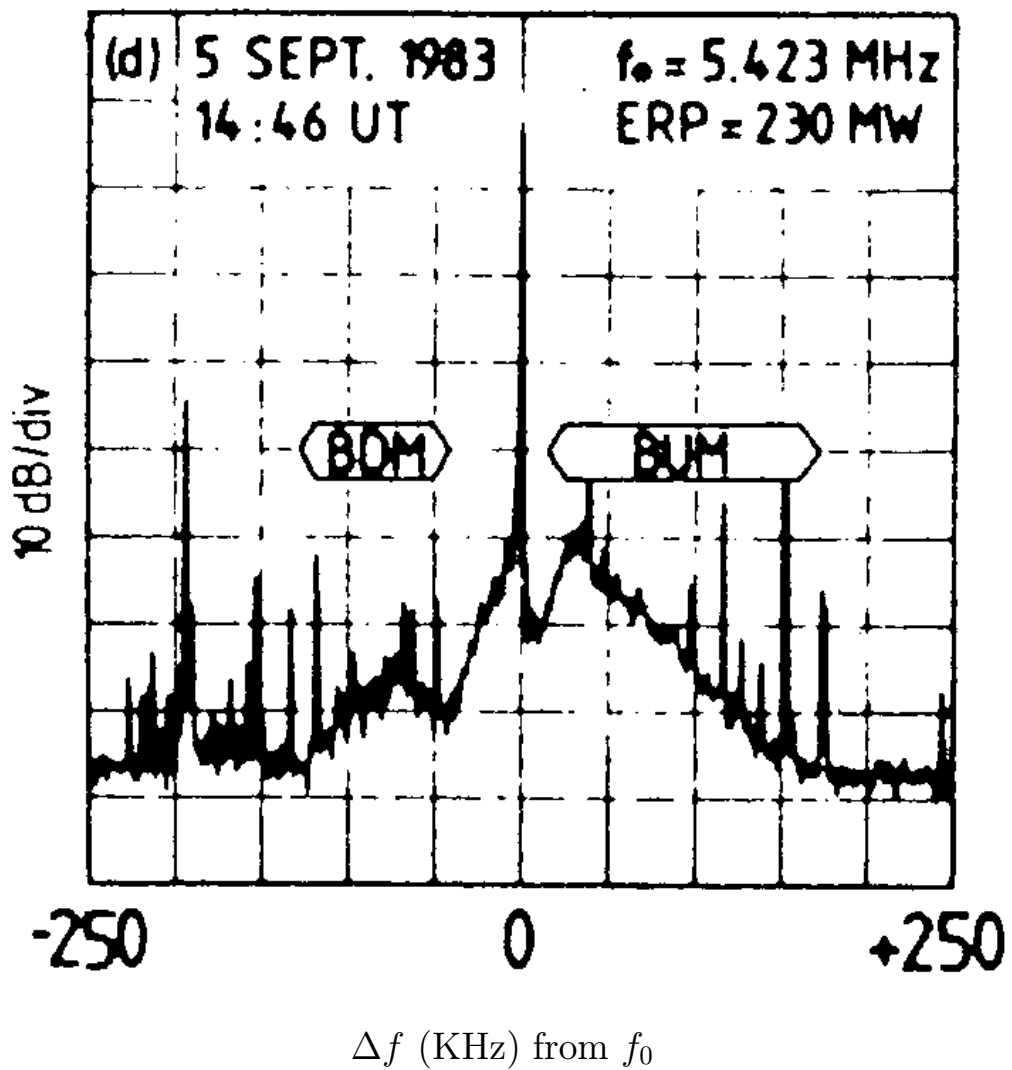


Figure 2.9: Experimental data result showing the BUM and BDM features.

Continuum [Leyser et al., 1990]

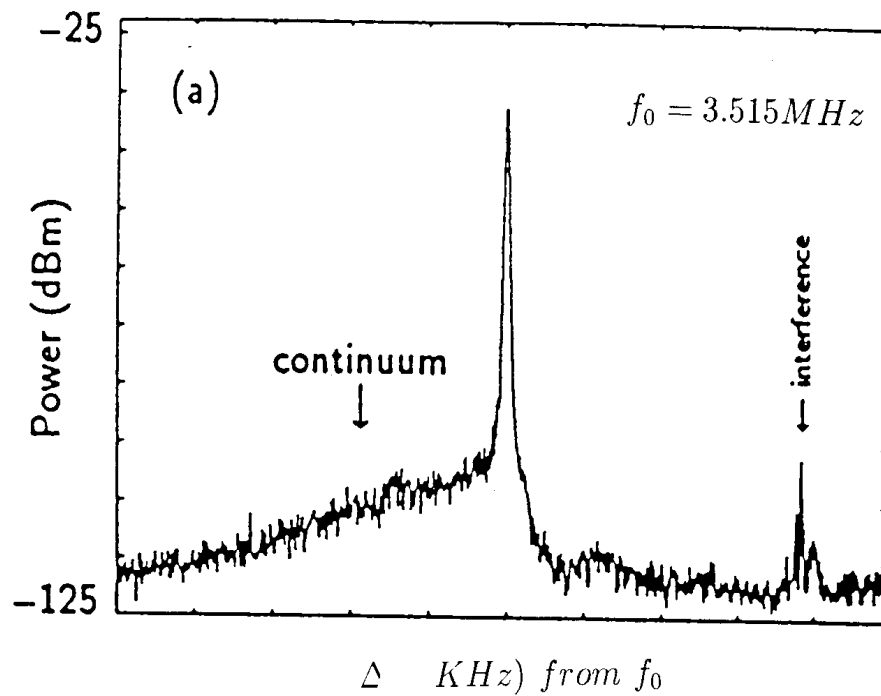


Figure 2.10: A result from experimental data showing the continuum structure.

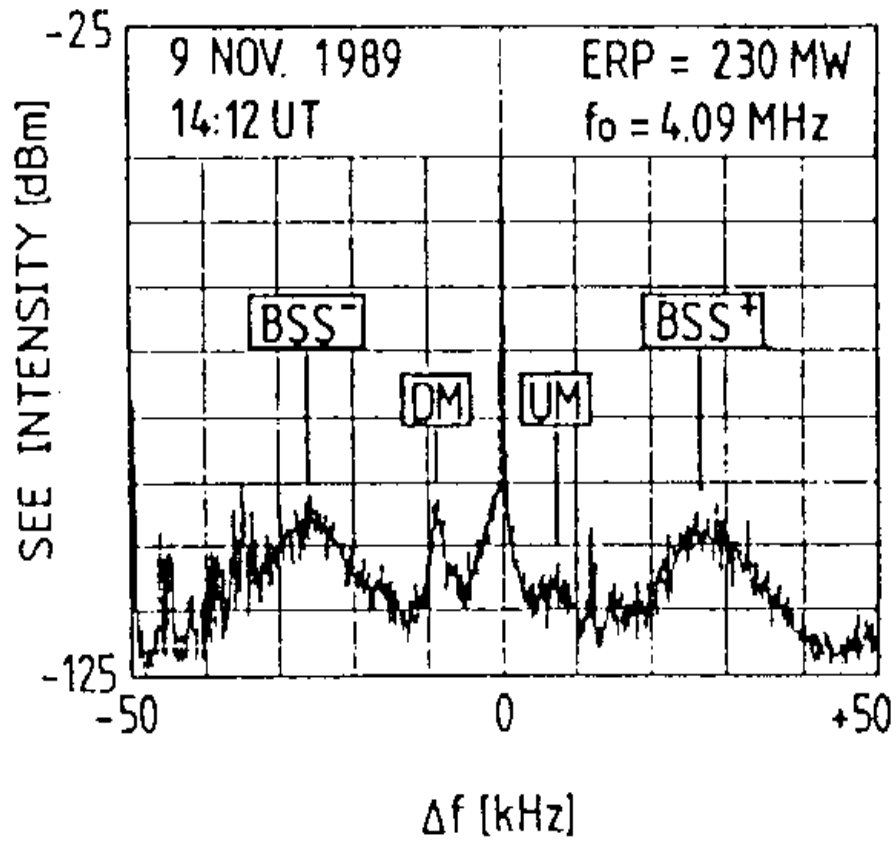
Broad Symmetric Structure (BSS) [Stubbe et al. 1990]

Figure 2.11: A result from experimental data showing the BSS.

Chapter 3

Three-Wave Decay Instability

3.1 Theory

Porkolab [1972] has discussed the coupling between low frequency and high frequency electrostatic waves by parametric instabilities. The model may be used for a qualitative description of down-shifted sidebands such as the DM and DP. The parametric coupling process for the decay of a pump wave (ω_0, k_0) into a sideband (ω_1, k_1) along with a low frequency decay mode (ω_s, k_s) has the frequency and wave vector matching conditions $\omega_0 = \omega_1 + \omega_s$, $k_0 = k_1 + k_s$. The dispersion relation for this 3-wave interaction is given by

$$\epsilon(\omega_s) + \frac{\beta_e^2}{4} \chi_i(\omega_s) \left\{ \frac{\epsilon_e(\omega_s)}{\epsilon_e(-\omega_1^*)} - 2 \right\} = 0 \quad (3.1)$$

where, $\beta_e = 2kv_{osc}/(\omega_0 + \Omega_e)$, $v_{osc} = qE_0/m_e\omega_0$ is the electron oscillating velocity, k is the wave number, m_e the electron mass, E_0 the electric field strength, and q is the electron charge. Also,

$$\epsilon(\omega) = 1 + \chi_e(\omega) + \chi_i(\omega) \quad (3.2)$$

$$\epsilon_e(\omega) = 1 + \chi_e(\omega) \quad (3.3)$$

and the susceptibility of the j^{th} species is given by

$$\chi_j(\omega, k) = \frac{1}{k^2 \lambda_{Dj}^2} \left\{ 1 + \zeta_{j0} \sum_{n=-\infty}^{\infty} \Gamma_n(b_j) Z(\zeta_{jn}) \right\} \quad (3.4)$$

where $b_j = k_{\perp}^2 \rho_j^2 / 2$, $\zeta_{jn} = (\omega - n\Omega_j) / k_{\parallel} v_{tj}$, $\Gamma_n(b_j) = I_n(b_j) \exp(-b_j)$, Z is the Fried Conte function, I_n is the modified Bessel function of the first kind of order n , λ_{Dj} is the Debye length, k_{\parallel} (k_{\perp}) is the component of k parallel (perpendicular) to B , ρ_j is the gyroradius, and v_{tj} is the thermal velocity. *Zhou et al.* [1994] have developed a more complete treatment of the three wave decay to interpret SEE. Future work might make comparisons with this more detailed theory. The *Porkolab* [1972] model was found to be more than adequate for guiding the simulation work and in general was in good agreement with simulation results.

Since we consider processes nearly perpendicular to the magnetic field, the relevant low frequency decay modes in this case are the lower hybrid and the ion acoustic modes. The linear dispersion relation for the low frequency decay mode is given as follows [*Ichimaru, 1973*]

$$1 - \frac{\omega_{pe}^2}{\omega_s^2 - \Omega_e^2} + \frac{k_{de}^2}{k_s^2} \mathbf{W}\left(\frac{\omega_s}{k_{sz} v_e}\right) - \frac{\omega_{pi}^2}{\omega_s^2 - \Omega_i^2} + \frac{k_{di}^2}{k_s^2} \mathbf{W}\left(\frac{\omega_s}{k_{sz} v_i}\right) = 0 \quad (3.5)$$

where $\mathbf{W}(\sqrt{2}\zeta) = 1 + \zeta \mathbf{Z}(\zeta)$, and \mathbf{Z} is the Fried and Conte function. In the frequency regime $k_{sz} v_i \ll k_{sz} v_e \ll \omega_s$ and neglecting damping effects, the dispersion relation reduces to

$$1 - \frac{\omega_{pe}^2}{\Omega_e^2} - \frac{\omega_{pi}^2}{\omega_s^2 - \Omega_i^2} + \frac{k_{sz}^2}{k_s^2} \frac{\omega_{pe}^2 + \omega_{pi}^2}{\omega_s^2} = 0 \quad (3.6)$$

which leads to the dispersion relation for the lower hybrid wave given by

$$\omega_s^2 = \frac{\omega_{pi}^2}{(1 + \omega_{pe}^2 / \Omega_e^2)} [1 + m_i / m_e (k_{sz} / k_s)^2] \quad (3.7)$$

We then obtain the dispersion relation for the lower hybrid wave in the regime $\theta < \sqrt{m_e / m_i}$

$$\omega_s^2 \simeq \omega_{lh}^2 \left[1 + \frac{m_i}{m_e} \left(\frac{k_{\parallel}}{k_s} \right)^2 \right] \quad (3.8)$$

where $k_{sz}/k_s = \sin(\theta)$ and $\omega_{lh} \equiv \sqrt{\Omega_{ce}\Omega_{ci}}$ is the lower hybrid resonance frequency.

In the frequency regime $k_{sz}v_i \ll \omega_s \ll k_{sz}v_e$ and neglecting the damping effects and using $\omega_s \ll \Omega_e$, the dispersion relation in equation (1) reduces to:

$$1 - \frac{k_{de}^2}{k_s^2} - \frac{k_{sz}^2}{k_s^2} \frac{\omega_{pi}^2}{\omega_s^2} + \frac{\omega_{pe}^2}{\Omega_e^2} - \frac{\omega_{pi}^2}{\omega_s^2 - \Omega_i^2} = 0 \quad (3.9)$$

We then obtain the dispersion relation for the electrostatic ion cyclotron wave in the regime $\theta > \sqrt{m_e/m_i}$ as follows

$$\omega_s^2 = \Omega_i^2 + \omega_{pi}^2/(1 + k_{de}^2/k_s^2) \simeq \Omega_i^2 + k_s^2 c_s^2 \quad (3.10)$$

where $c_s = \sqrt{(KT_e + KT_i)/m_i}$ is the sound speed and K is Boltzman constant.

Figure (3.1) shows the dispersion relation for the lower hybrid wave obtained numerically at different angles θ , (a) $\theta = 0.7\sqrt{m_e/m_i}$, (b) $\theta = 1.0\sqrt{m_e/m_i}$, (c) $\theta = 1.4\sqrt{m_e/m_i}$, since it is an angular dependent wave. The dispersion relation for the ion cyclotron wave is also shown in Figure (3.1) (thick dashed line) which was also obtained by solving equation (3.1) numerically for the case $\theta = 4\sqrt{m_e/m_i}$. Note that the ion cyclotron waves were found to be nearly angular independent. It was also found that the dispersion relations for both the lower hybrid and ion cyclotron waves obtained numerically were in a very close agreement with the analytical approximate expressions given in equations (3.9) and (3.10) respectively.

The dispersion relation given in (3.1) is solved using the method of *Rönmark* [1983] [Appendix A,B] to obtain the growth rate γ . The angle corresponding to the deviation from perpendicular propagation θ is varied and the growth rate is computed when $\omega_0 = 3\Omega_{ce} + 3\omega_{lh}$ and $\omega_{uh} = 3\Omega_{ce}$. The mass ratio in this case is $m_e/m_i = 400$ (corresponding to the simulations to be discussed later), the oscillating velocity $v_{osc}/v_{te} = 0.3$, and the electron to ion temperature ratio (T_e/T_i) is taken to be 0.2, 1.0 and 10.0. Again, we consider the case $\omega_0 > \omega_{uh}$. The dispersion relation for the upper hybrid and the electron Bernstein mode and the location of ω_0 are shown in Figure (3.2). The results shown in Figure (3.3) show the growth rate for both the lower hybrid mode and the ion cyclotron mode versus angle for different T_e/T_i . The two sets of growth rate curves shown in Figure (3.3) (a-c) correspond to the lower hybrid decay instability LHDI (dashed plot) and the ion cyclotron decay instability ICDI (solid plot). The growth rate for the LHDI peaks at an angle which roughly equals $\sqrt{m_e/m_i}$. The growth rate for the ICDI maximizes at an angle which is larger

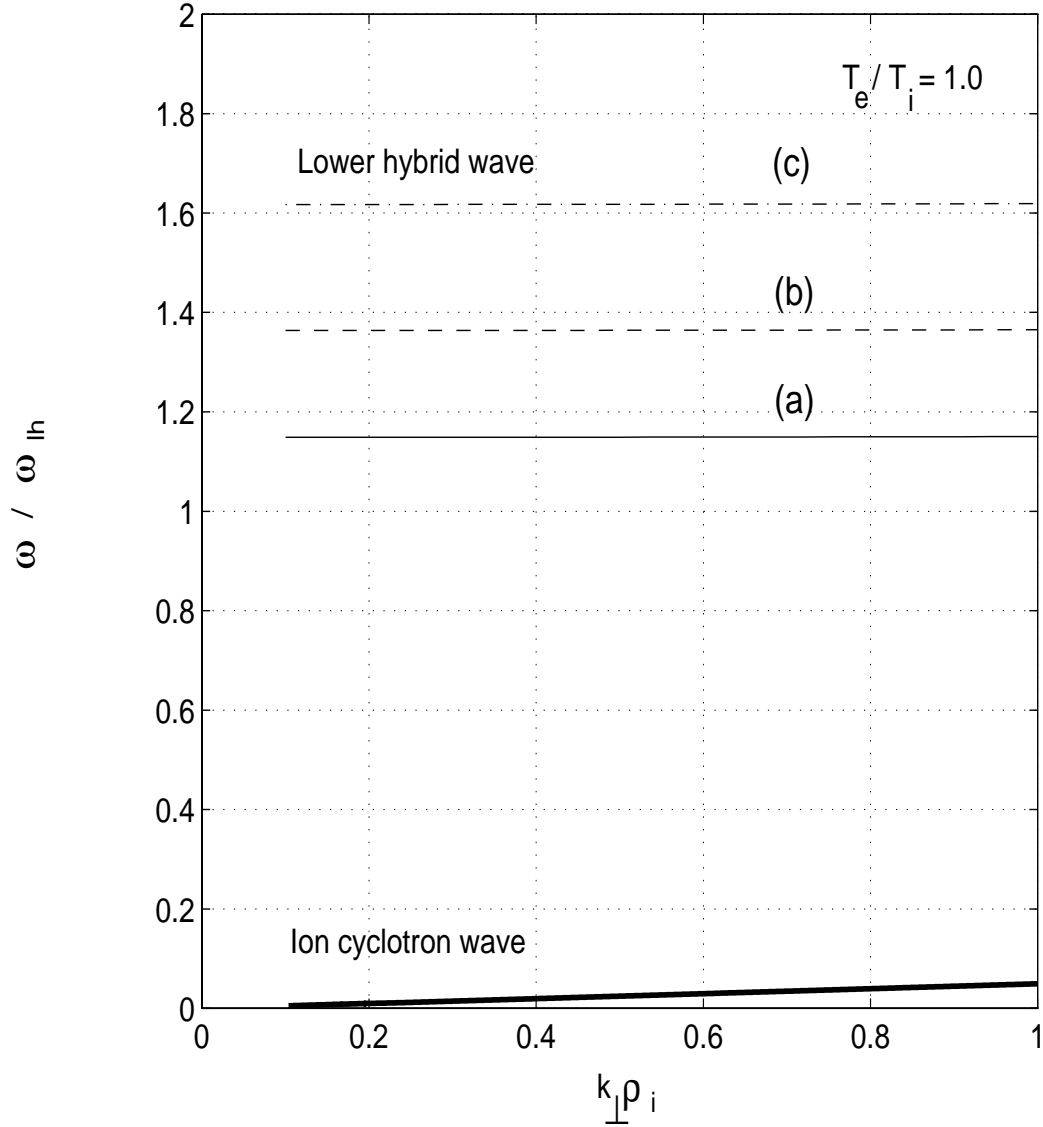


Figure 3.1: A plot for the dispersion relation for both the lower hybrid wave for the cases (a) $\theta = 0.7\sqrt{m_e/m_i}$ (b) $\theta = 1.0\sqrt{m_e/m_i}$ and (c) $\theta = 1.4\sqrt{m_e/m_i}$ and for the ion cyclotron wave for the case $\theta = 4.0\sqrt{m_e/m_i}$.

than $\sqrt{m_e/m_i}$. Also note the sharp cutoff in the growth rate for both cases as θ decreases.

The result obtained by varying T_e/T_i shows that the growth rate for the ICDI increases substantially as the ratio T_e/T_i is increased and the growth rate for the lower hybrid wave is essentially temperature independent. For small ratios of T_e/T_i the ion cyclotron modes are ion Landau damped and the growth rate is reduced. Note also that the growth rate for the ion cyclotron waves becomes larger than that of the lower hybrid waves as T_e/T_i increases. Figure(3.4) is a plot for γ versus T_e/T_i for both the LHDI and ICDI. It shows that the growth rate of the ICDI increases as the ratio T_e/T_i is increased. It also shows that the LHDI is essentially temperature independent for $T_e/T_i > 1$.

The angle at which the growth rate maximizes in Figure (3.3) for both the ICDI and the LHDI was used to plot the growth rate versus frequency. The result is shown in Figure (3.5). The result shows that for the ICDI, the frequency of maximum growth and the bandwidth decrease as T_e/T_i increases. Similar effects are observed in the LHDI but much less pronounced. Also, the angle of maximum growth for both the ICDI and the LHDI is used to plot the growth rate versus the wavelength k . The result is shown in Figure (3.6). The result shows that the ICDI appears at a shorter wavelength regime than the LHDI.

3.2 Simulation model

A periodic one space dimension and three velocity dimension (1D3V) electrostatic Particle-In-Cell (PIC) simulation model using standard techniques [*Birdsall and Langdon*, 1991] is used in this study. The model geometry is shown in Figure (3.7) [Appendix C]. An external oscillating uniform electric field E with amplitude given by

$$E = E_0 \cos(\omega_0 t) \quad (3.11)$$

is used to present the long wavelength electromagnetic pump field and is applied uniformly across the simulation box. The system length is $1024\lambda_D$, where λ_D is the initial electron Debye length, with a uniform density of 200 particles per grid cell for each species. The total number of particles in the simulation is 405600. The mass ratio of ions to electrons is $m_i/m_e = 400$ which provides sufficient separation of the ion and electron timescales. The ions and electrons are initialized with a Maxwellian velocity distribution. The field strength $v_{osc}/v_{te} = 0.3$. Note that these artificially

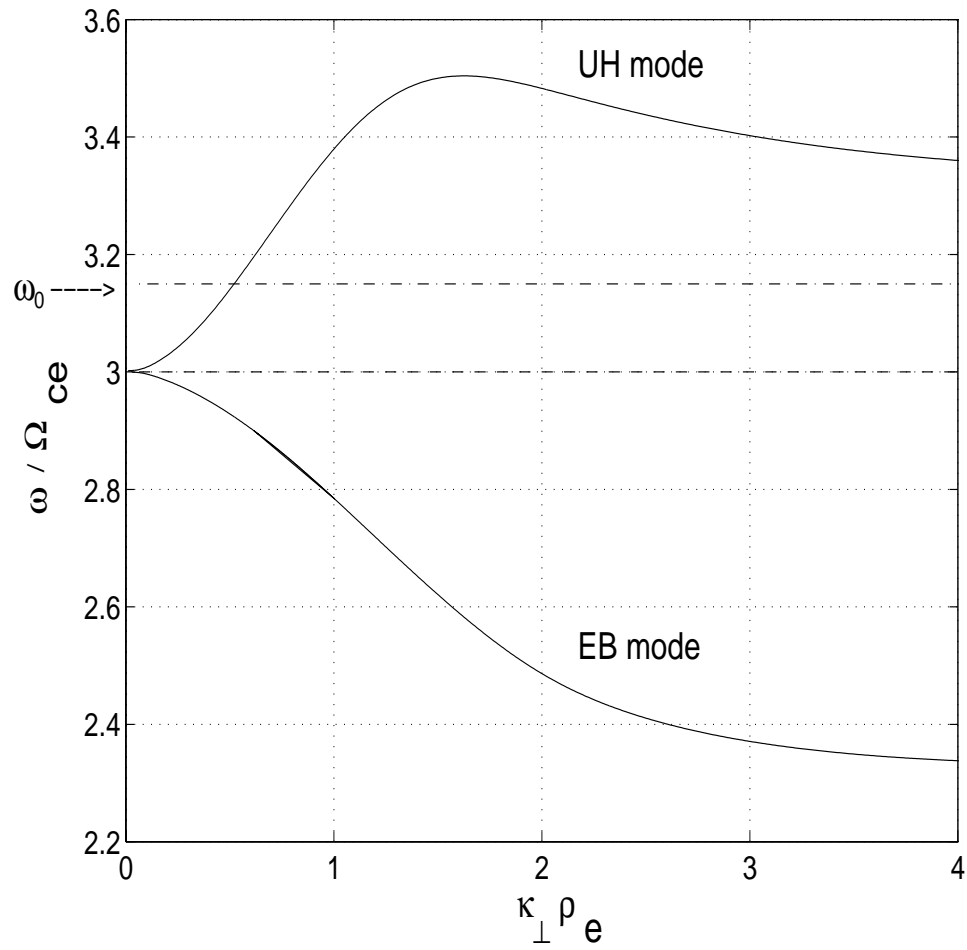


Figure 3.2: The dispersion relation for the upper hybrid and electron Bernstein modes and the location of the pump frequency ω_0 for the growth rate shown in Figure (3.3).

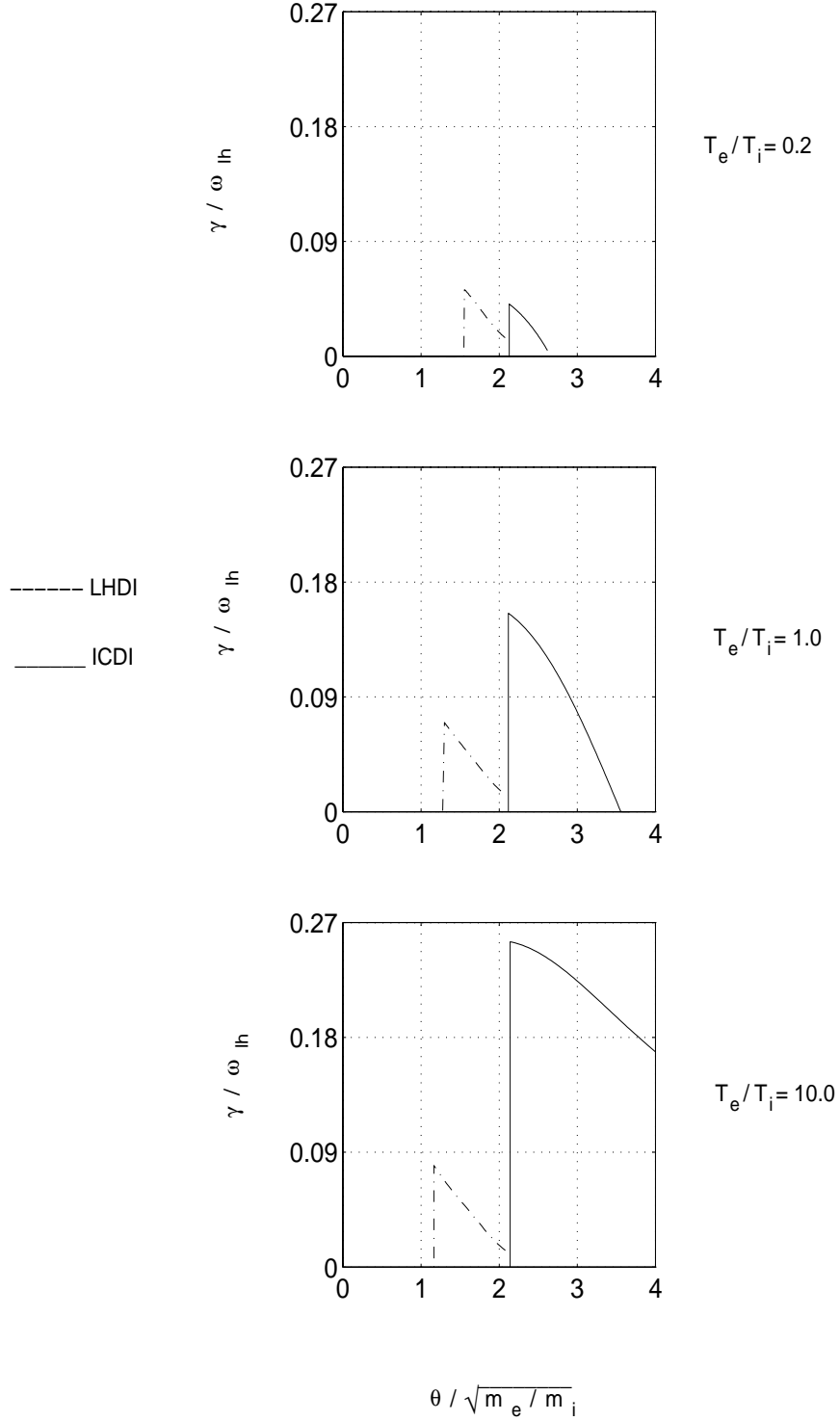


Figure 3.3: A plot of the growth rate γ vs θ in equation (1) for the case $\omega_0 = 3\Omega_{ce} + 3\omega_{lh}$ and for different temperature ratios T_e/T_i for the LHDI and the ICDI.

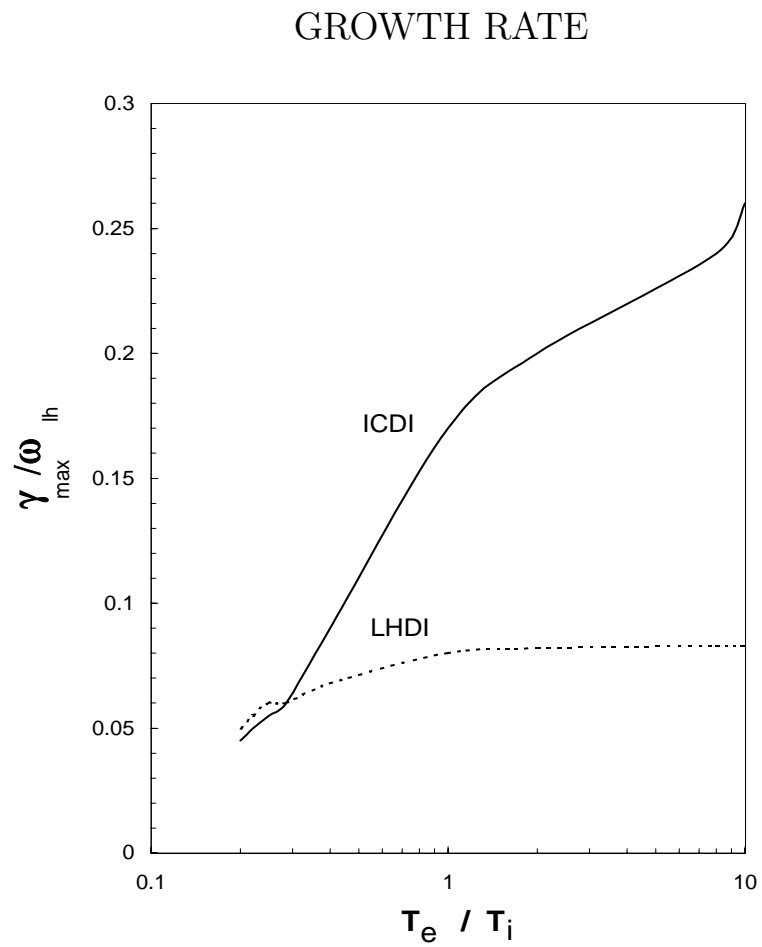


Figure 3.4: A plot of the maximum growth rate γ_{max} vs electron-ion temperature ratio T_e/T_i for the case $\omega_0 = 3\Omega_{ce} + 3\omega_{lh}$ for both ICDI and LHDI.

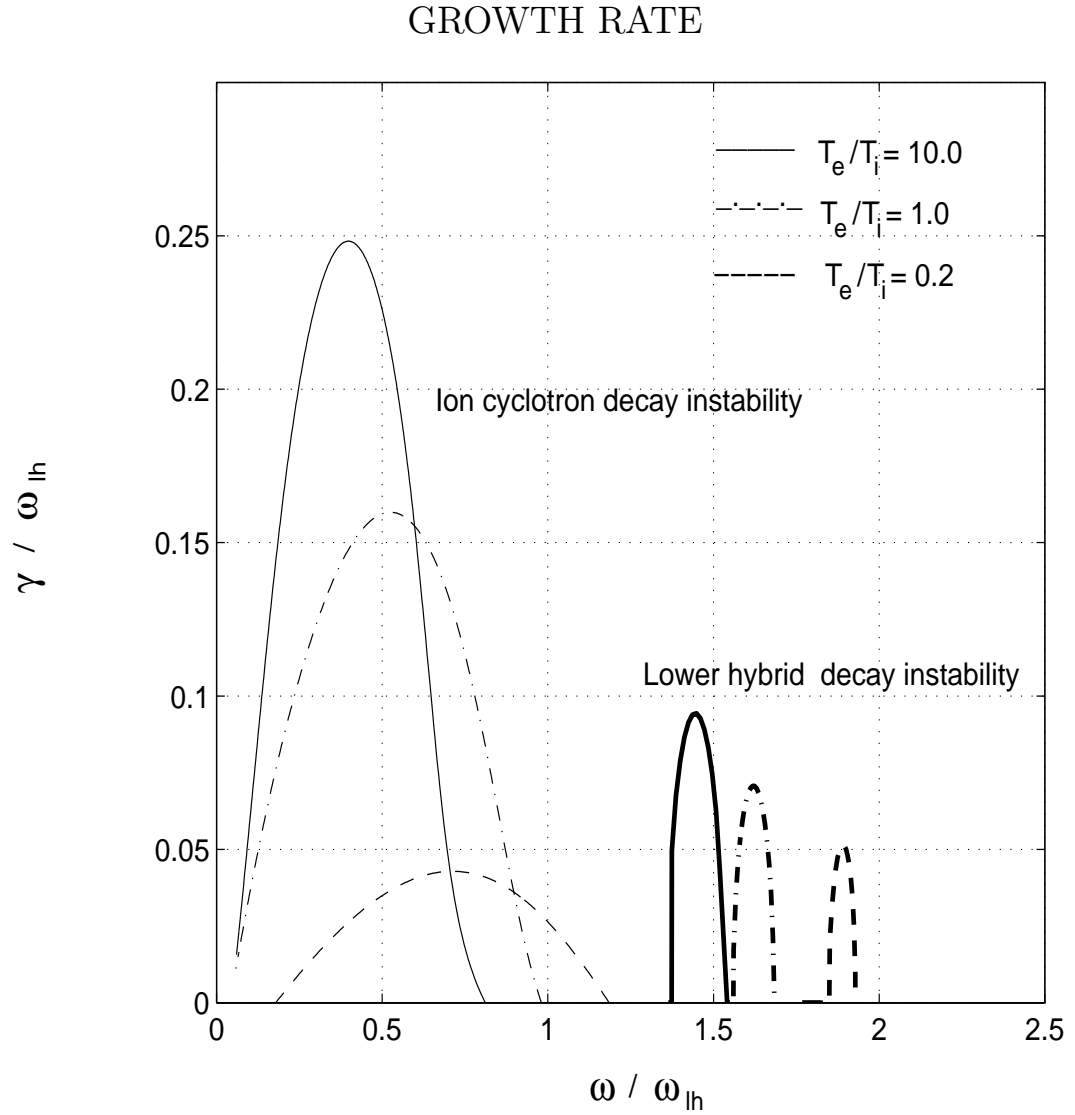


Figure 3.5: A plot of the growth rate γ vs ω in equation (3.1) for the case $\omega_0 = 3\Omega_{ce} + 3\omega_{lh}$ and for different temperature ratios T_e/T_i for both the ion cyclotron and lower hybrid modes.

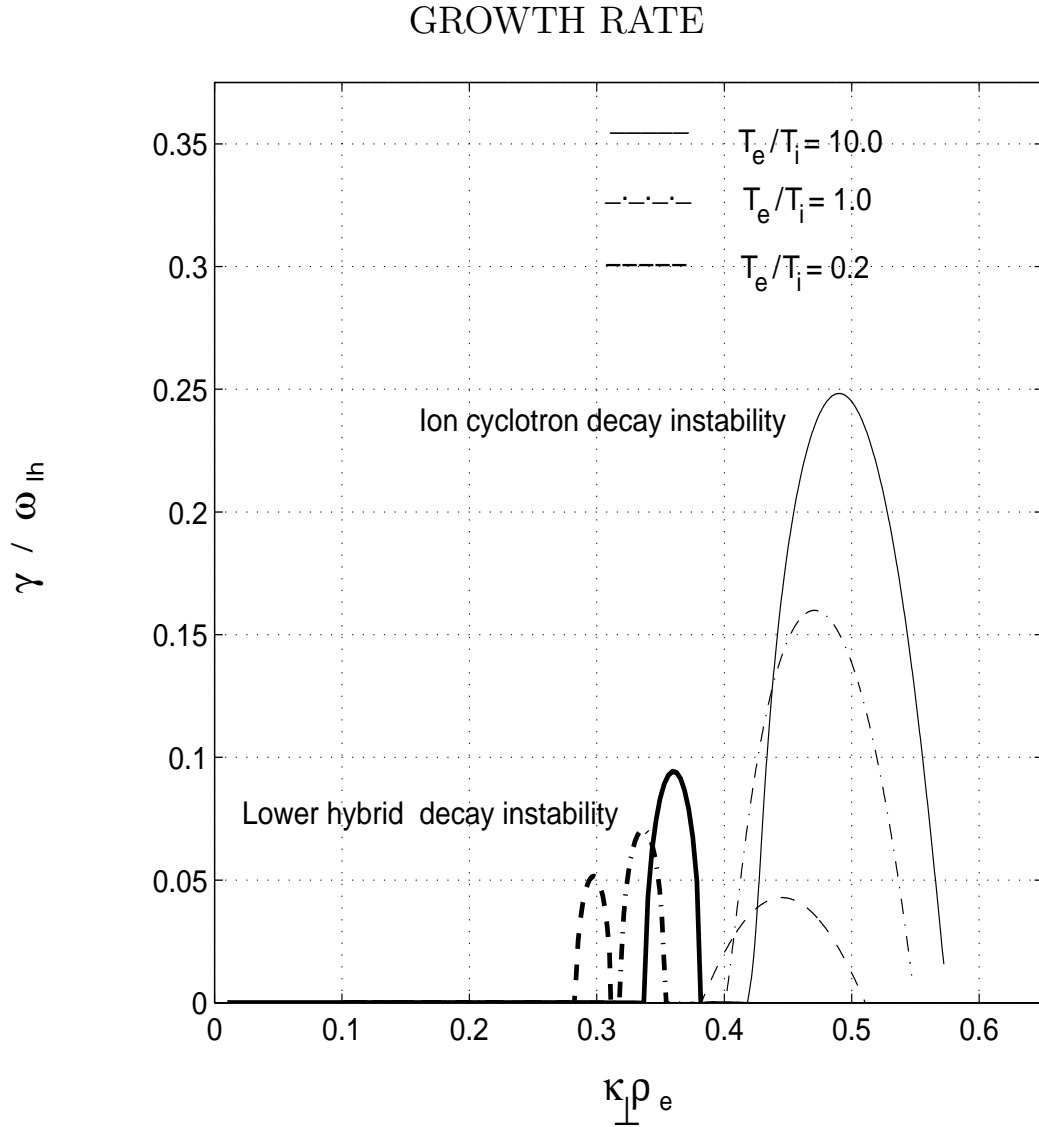


Figure 3.6: A plot of the growth rate γ vs wavelength k in equation (3.1) for the case $\omega_0 = 3\Omega_{ce} + 3\omega_{lh}$ and for different temperature ratios T_e/T_i for both the ion cyclotron and lower hybrid modes.

large values allow the simulation to run in a reasonable amount of CPU time and will not make qualitative physics changes. The simulation runs for up to 600,000 time steps (corresponding to an end time $\omega_{lh}t = 2000$ and a real time of approximately 60 milliseconds) to allow for a steady state to take place and sufficient frequency resolution.

3.3 Simulation results

3.3.1 Simulation results for the LHDI

A large number of simulations have been performed by using the parameters described previously. The results in Figure (3.2) and Figure (3.3) are used to guide our simulation runs. Figure (3.8) shows the total electric field energy history during the simulation of the LHDI. It shows that the field energy reaches steady state by the end of the simulation. It also shows that the simulation runs for at least 5 growth periods of the LHDI. Figure (3.9) shows the history plots of the kinetic energy for both the ions and electrons. Note the increase in the kinetic energy for the electrons due to wave-particle heating process. Figure (3.10) shows simulation electric field power spectra $|E(\omega)|^2$ [Appendix D] for the angle θ chosen to correspond to the angle at which the growth rate in Figure (3.3.b) maximizes for the lower hybrid parametric decay process. The high frequency spectrum shows a sideband emission shifted below the pump wave frequency with a maximum in power at approximately $2\omega_{lh}$ which corresponds to the lower hybrid wave frequency given in equation (3.8) for this propagation angle. A minimum in wave power is observed at ω_{lh} . The low frequency spectrum shows a maximum in power at approximately $2\omega_{lh}$ corresponding to the lower hybrid decay wave. A weaker sideband up-shifted by approximately the lower hybrid frequency is also observed. Note that if the simulation power spectrum was obtained using the current $|J(\omega)|^2$ we would get the same high frequency spectrum we obtained using the electric field $|E(\omega)|^2$. However, we will not be able to obtain the low frequency power spectrum in this case. This was the reason we used the electric field rather than the current to obtain the simulation electric field power spectra.

Figure (3.11) and (3.12) show the electron and ion density during the simulation run for the LHDI discussed earlier at time $\omega_{lh}t = 20$ (early in the simulation run), 180 (late in the simulation run). Well defined density irregularities can be observed to exist in the plasma density. Note that the irregularities become more pronounced as time goes along the simulation run. Figure (3.13) shows the electric field strength during the simulation run. Note that the wavelength in this case is in a very good agreement with the wavelength regime for the LHDI predicted by the theory in Figure (3.6).

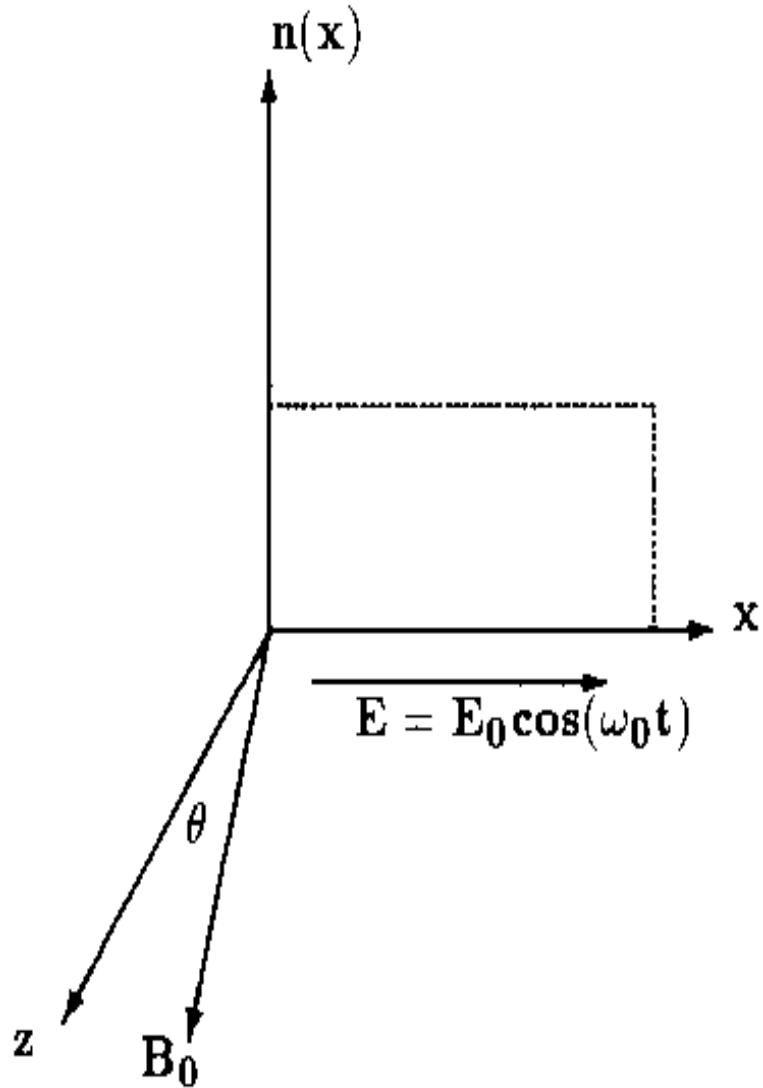


Figure 3.7: A schematic 1D electrostatic PIC model for studying SEE parametric processes around electron gyroharmonic frequencies $n\Omega_{ce}$

ENERGY HISTORY

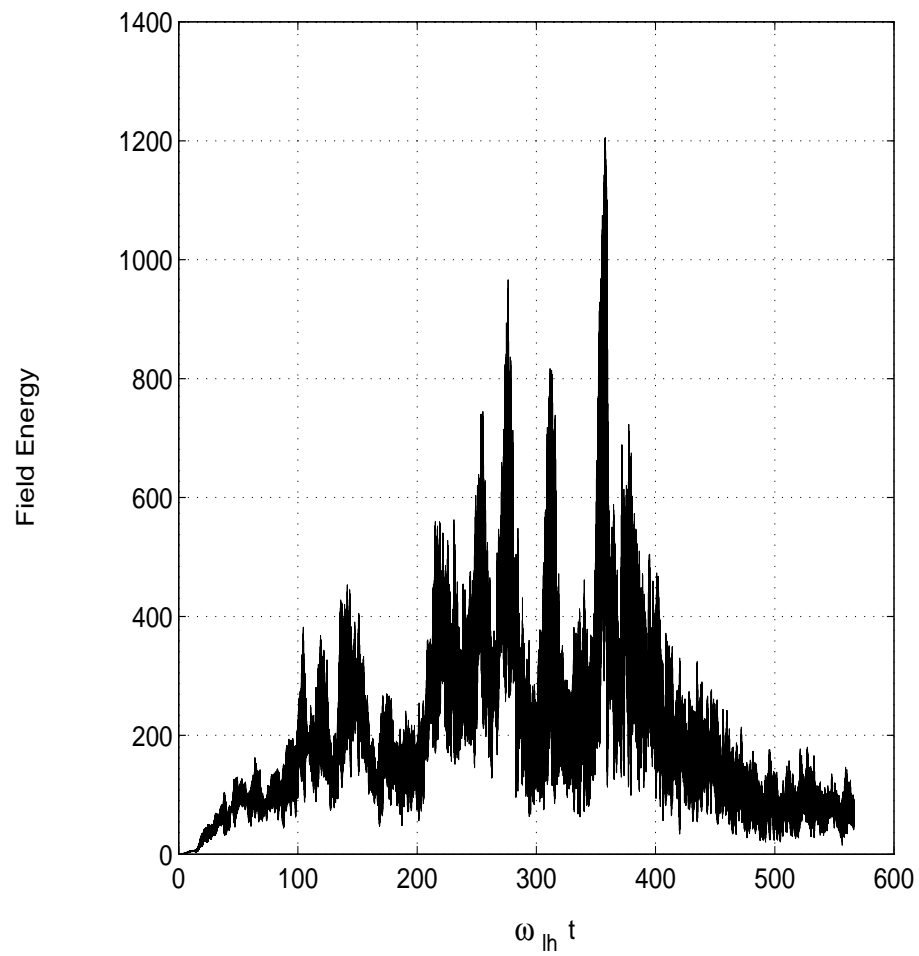


Figure 3.8: Simulation result showing the total field energy in the simulation of the LHDI responsible for the DM.

ENERGY HISTORY

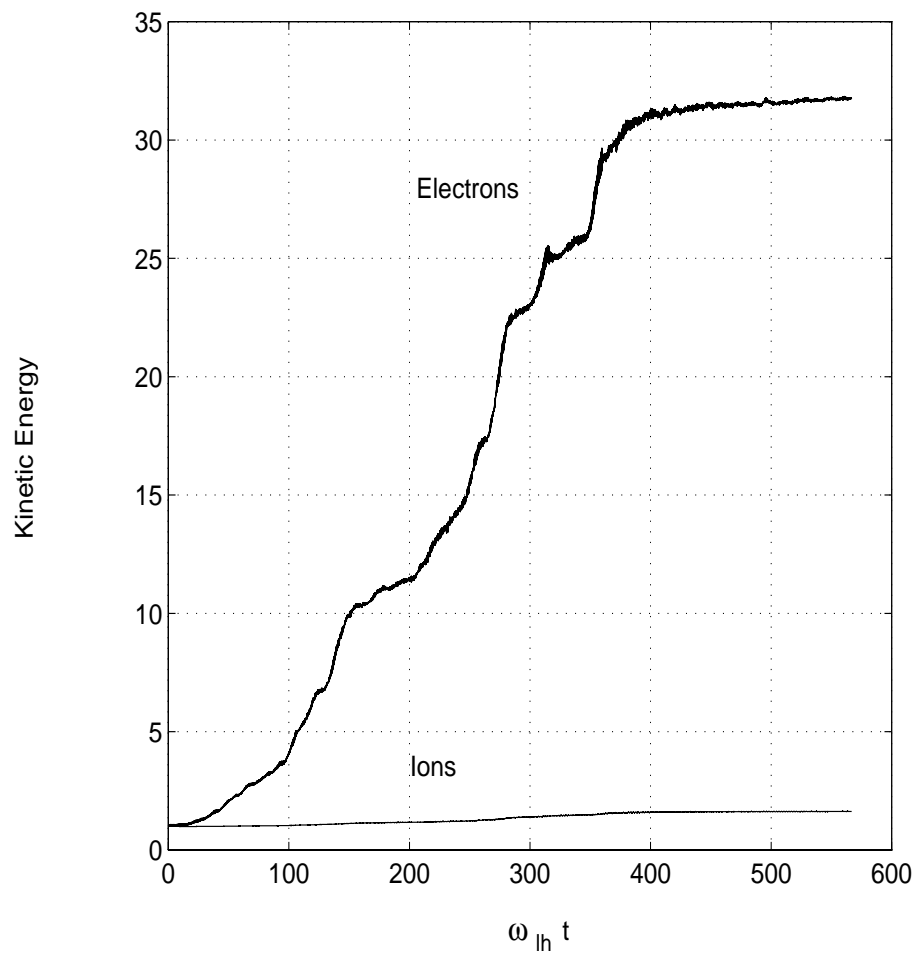


Figure 3.9: Simulation result showing the kinetic energy for both the ions and electrons in the simulation of the LHDI responsible for the DM.

Simulation Electric Field Power Spectrum $|E(\omega)|^2$

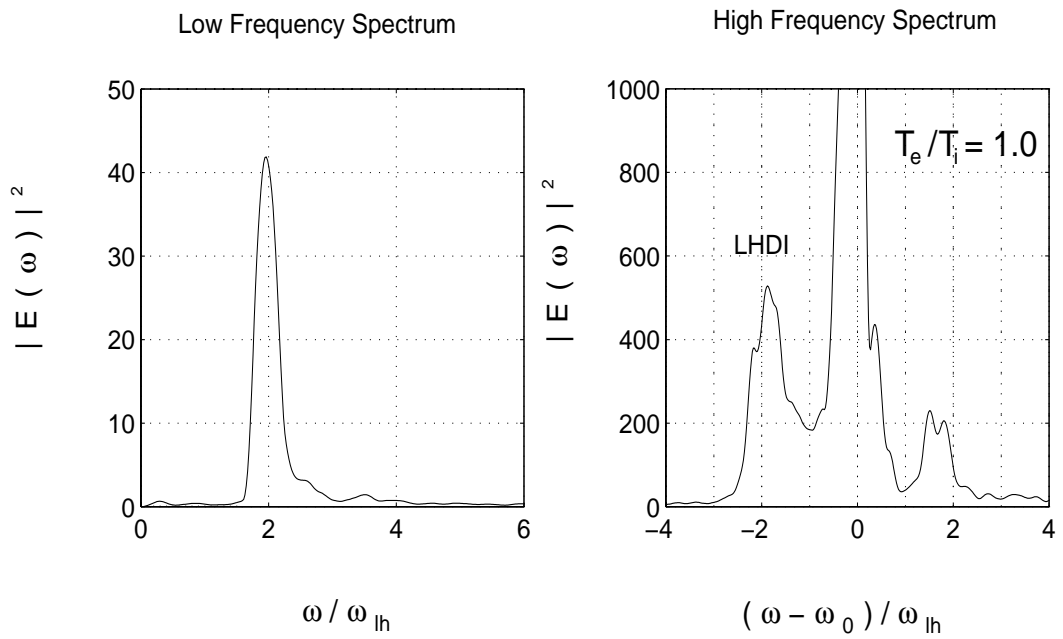


Figure 3.10: Simulation result showing the down-shifted sideband for the case $\omega_0 = 3\Omega_{ce} + 3\omega_{lh}$ and $T_e/T_i = 1.0$ which corresponds to the growth rate calculation in Figure (3.3.b).

ELECTRON DENSITY

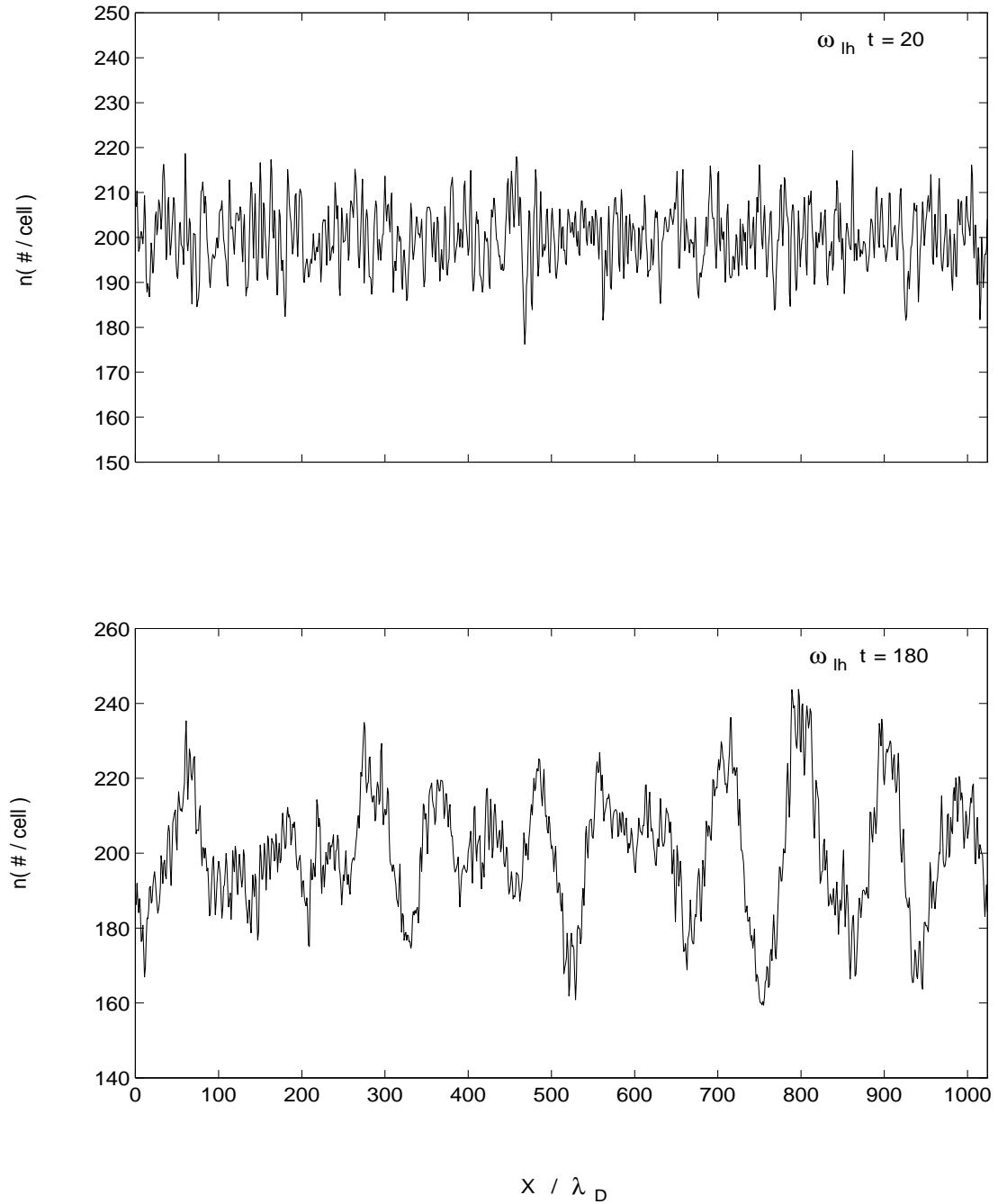


Figure 3.11: Simulation result showing the electron density and density irregularities in the simulation of the LHDI responsible for the DM.

ION DENSITY

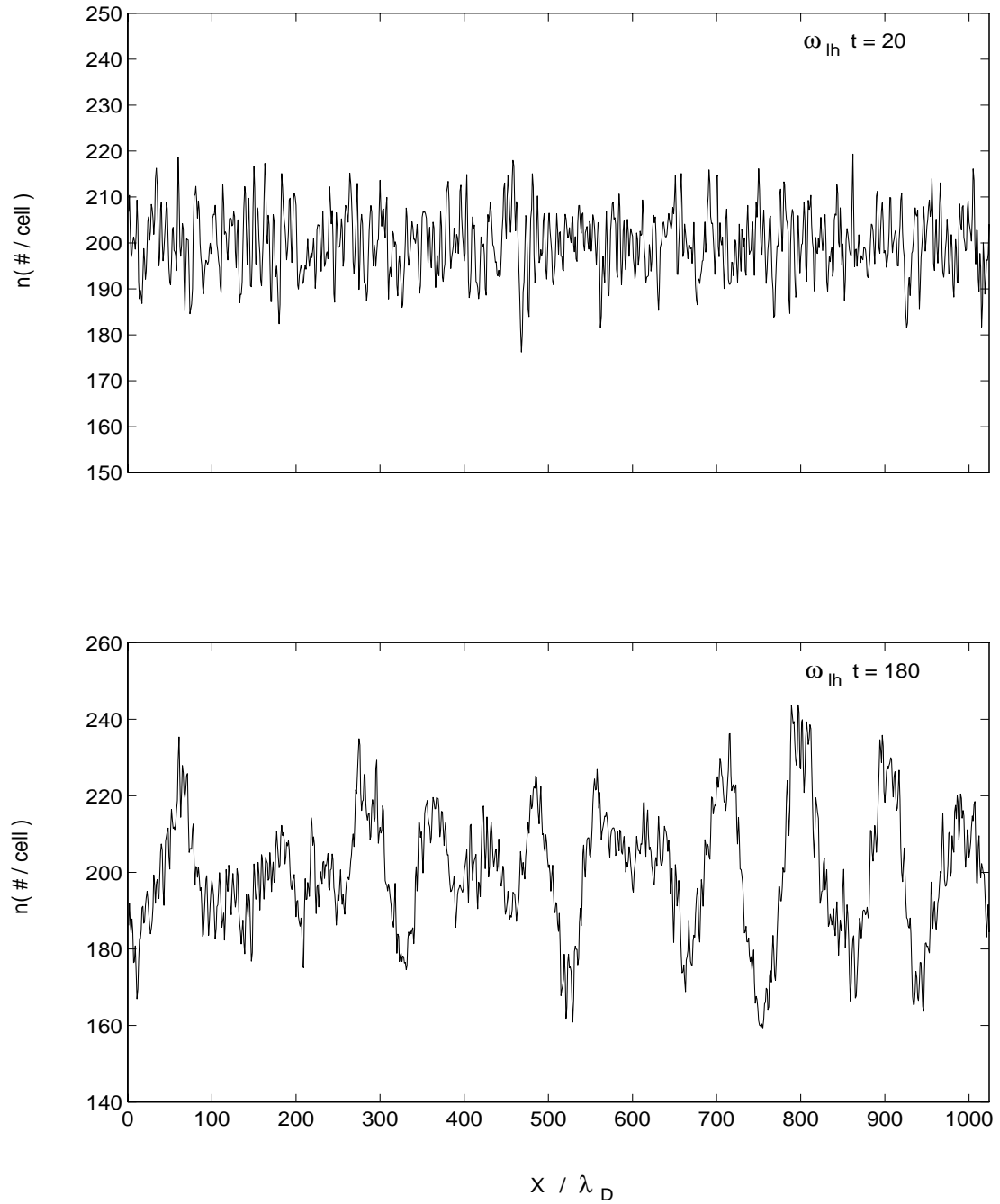


Figure 3.12: Simulation result showing the ion density and density irregularities in the simulation of the LHDl responsible for the DM.

ELECTRIC FIELD

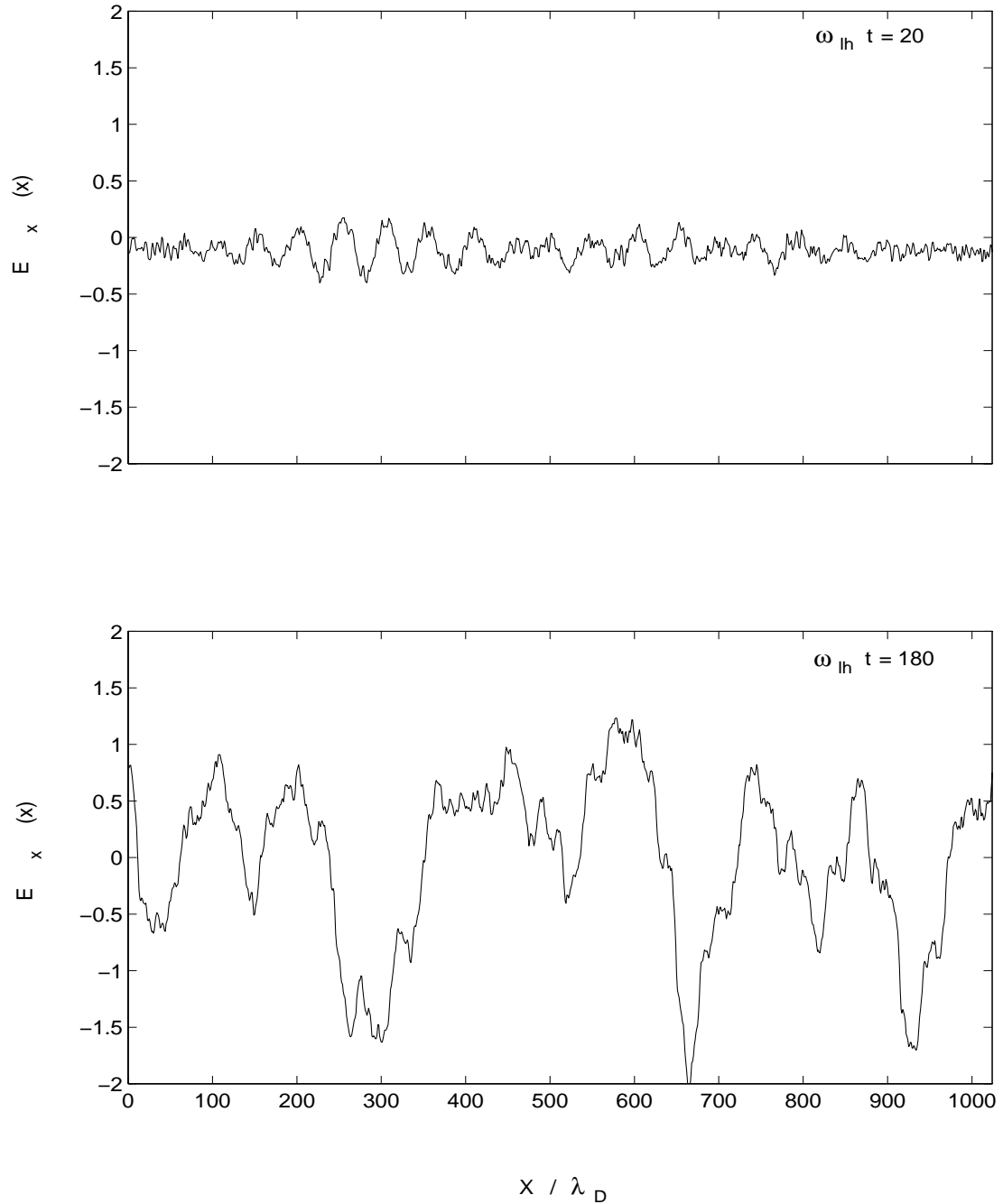


Figure 3.13: Simulation result showing the electric field strength in the simulation of the LHDI responsible for the DM.

3.3.2 Cascading of the LHDI

It was noted during the experimental observations that the DM is absent when the pump frequency ω_0 is very close to an electron cyclotron harmonic $n\Omega_{ce}$ and also when the pump frequency is significantly separated from the cyclotron harmonic. It was also noted that multiple DM structure could also be observed when the pump frequency is reasonably separated from $n\Omega_{ce}$, Figure (2.7). A simulation run was done for the case $\omega_0 = 3\Omega_{ce} + 4\omega_{lh}$ and $\omega_{uh} = 3\Omega_{ce}$ (double resonance condition) to simulate the cascading of this down-shifted sideband. Figure (3.14) shows the growth rate calculation for this case. The angle at which the growth rate maximizes in Figure (3.14) was used to guide the simulation for the cascading of the LHDI. Figure (3.15) shows the electric field power spectrum corresponding to the growth rate calculation in Figure (3.14). The low frequency spectrum shows the corresponding lower hybrid decay wave. The high frequency spectrum shows the multiple down-shifted sidebands corresponding to the cascading of the LHDI.

3.4 Time evolution of the LHDI frequency spectrum

Three simulation electric field power spectra for the LHDI were taken at different time instants of the simulation. $\omega_0 = 3\Omega_{ce} + 3\omega_{lh}$ and $v_{osc}/v_{te} = 0.3$. Figure (3.16) shows the simulation electric field energy history which shows that the simulation reaches steady state at $\omega_{lh}t \simeq 500$. Figure (3.17.a) shows the simulation power spectrum in the linear growth rate regime where $0 < \omega_{lh}t < 250$. Figure (3.17.b,c) show the simulation power spectra after the simulation has reached a steady state or equilibrium. Figure (3.17) shows that the amplitude and shape of the down-shifted sideband in the simulation electric field power spectrum of the LHDI does not change much when the spectrum is taken in the linear growth rate regime or after the simulation has reached a steady state. Figure (3.18) shows three simulation results of the LHDI at the linear growth phase. It shows how the LHDI develops with time.

3.4.1 Simulation results and temperature effect on the ICDI

Figure (3.19) shows 3 simulation runs corresponding to the three growth rate calculations of the ICDI shown in Figure 3.3. The high frequency spectrum shows a sideband shifted below the pump wave frequency by a frequency less than the lower hybrid frequency which corresponds to the ion cyclotron wave frequency given in equation (3.10). The result of varying T_e/T_i shows that the down-shifted sideband

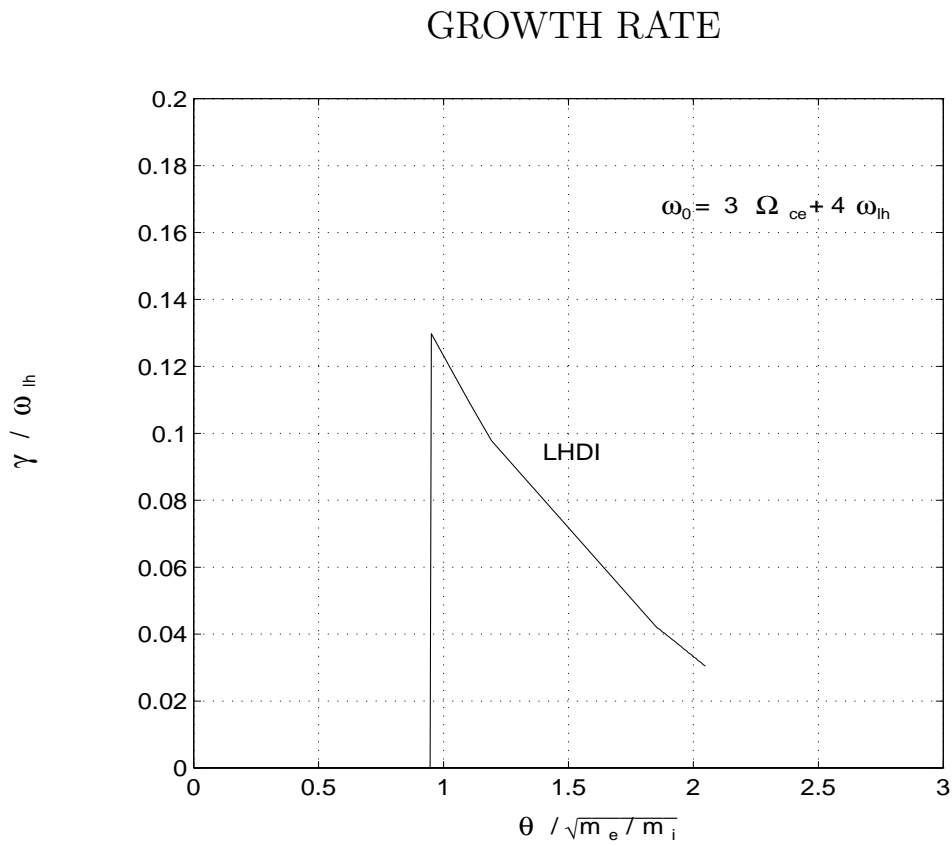


Figure 3.14: The growth rate versus angle for investigating the cascading of the LHDI for the case $\omega_{uh} = 3\Omega_{ce}$.

Simulation Electric Field Power Spectrum $|E(\omega)|^2$

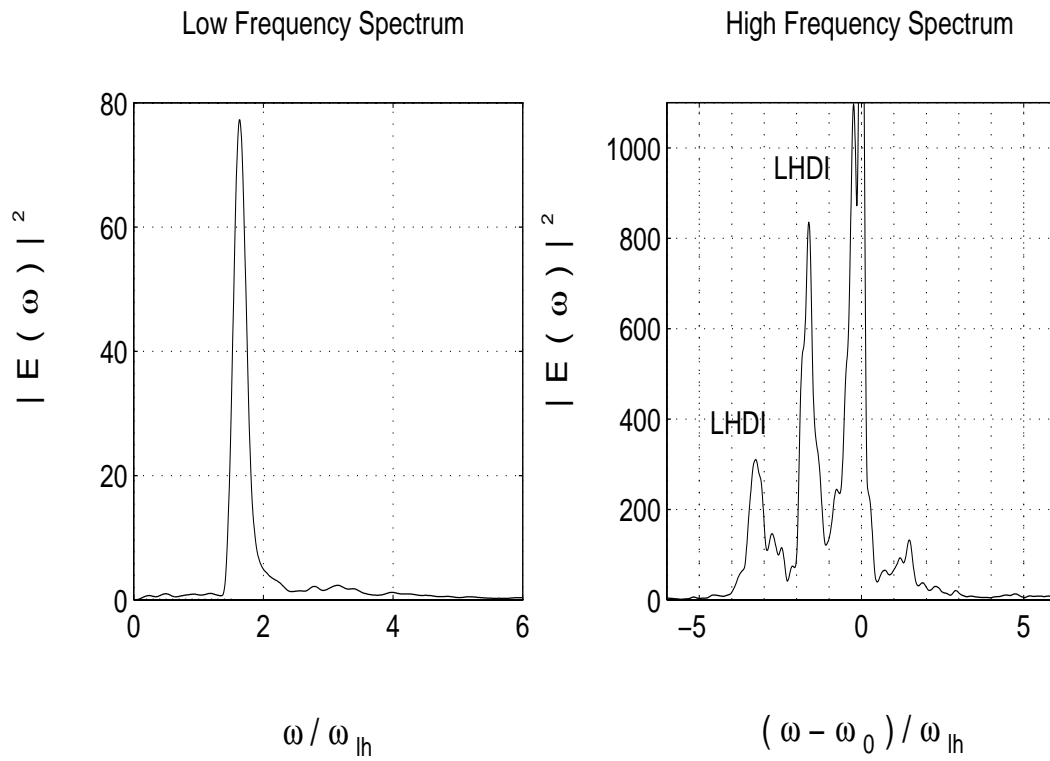


Figure 3.15: Simulation run showing the cascading of the down-shifted sideband for the case $\omega_0 = 3\Omega_{ce} + 4\omega_{lh}$ and $\omega_{uh} = 3\Omega_{ce}$.

ENERGY HISTORY

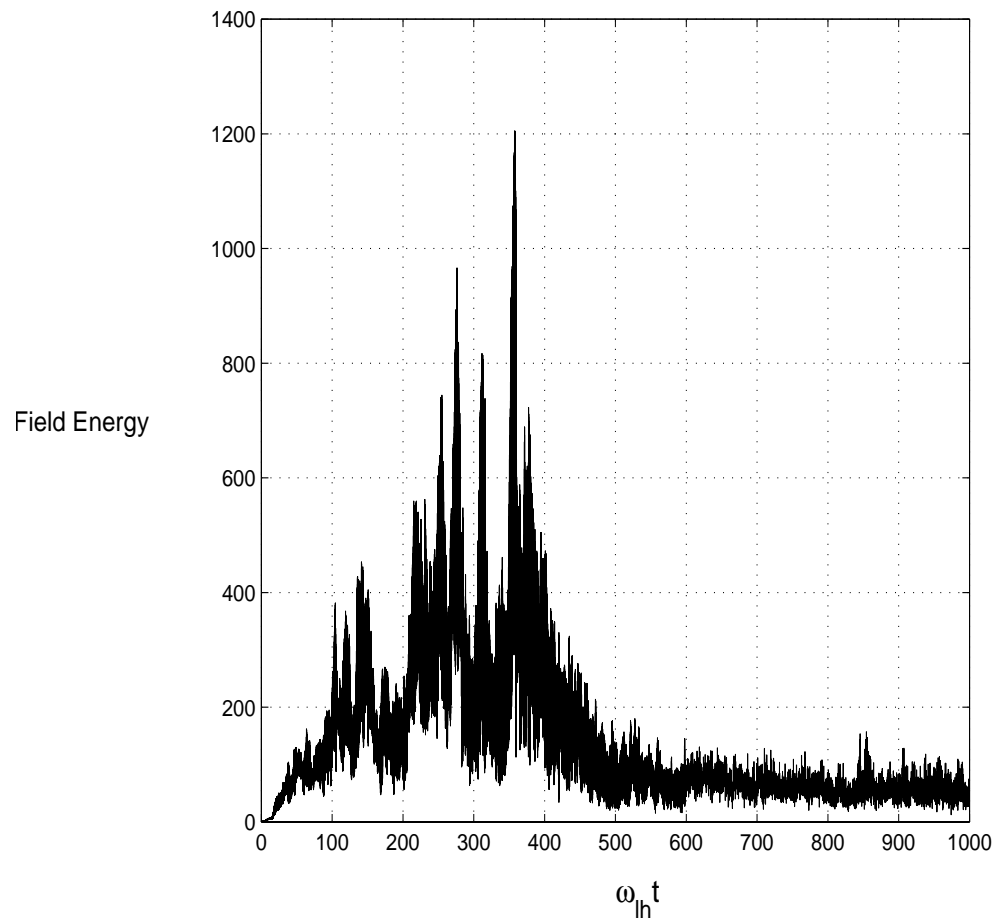


Figure 3.16: The simulation electric field energy history for the simulation results of the LHDI shown in Figure (3.17,18).

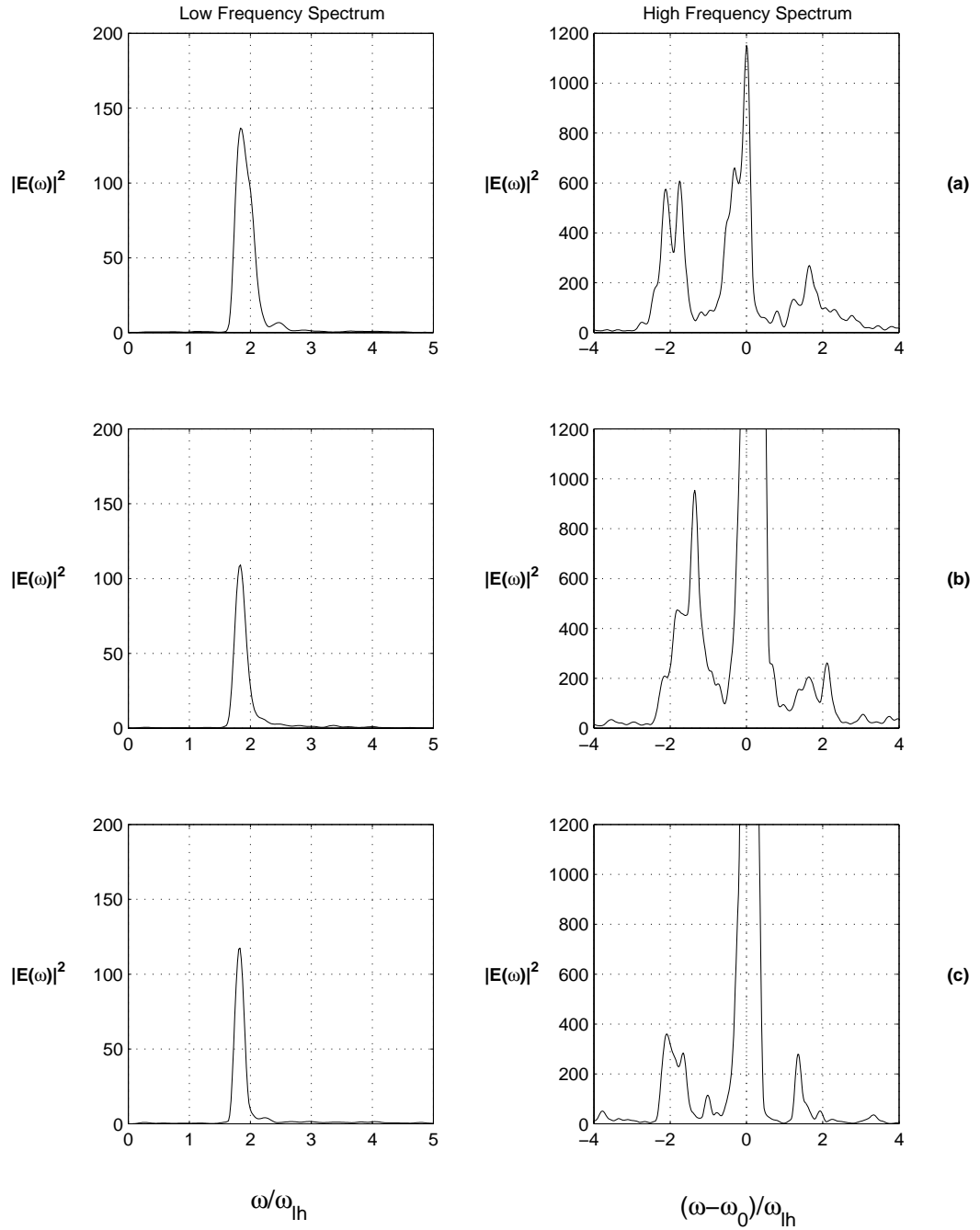


Figure 3.17: Three simulation results showing the simulation electric field power spectrum for the LHD instability at different instants of time (a) $0 < \omega_{1h} t < 300$ (b) $300 \leq \omega_{1h} t < 600$ (c) $600 \leq \omega_{1h} t < 900$.

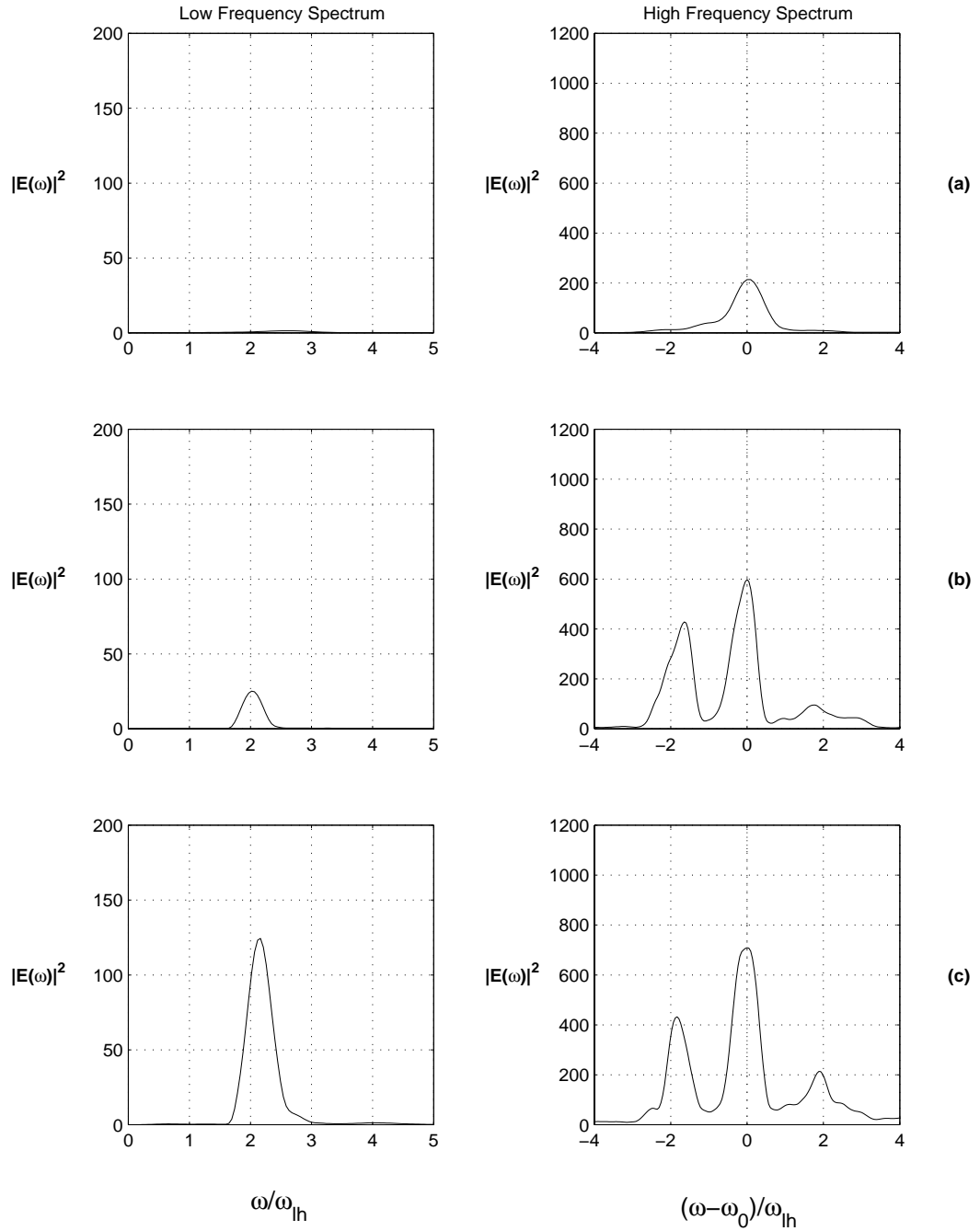


Figure 3.18: Three simulation results showing the simulation electric field power spectrum for the LHDI at different instants of time (a) $0 < \omega_{lh}t < 60$ (b) $60 \leq \omega_{lh}t < 200$ (c) $200 \leq \omega_{lh}t < 330$.

produced by the ICDI is very sensitive to temperature. For $T_e/T_i = 0.2$ the sideband is very weak and relatively broad. It is barely above the noise level. As T_e/T_i is increased the amplitude increases. The frequency of maximum amplitude and bandwidth also decrease. These results are in good qualitative agreement with the linear theory calculation described in Figure (3.3). We also note that the amplitude of the sideband for the LHDI is comparable to that for the ICDI for $T_e/T_i = 1.0$.

By also comparing the spectrum shown in Figure (3.10) and Figure (3.19.b) we notice that the ICDI has a growth rate amplitude larger than that of the LHDI since it has a sharper peak transition. For large values of $T_e/T_i = 10.0$ the ICDI sideband has significantly large amplitude. The LHDI sideband is affected only slightly by variations in T_e/T_i .

Figure (3.20) and (3.21) show the electron and ion density during the simulation run for the ICDI shown in Figure (3.18.b) ($T_e/T_i = 1.0$) at $\omega_{lh}t = 20$ (early in the simulation), 180 (late in the simulation). Density irregularities can be seen to exist in the plasma density. Figure (3.22) shows the electric field strength during the simulation run. Note that the wavelength in this case is in a very good agreement with the wavelength regime for the ICDI predicted by the theory in Figure (3.6). Figure (3.23) shows the history plots of the kinetic energy for both the ions and electrons. Note the increase in the kinetic energy for the electrons due to wave-particle heating process. Note that the particle heating in the case of the ICDI is less pronounced than that of the LHDI. Figure(3.24) shows the field energy history during the simulation run of the ICDI responsible for the DP. It shows that the field energy reaches a steady state by the end of the simulation. It also shows that the simulation runs for up to 9 growth periods of the ICDI. The simulation results for the ICDI were in good agreement with the experimental observations, Figure (2.7).

3.4.2 Cascading of the ICDI

A simulation run was done for the case $\omega_0 = 3\Omega_{ce} + 5\omega_{lh}$ and $\omega_{uh} = 3\Omega_{ce}$ (double resonance condition) to simulate the cascading of the down-shifted sideband. Figure (3.25) shows the growth rate calculation for this case. The angle at which γ maximizes in Figure (3.25) was used to guide our simulation for the cascading of the ICDI. Figure (3.26) shows the electric field power spectrum corresponding to the growth rate calculation in Figure (3.25). The low frequency spectrum shows the corresponding ion cyclotron decay wave. The high frequency spectrum shows the multiple down-shifted sidebands corresponding to the cascading of the ICDI process. The simulation results we obtained were in good agreement with the experimental observations, Figure (2.8).

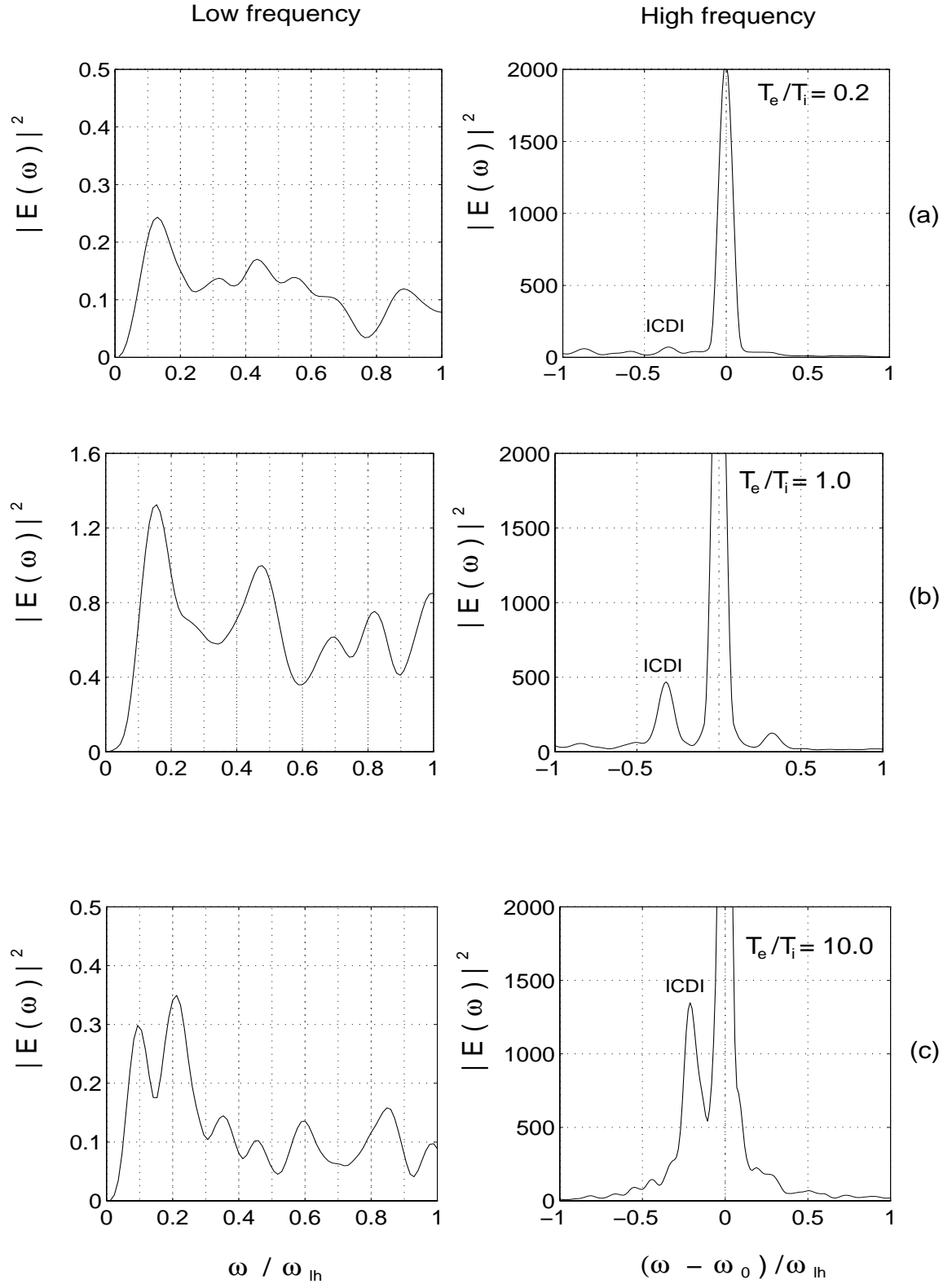


Figure 3.19: Three simulation runs showing the down-shifted sideband for the case $\omega_0 = 3\Omega_{ce} + 3\omega_{lh}$ and for (a) $T_e/T_i = 0.2$ (b) $T_e/T_i = 1.0$ (c) $T_e/T_i = 10.0$.

ELECTRON DENSITY

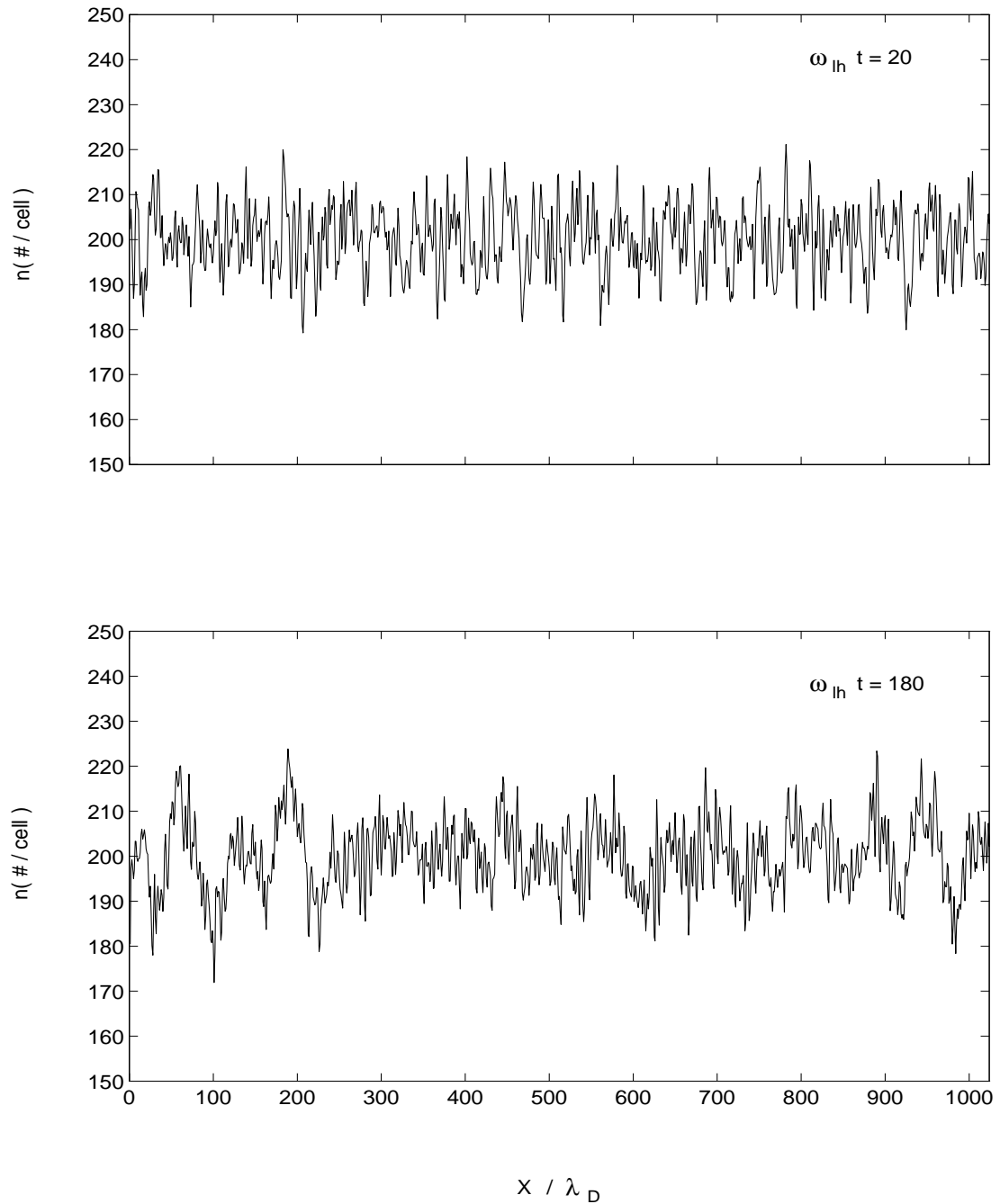


Figure 3.20: Simulation result showing the electron density and density irregularities in the simulation of the ICDI responsible for the DP.

ION DENSITY

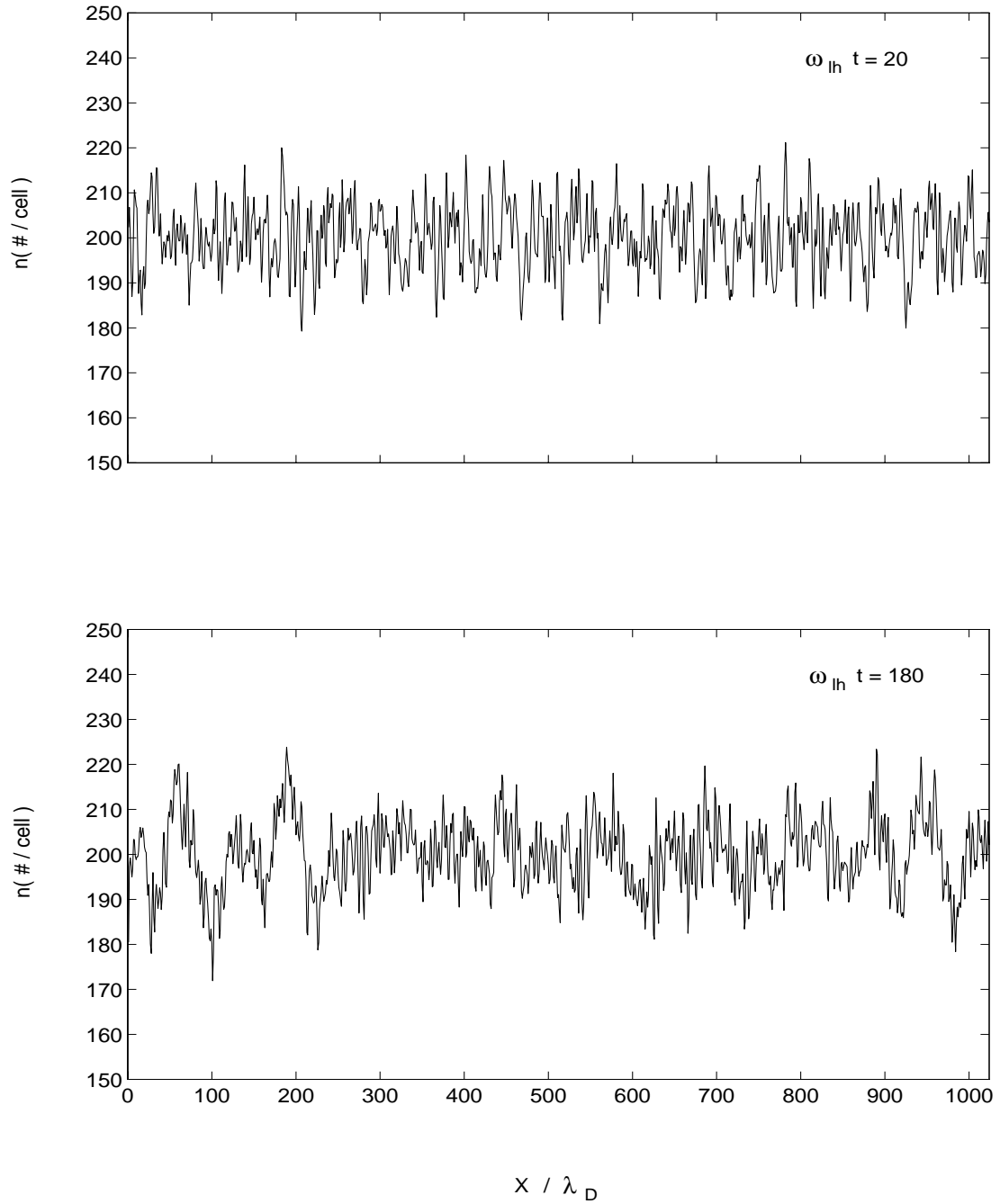


Figure 3.21: Simulation result showing the ion density and density irregularities in the simulation of the ICDI responsible for the DP.

ELECTRIC FIELD

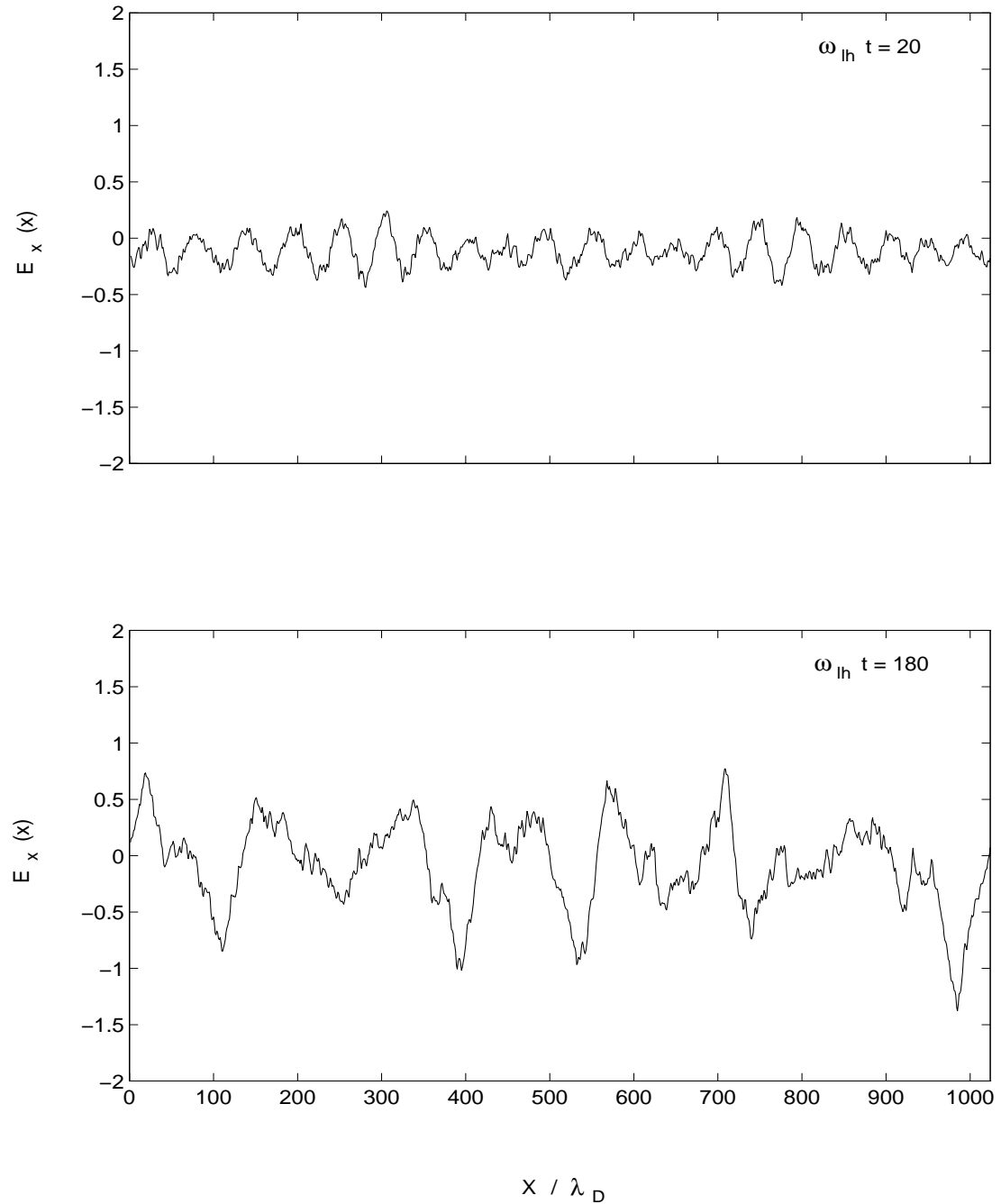


Figure 3.22: Simulation result showing the electric field strength in the simulation of the ICDI responsible for the DP.

ENERGY HISTORY

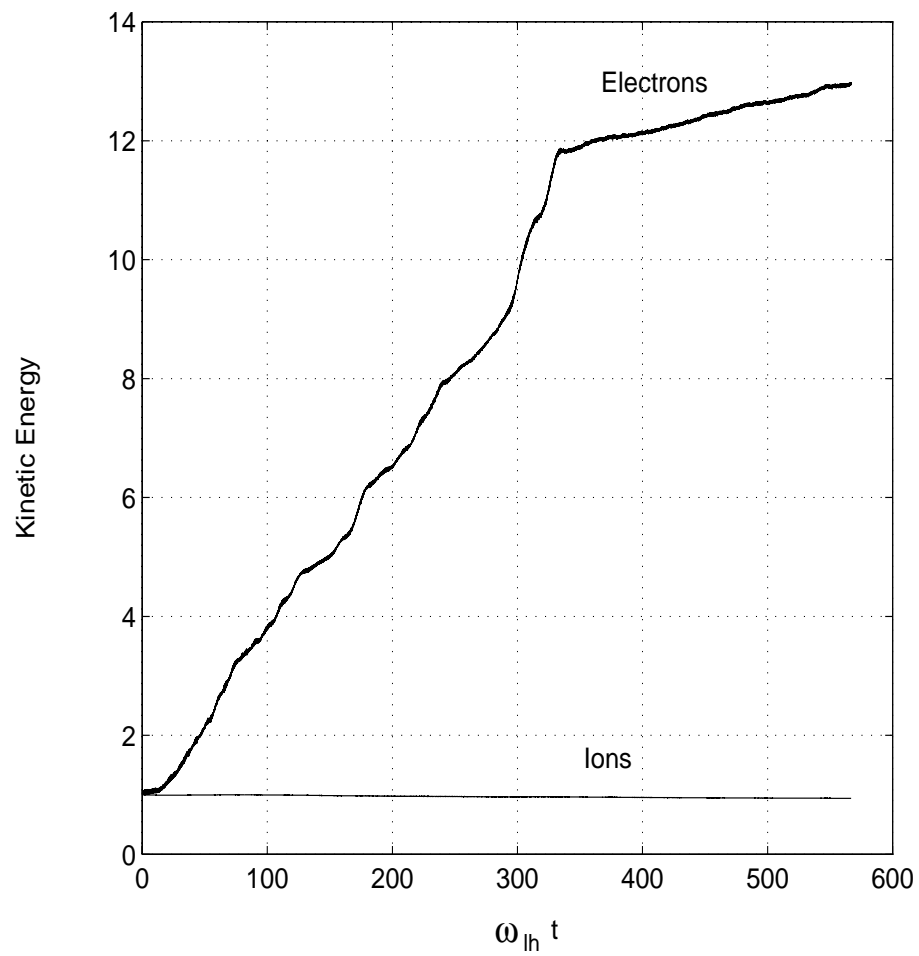


Figure 3.23: Simulation result showing the energy history of the kinetic energy for both the ions and electrons in the simulation of the ICDI responsible for the DP.

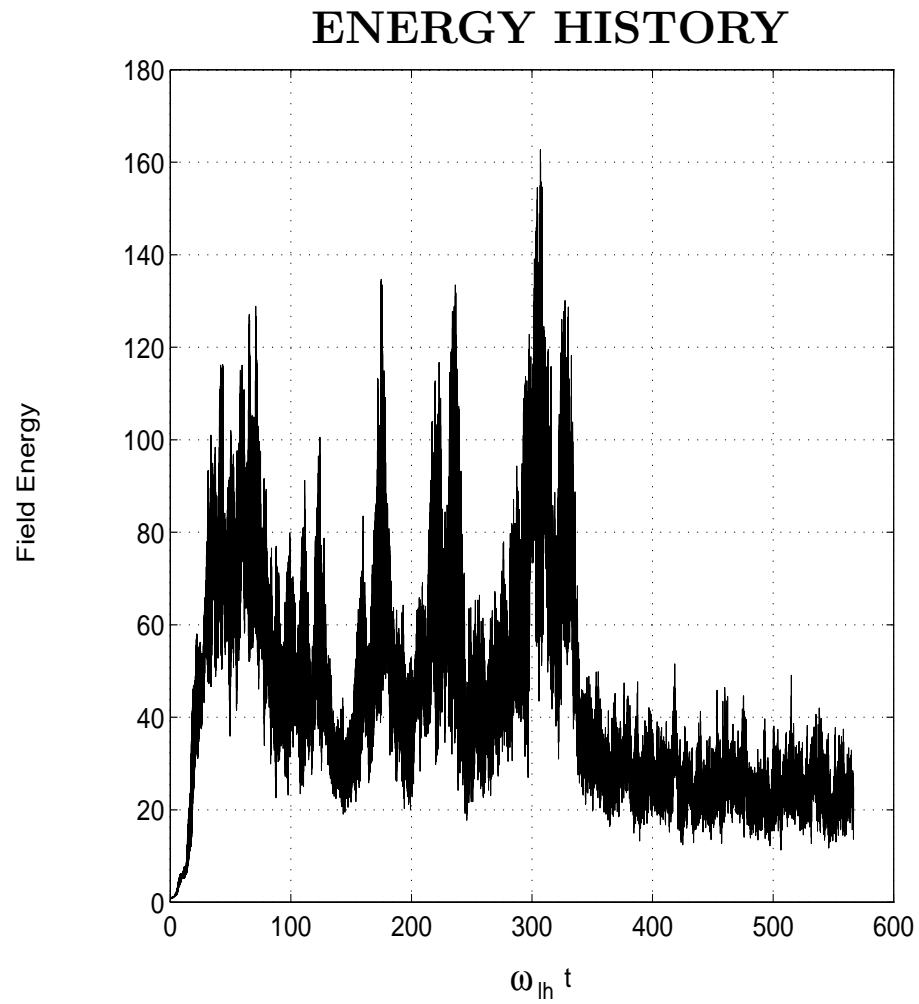


Figure 3.24: Simulation result showing the total field energy in the simulation of the ICDI responsible for the DP.

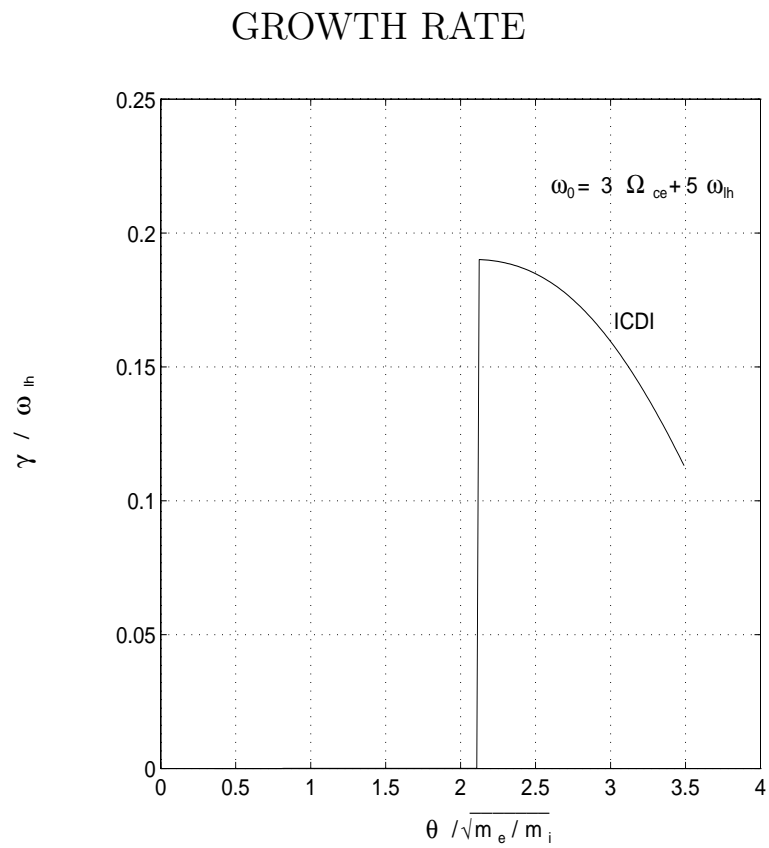


Figure 3.25: The growth rate versus angle for investigating the cascading of the ICDI for the case $\omega_{uh} = 3\Omega_{ce}$.

Simulation Electric Field Power Spectrum $|E(\omega)|^2$

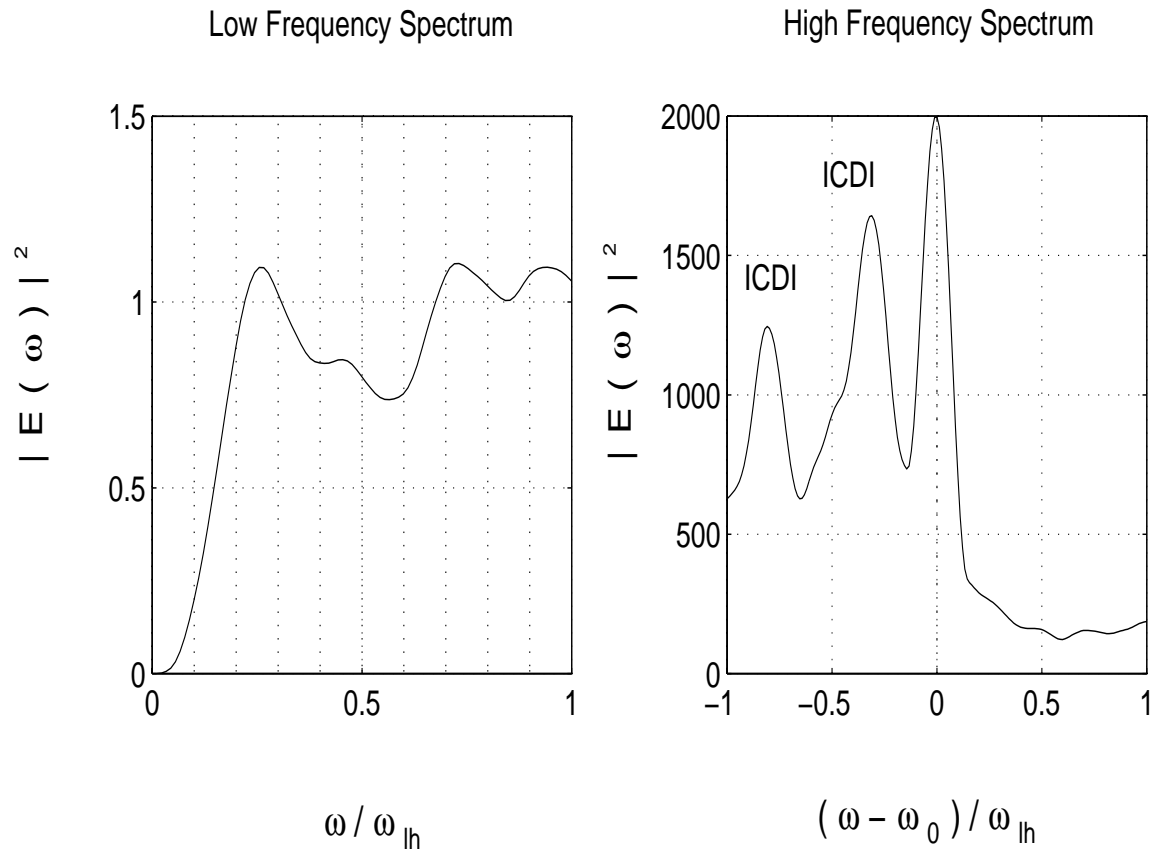


Figure 3.26: Simulation run showing the cascading of the down-shifted sideband corresponding to the ICDI for the case $\omega_0 = 3\Omega_{ce} + 5\omega_{lh}$ and $\omega_{uh} = 3\Omega_{ce}$.

3.5 Time evolution of the ICDI frequency spectrum

Three simulation electric field power spectra for the ICDI were taken at different time instants of the simulation. $\omega_0 = 3\Omega_{ce} + 3\omega_{lh}$ and $v_{osc}/v_{te} = 0.25$. The oscillating velocity was reduced in this case in order to get a better frequency resolution by running the simulation longer, since the ICDI is a narrow frequency band feature that requires good frequency resolution. Figure (3.27) shows the simulation electric field energy history. Figure (3.28.a) shows the simulation power spectrum in the linear growth rate regime where $\omega_{lh}t < 1000$. Figure (3.28.b) shows the simulation power spectra after the simulation has reached a steady state or equilibrium. Figure (3.28) shows that for the ICDI, in the weakly nonlinear regime and early in the simulation, the peak of the down-shifted sideband becomes narrower in frequency and moves closer to ω_0 as the simulation progresses, as predicted by the theory. Figure (3.28) shows that when the simulation electric field power spectrum is taken in the regime where strong nonlinearities take place the down-shifted sideband becomes narrower in frequency and moves closer to ω_0 it also becomes larger in amplitude.

Figure (3.29) shows three simulation results of the ICDI at the linear growth phase. It shows the development mechanism for the ICDI.

3.6 Summary

In this chapter, theoretical predictions were used to study the three-wave instability process responsible for the generation of the down-shifted sidebands, in particular the DM and the DP. The theory was very successful for providing us with the angular regime at which the sidebands develop as well as the frequency and wavenumber regimes of both the ICDI and the LHDI. The investigation involved studying the LHDI responsible for the DM and the ICDI responsible for the DP. It was also found that the ICDI was very sensitive to the temperature ratio T_e/T_i and the LHDI was essentially temperature independent. Looking at the simulation electric field power spectrum, it was found that the theory was very accurate in predicting the presence of the LHDI and ICDI at the appropriate regimes. It was also noted that, for the ICDI as T_e/T_i was increased the down-shifted sideband becomes narrower in frequency as well as the sideband gets closer to the heater frequency, as predicted by the theory. Time evolution of both the LHDI and the ICDI was also investigated. It was noted that for the LHDI, the amplitude and shape of the down-shifted sidebands in the simulation electric field power spectrum did not vary much if we take the spectrum in the linear growth rate regime or after the electric field energy has reached a steady state.

However, for the ICDI, if the simulation electric field power spectrum was taken in the strong nonlinear regime, the down-shifted sideband became larger in amplitude and the sideband moved closer to ω_0 and became narrower in frequency band. The saturation mechanism of the instability can be explained from a stand point of energy interchange between the electrostatic waves and the particles. Some electrons may be trapped in the potential wells of the electrostatic wave. Since the motion of the resonant particles (both trapped and untrapped) becomes periodic, we then expect the amplitude of the wave to oscillate, as it first gives and then recovers energy from the particles. In other words, first there are more electrons moving slightly slower than the phase velocity of the wave. The wave damps as the slower electrons gain energy. This leads to a situation in which there are now more electrons moving slightly faster than the wave phase velocity and the wave regains energy from the particles. The periodic interchange of energy between the wave and the particles reaches steady state and saturation takes place for the instability.

The theory prediction was also used to investigate and simulate the cascading of the LHDI and the ICDI. Particle heating and density irregularities were also observed to be associated with the three-wave instability in our simulations.

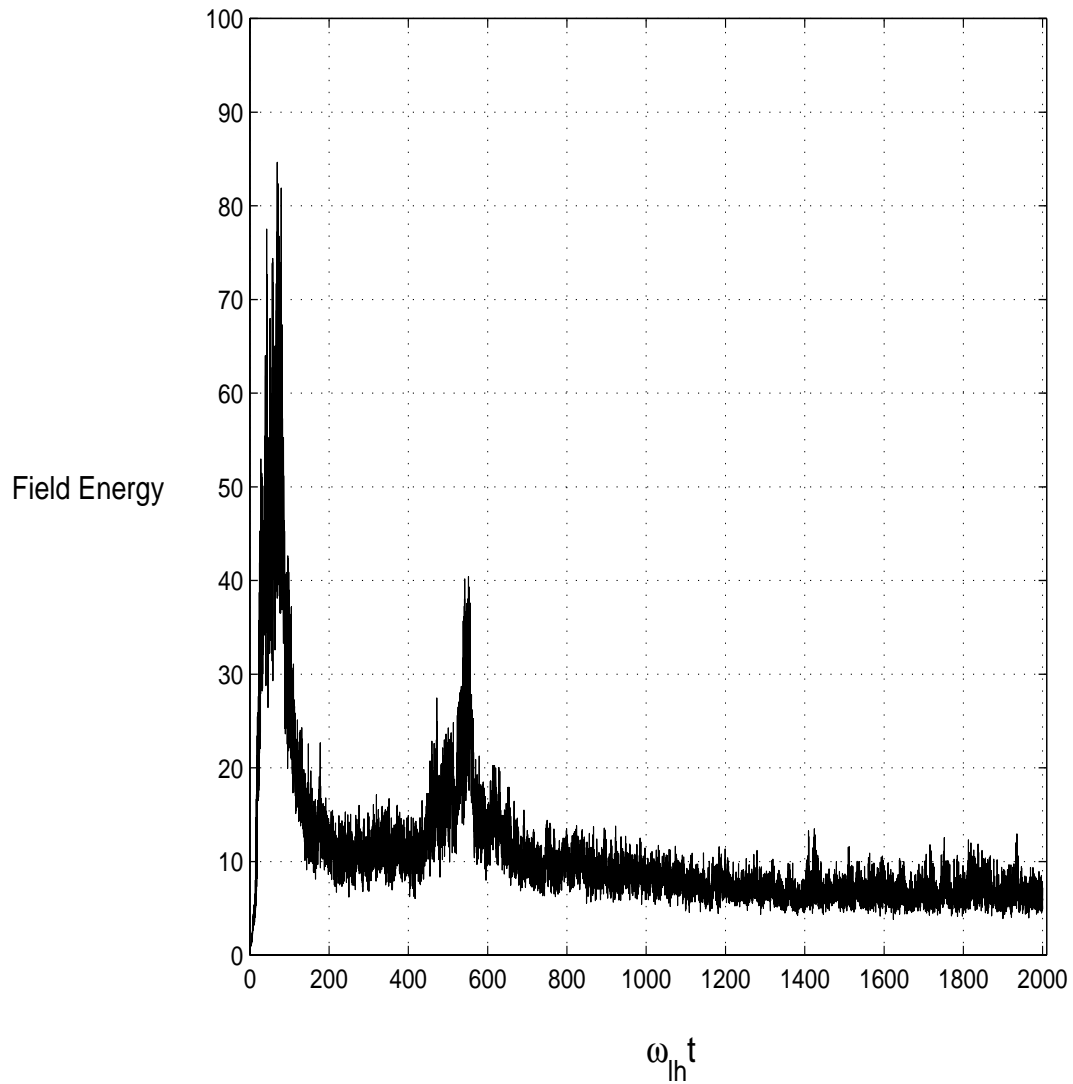
ENERGY HISTROY

Figure 3.27: The simulation electric field energy history for the simulation results of the ICDI shown in Figure (3.28,29).

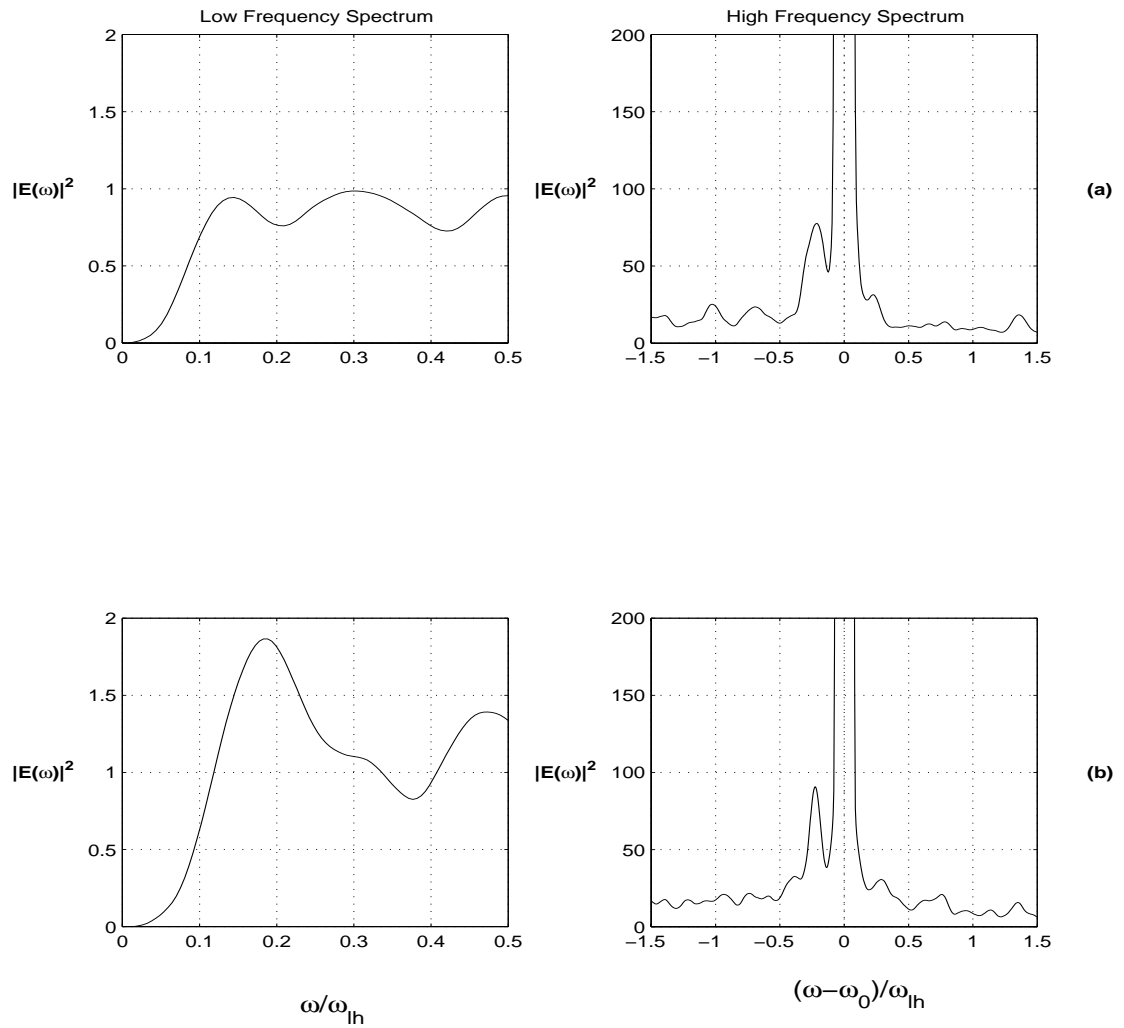


Figure 3.28: Three simulation results showing the simulation electric field power spectrum for the ICDI at different instants of time (a) $0 < \omega_{lh}t < 1000$ (b) $1000 \leq \omega_{lh}t < 2000$.

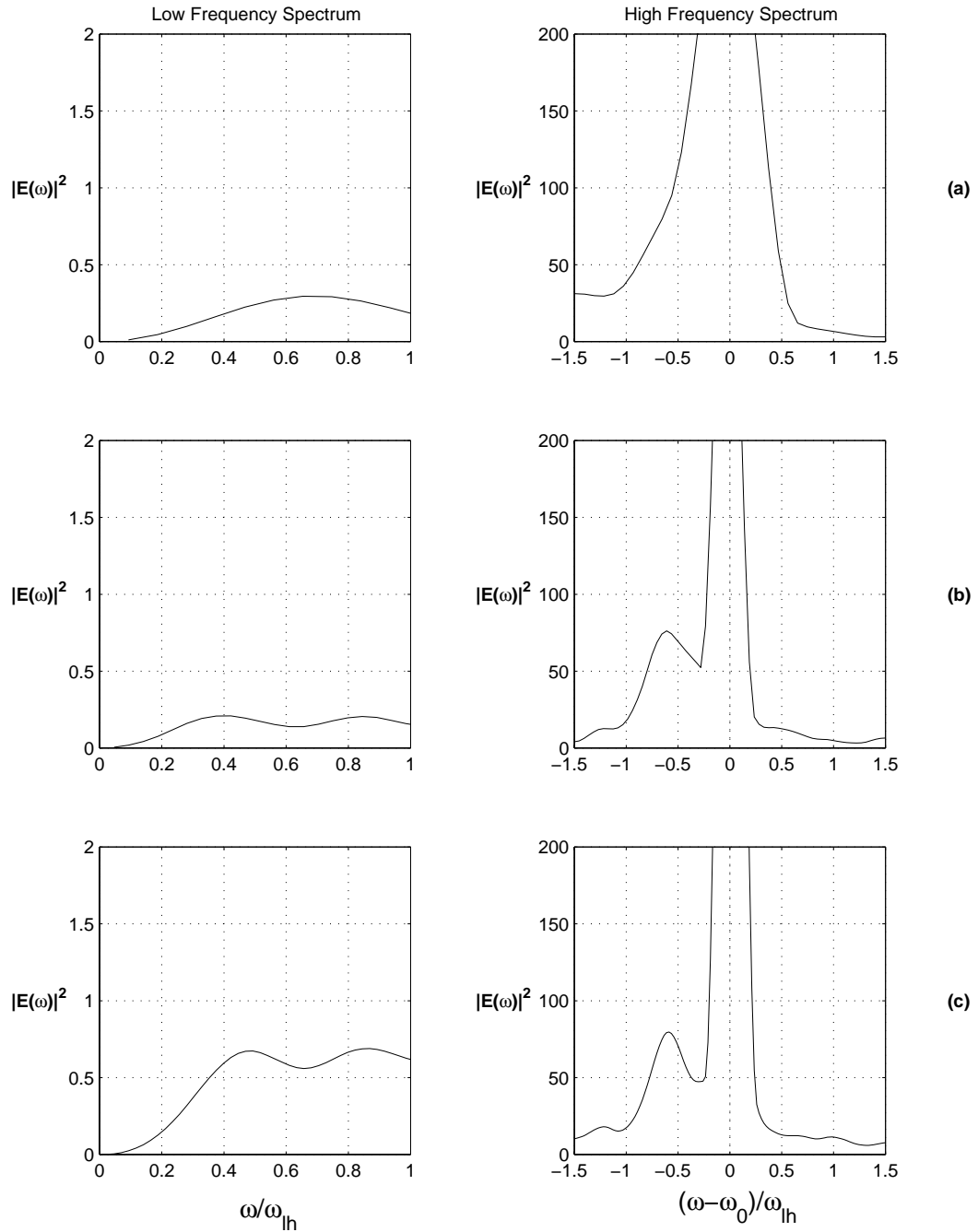


Figure 3.29: Three simulation results showing the simulation electric field power spectrum for the ICDI at different instants of time (a) $0 < \omega_{lh}t < 60$ (b) $60 \leq \omega_{lh}t < 200$ (c) $200 \leq \omega_{lh}t < 330$.

Chapter 4

Four-Wave Decay Instability

The most prominent up-shifted feature in the SEE spectrum is the broad up-shifted maximum BUM. The BUM is a broad upper sideband which extends more than 100 KHz above ω_0 [Leyser *et al.*, 1989, 1993, Stubbe *et al.* 1994]. The BUM is only seen when ω_0 is above $n\Omega_{ce}$. The frequency of the BUM peak is approximately given by the empirical formula $\omega_{BUM} = 2\omega_0 - n\Omega_{ce}$ for $n=3,4,5$ [Leyser *et al.*, 1989]. It was noted by Leyser *et al.* [1989] that the BUM feature could be generated through a four-wave interaction process involving two pump photons or upper hybrid plasmons, a decay mode at $n\Omega_{ce}$, and the stimulated radiation at ω_{BUM} . Huang and Kuo [1994] developed a theoretical model for the generation mechanism of the BUM in SEE which has been successful at interpreting some important aspects of the experimental observations. Huang and Kuo [1994] proposed that the BUM is produced in the altitude region where the pump frequency is near the mean of the upper hybrid wave frequency and the electron Bernstein wave frequency. Parametric interactions involving these wave modes produce a growing upper hybrid sideband. Nonlinear mixing of this electrostatic sideband with field-aligned ionospheric irregularities produces beat currents that radiate the SEE observed on the ground.

The object of this study is to present detailed comparisons between the predictions of the proposed theoretical model for the generation of the BUM in the SEE spectrum and numerical simulations and also to study the nonlinear development of the four-wave process.

4.1 Theory

The four-wave second order theoretical model developed by Huang and Kuo [1994] used to study the parametric process responsible for producing the BUM is described

as follows. In this proposed process, the long wavelength heater wave $(\omega_0, k_0 = 0)$ parametrically decays into a frequency down-shifted electron Bernstein wave (ω_1, k_1) , a frequency up-shifted upper hybrid wave (ω_2, k_2) along with a low frequency oscillation (ω_s, k_s) near the lower hybrid resonance frequency ω_{lh} . The wavevector and frequency matching conditions are given by $k_1 + k_s = 0$, $k_2 - k_s = 0$ and $\omega_1 + \omega_s^* = \omega_0 = \omega_2 - \omega_s$, where * denotes the complex conjugate. The dispersion relation for this process is given by

$$\epsilon_1^* \epsilon_2 - \frac{\beta_e^4}{16} \left\{ \frac{1}{\epsilon_s} [\chi_e(\omega_s) - \chi_e(\omega_2)] [\chi_e(\omega_s) - \chi_e(-\omega_1^*)] + \frac{1}{2} [\chi_e(-\omega_1^*) - 2\chi_e(\omega_s) + \chi_e(\omega_2)] \right\}^2 = 0 \quad (4.1)$$

where $\epsilon_{1,2} = 1 + \chi_e(\omega_{1,2})$ and $\epsilon_s = 1 + \chi_e(\omega_s) + \chi_i(\omega_s)$. The susceptibility of the j^{th} species χ_j is given by

$$\chi_j(\omega, k) = \frac{1}{k^2 \lambda_{Dj}^2} \left\{ 1 + \zeta_{j0} \sum_{n=-\infty}^{\infty} \Gamma_n(b_j) Z(\zeta_{jn}) \right\} \quad (4.2)$$

where $\beta_e = 2kv_{osc}/(\omega_0 + \Omega_{ce})$, $v_{osc} = qE_0/m_e\omega_0$ is the electron oscillating velocity, k is the wavenumber, m_e the electron mass, E_0 is the electric field strength, q is the electron charge, $b_j = k_{\perp}^2 \rho_j^2 / 2$, ρ_j is the gyroradius, $\zeta_{jn} = (\omega - n\Omega_{cj})/k_{\parallel} v_{tj}$, Ω_{cj} is the cyclotron frequency, v_{tj} is the thermal velocity, $\Gamma_n(b_j) = I_n(b_j) \exp(-b_j)$, Z is the Fried Conte function, I_n is the modified Bessel function of the first kind of order n , λ_{Dj} is the Debye length, $k_{\parallel}(k_{\perp})$ is the component of k parallel (perpendicular) to the magnetic field B .

We have solved the dispersion relation in (4.1) numerically using the method of *Rönnmark* [1983] for a variety of parameter regimes [Appendix E]. The case $4\Omega_{ce} < \omega_0 < \omega_{uh}$ is considered in detail here. The frequency separation between ω_{uh} and $4\Omega_{ce}$ is chosen to be $6\omega_{lh}$. In this case, ω_0 is chosen to be at the mean value of ω_{uh} and $4\Omega_{ce}$, $\omega_0 = 4\Omega_{ce} + 3\omega_{lh}$, as predicted by *Huang and Kuo* [1994]. The ion-electron mass ratio $m_i/m_e = 400$ and $v_{osc}/v_{te} = 0.275$ in this case (for comparisons to the simulations to be discussed shortly). Figure (4.1) shows the dispersion relation for the upper hybrid and the electron Bernstein modes and the location of the pump frequency ω_0 for this case. For given values of ω_0 and ω_{uh} , the dispersion relation in (4.1) is solved to obtain the propagation angle with respect to the direction perpendicular to B for maximum growth θ_{max} . In this case, the angle is found to be $\theta_{max} \simeq 3.0\sqrt{m_e/m_i}$. The result in Figure (4.2) shows the growth rate γ versus angle θ for the case $\omega_0 = 4\Omega_{ce} + 3\omega_{lh}$. The growth rate γ at θ_{max} is calculated and plotted versus wavenumber $k_{\perp}\rho_e$. The

result is also shown in Figure (4.1) which shows the wavelength regime for the four-wave process. The maximum growth occurs for $k_{\perp}\rho_e \simeq 0.3$, where $\gamma/\omega_{lh} \simeq 0.008$. Figure(4.3) shows the growth rate γ versus frequency for the same case.

A number of theoretical calculations were done by stepping the heater frequency ω_0 closer to ω_{uh} . The pump frequency was stepped from $2\omega_{lh}$ to about $5\omega_{lh}$ above $4\Omega_{ce}$. The growth rate γ was calculated in each case at the angle of maximum growth. The result shows that as we get closer to ω_{uh} , γ increases considerably. The result is shown in Figure (4.4). It was also noted that, as ω_0 is stepped closer to ω_{uh} , the angle of maximum growth θ_{max} decreases. The result is shown in Figure (4.5). Figure (4.6) shows that the maximum growth rate shifts to a higher frequency as ω_0 is moved away from ω_{uh} . Figure (4.7) shows that the maximum growth rate of the four-wave process moves to a shorter wavelength as ω_0 is stepped closer to ω_{uh} .

4.2 Simulation Results

Many simulation runs have been conducted for the up-shifted sideband using the same simulation model discussed earlier. The system length is $1024\lambda_D$ with a uniform density of 400 particles per grid cell for each species. The total number of particles in the simulation is 819200. The mass ratio $m_i/m_e = 400$ which provides sufficient separation of the ion and electron timescales. The ions and electrons are initialized with Maxwellian velocity distributions and $T_e = T_i$. Note that this artificially large value (as well as the artificially small mass ratio) allows the simulation to run in a reasonable amount of CPU time and will not make qualitative physics changes. The simulation runs for up to 1.2×10^6 time steps corresponding to an end time $\omega_{lh}t = 3000$ (corresponding to a real time of approximately 100 milliseconds) and at least 3.5 growth periods of the four-wave interaction process to allow for a steady state to take place and sufficient frequency resolution. The angle of propagation θ_{max} corresponding to the angle of maximum growth in Figure (4.2) described in the previous section is used for the simulation.

As shown in Figure (4.1), ω_0 is chosen to be $\omega_0 = 4\Omega_{ce} + 3\omega_{lh}$ and $v_{osc}/v_{te} = 0.275$. Figure (4.8) shows the total electric field energy history during the simulation. It shows that the field energy reaches a steady state at time corresponding to $\omega_{lh}t \simeq 1000$. It also shows that the simulation runs for up to 3.5 growth periods of the four-wave process. Figure (4.9) shows the kinetic energy history for both the ions and the electrons. Note the increase in the kinetic energy for the electrons due to wave-particle heating. The simulation electric field power spectrum is shown in Figure (4.10). Note that the simulation spectrum is taken after the simulation has reached a steady state, $1000 < \omega_{lh}t < 1750$. We observe a broad sideband up-shifted from the pump frequency which corresponds to the excited upper hybrid wave. The lower frequency

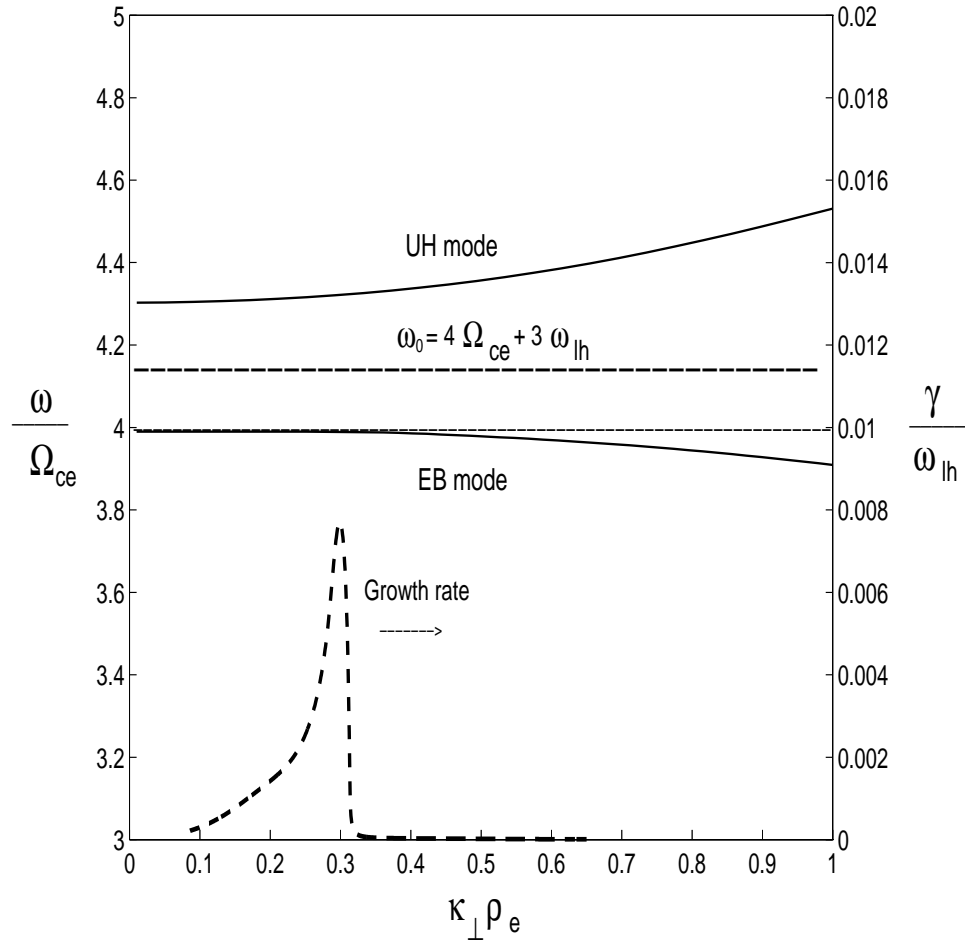


Figure 4.1: A plot of the growth rate γ in equation (4.1) vs wavelength $k_{\perp}\rho_e$ and the dispersion relation for both the upper hybrid and the electron Bernstein modes for the case $\omega_0 = 4\Omega_{ce} + 3\omega_{lh}$, $\theta_{max} \simeq 3.0\sqrt{m_e/m_i}$ and $v_{osc}/v_{te} = 0.275$.

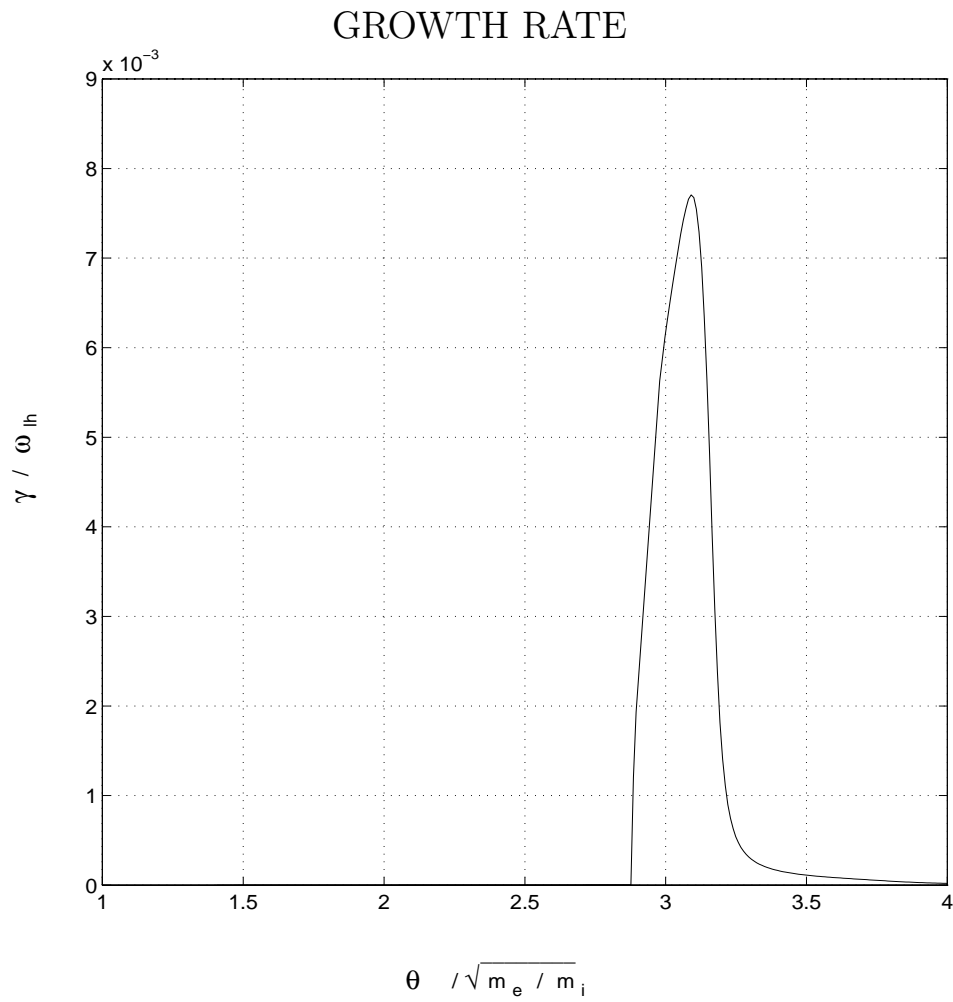


Figure 4.2: A plot of showing the growth rate γ in equation (4.1) vs θ for the case $\omega_0 = 4\Omega_{ce} + 3\omega_{lh}$ and $v_{osc}/v_{te} = 0.275$.

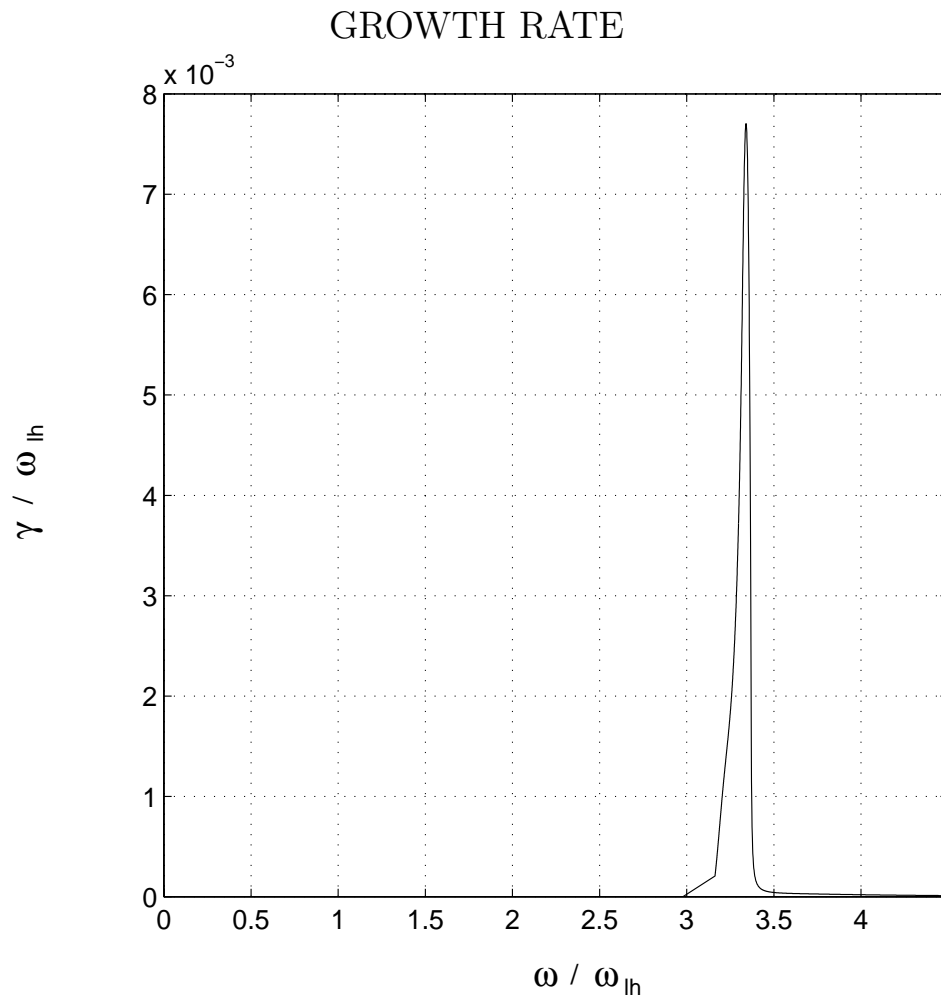


Figure 4.3: A plot of showing the growth rate γ in equation (4.1) vs ω for the case $\omega_0 = 4\Omega_{ce} + 3\omega_{lh}$, $\theta_{max} \simeq 3.07\sqrt{m_e/m_i}$ and $v_{osc}/v_{te} = 0.275$.

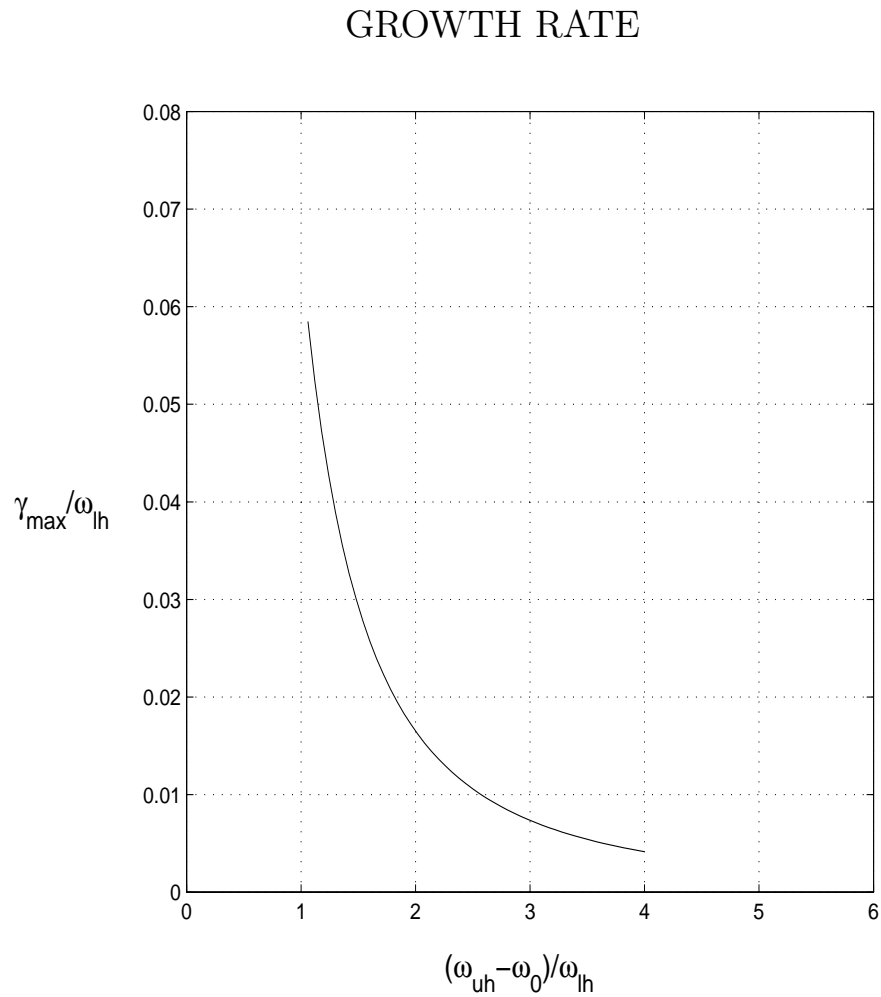


Figure 4.4: A plot showing the variation of the growth rate γ as the pump frequency ω_0 is stepped close to the upper hybrid resonance frequency ω_{uh} for the case $\theta = \theta_{max}$ and $v_{osc}/v_{te} = 0.275$.

GROWTH RATE

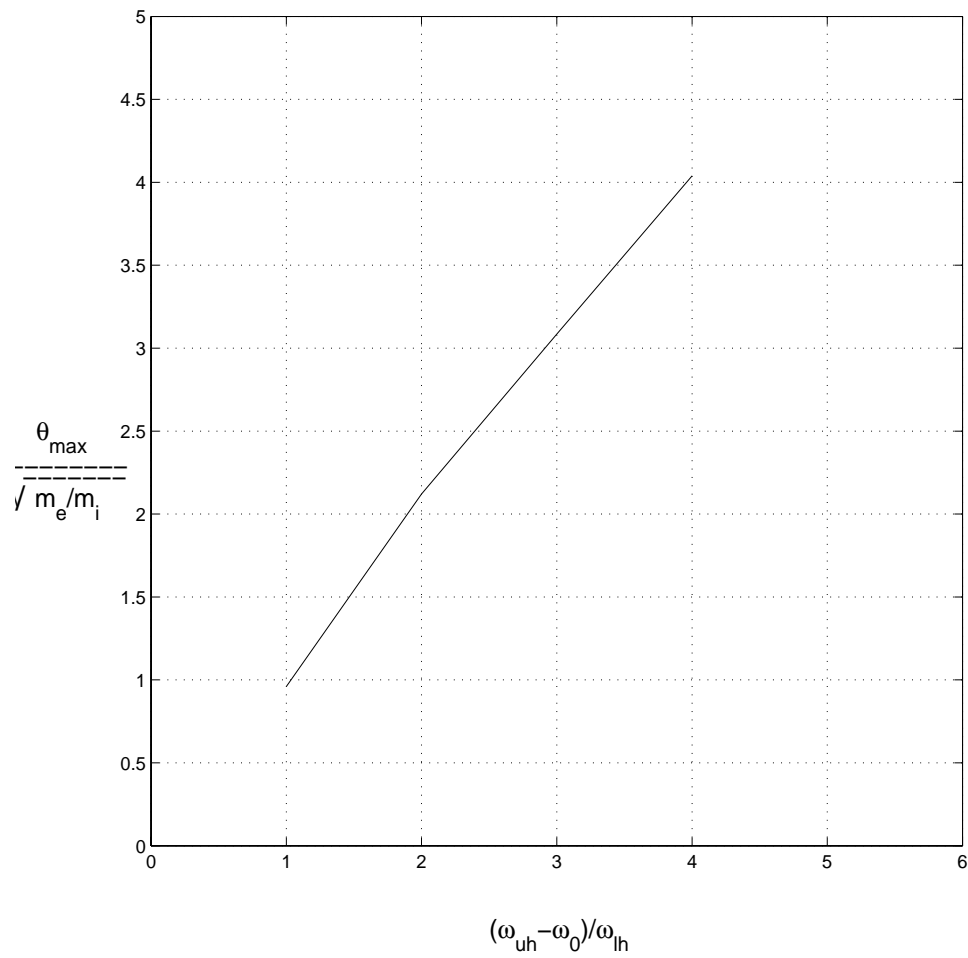


Figure 4.5: A plot showing the variation of the angle of maximum growth θ_{max} as the pump frequency ω_0 is stepped close to the upper hybrid resonance frequency ω_{uh} for the case $v_{osc}/v_{te} = 0.275$.

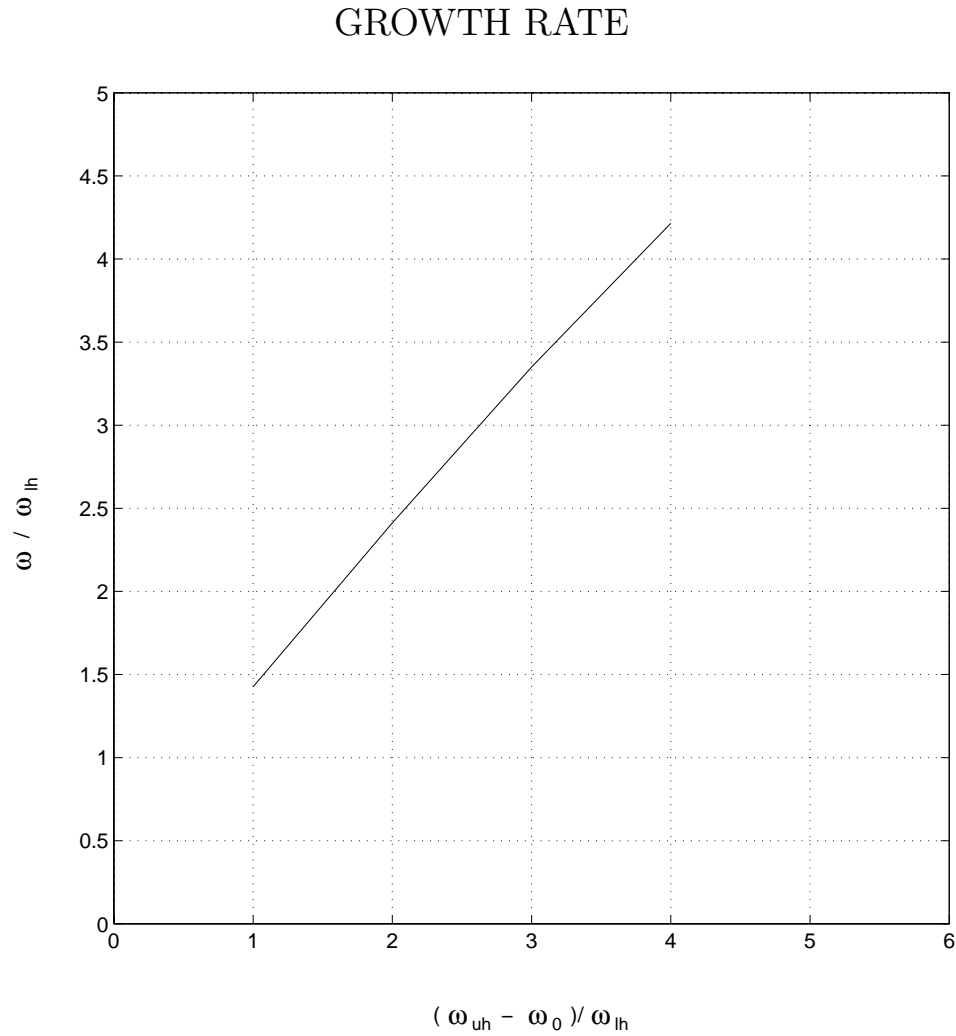


Figure 4.6: A plot showing the variation of the frequency at maximum growth rate as the pump frequency ω_0 is stepped close to the upper hybrid resonance frequency ω_{uh} for the case $\theta = \theta_{max}$ and $v_{osc}/v_{te} = 0.275$.

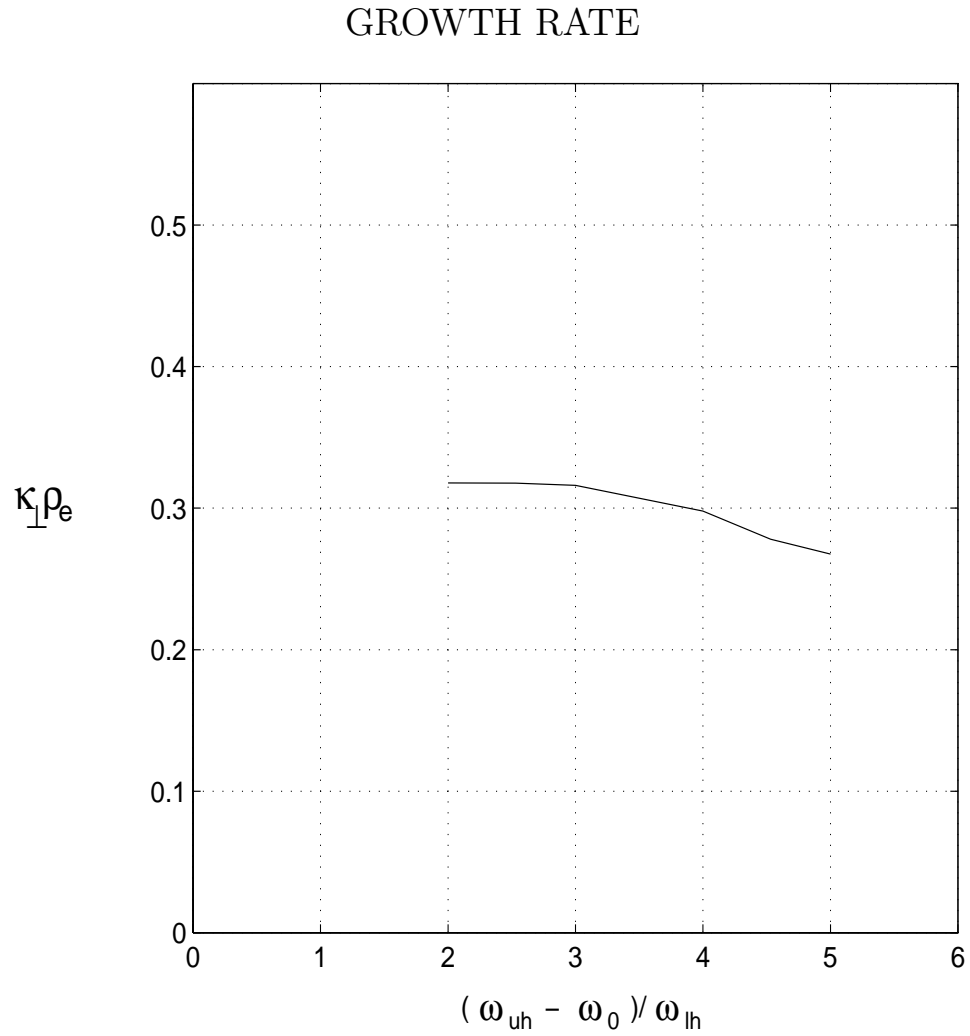


Figure 4.7: A plot showing the variation of the wavenumber at maximum growth rate as the pump frequency ω_0 is stepped close to the upper hybrid resonance frequency ω_{uh} for the case $\theta = \theta_{max}$ and $v_{osc}/v_{te} = 0.275$.

cutoff is approximately $\omega_0 + 4\omega_{lh}$ and the frequency band is approximately $7\omega_{lh}$. The low frequency spectrum shows a wave at the lower hybrid wave frequency $\omega \simeq \omega_{lh}\sqrt{1 + \sin^2(\theta_{\max})m_i/m_e}$. The spectrum also shows a narrower bandwidth smaller amplitude down-shifted sideband which corresponds to the electron Bernstein wave. The down-shifted sideband may be responsible for the so-called Broad Downshifted Maximum BDM often observed during experiments, Figure(2.9).

The result in Figure (4.10) shows the frequency up-shifted, upper hybrid, frequency down-shifted, electron Bernstein, and the low frequency, lower hybrid, waves. Figure (4.10) indicates that the frequency matching condition is satisfied.

Figure (4.11) and (4.12) show the development of cavities in the ions and electrons densities during the simulation run with the electric field power spectrum shown in Figure (4.10). Figure (4.13) shows the electric field during the same simulation run early and towards the end of the simulation.

In order to check the wavenumber matching conditions, an interferogram [Lin *et al.*, 1982] [Appendix F] is constructed in which we compute

$$E_x(x, \tau) = \frac{1}{T} \int_0^T \sin(\omega_d t) E_x(x, t + \tau) dt \quad (4.3)$$

where ω_d is either the up-shifted, down-shifted or the low frequency wave frequencies. The result in Figure (4.14) shows that the wavelength of both the up-shifted and down-shifted sidebands are comparable to that of the low frequency wave which shows good agreement with the theoretical prediction.

4.3 Time evolution of the four-wave decay frequency spectrum

Figure (4.15) shows the simulation electric field power spectrum for the case $\omega_0 = 4\Omega_{ce} + 3\omega_{lh}$ and $v_{osc}/v_{te} = 0.275$ at different time instants. It shows that, in the regime where $\omega_{lh}t < 1000$, where the waves are growing and steady state has not been reached yet, the broad down-shifted sideband has an amplitude comparable to that of the broad up-shifted sideband. This result is shown in Figure (4.15.a). As we take the simulation electric field power spectrum in the regime where the simulation has reached a steady state and the waves are not growing any more (this corresponds to the case of an actual experiment), the down-shifted sideband has an amplitude at least 10 dB below the up-shifted sideband. This result agrees with the experimental observations. The result is shown in Figure (4.15.b,c).

ENERGY HISTORY

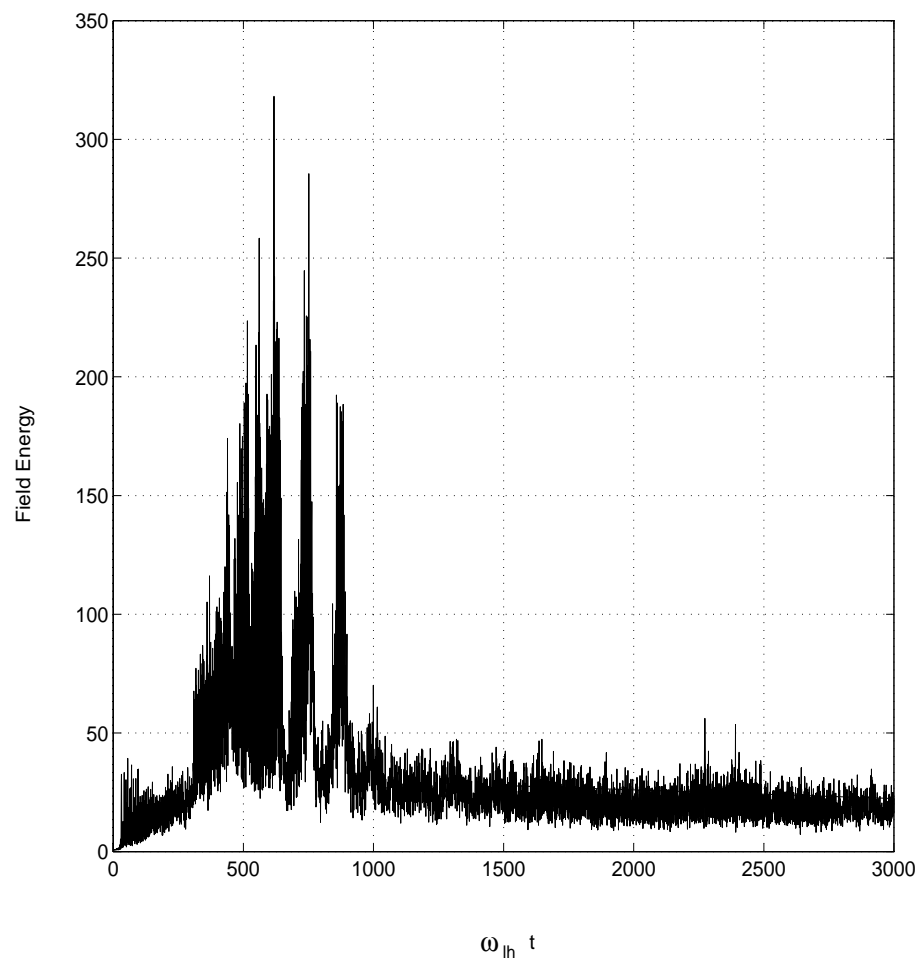


Figure 4.8: Simulation result showing the total field energy history in the simulation of the up-shifted sidebands.

ENERGY HISTORY

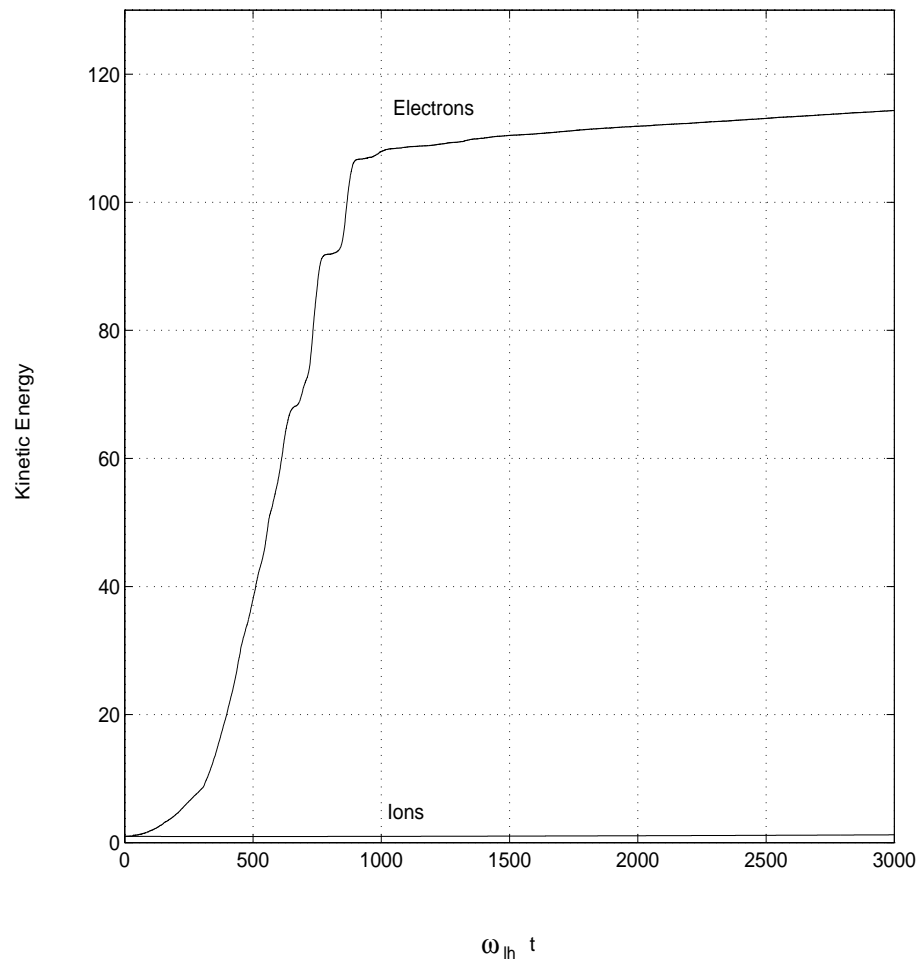


Figure 4.9: Simulation result showing the kinetic energy history for both the ions and electrons in the simulation of the up-shifted sidebands.

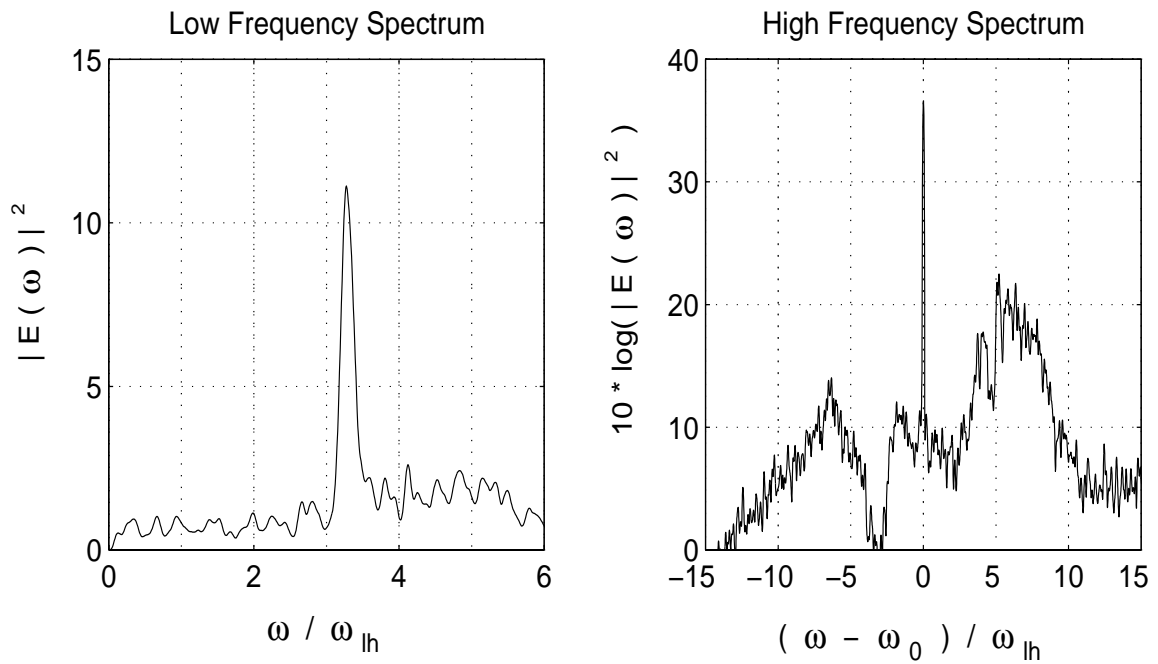


Figure 4.10: Simulation electric field power spectrum showing the broad up-shifted spectral feature and the low frequency lower hybrid wave produced by the four-wave decay process described in Figure (4.1).

ELECTRON DENSITY

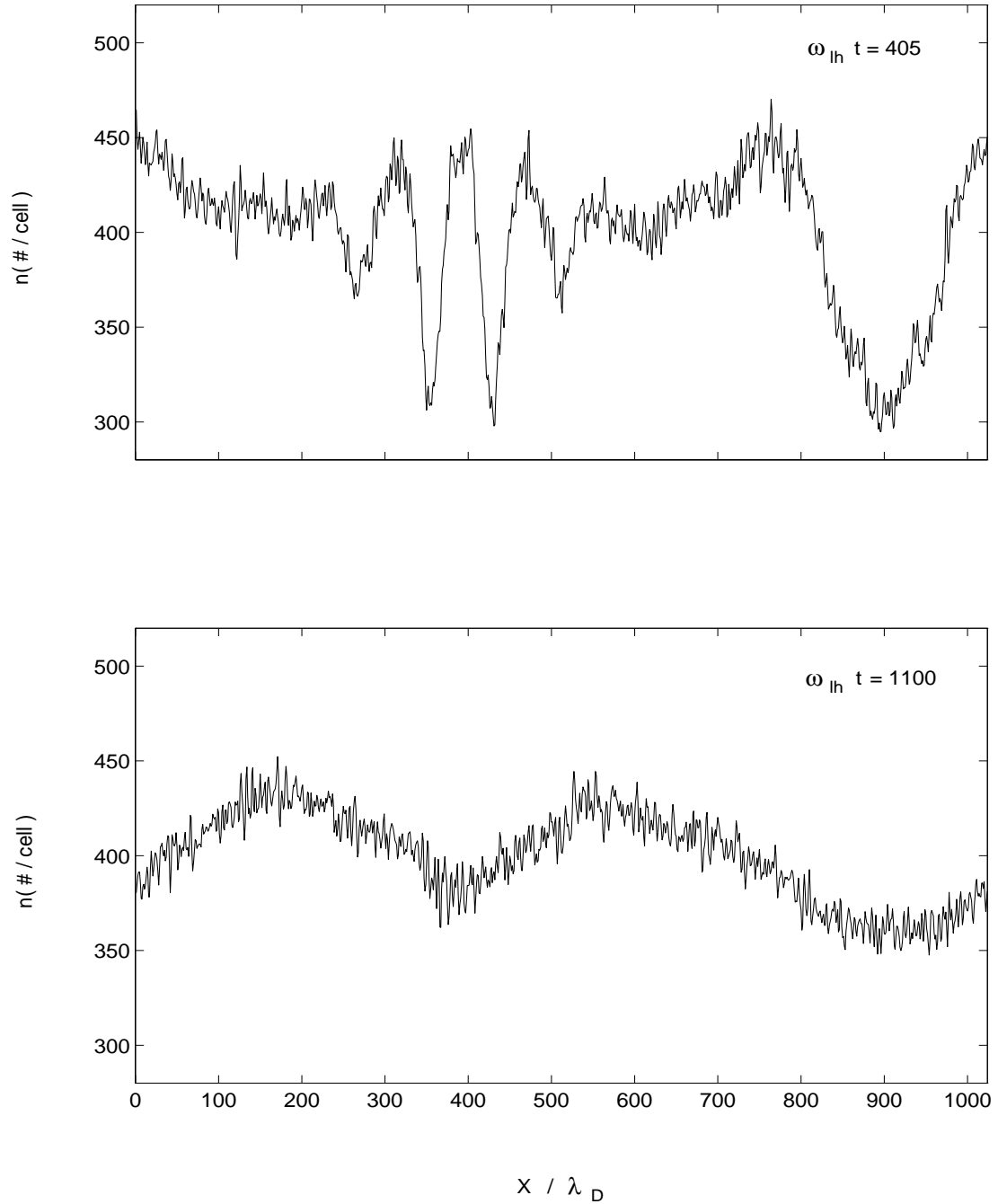


Figure 4.11: Simulation result showing the electron density and the development of density cavities in the simulation of the up-shifted sidebands.

ION DENSITY

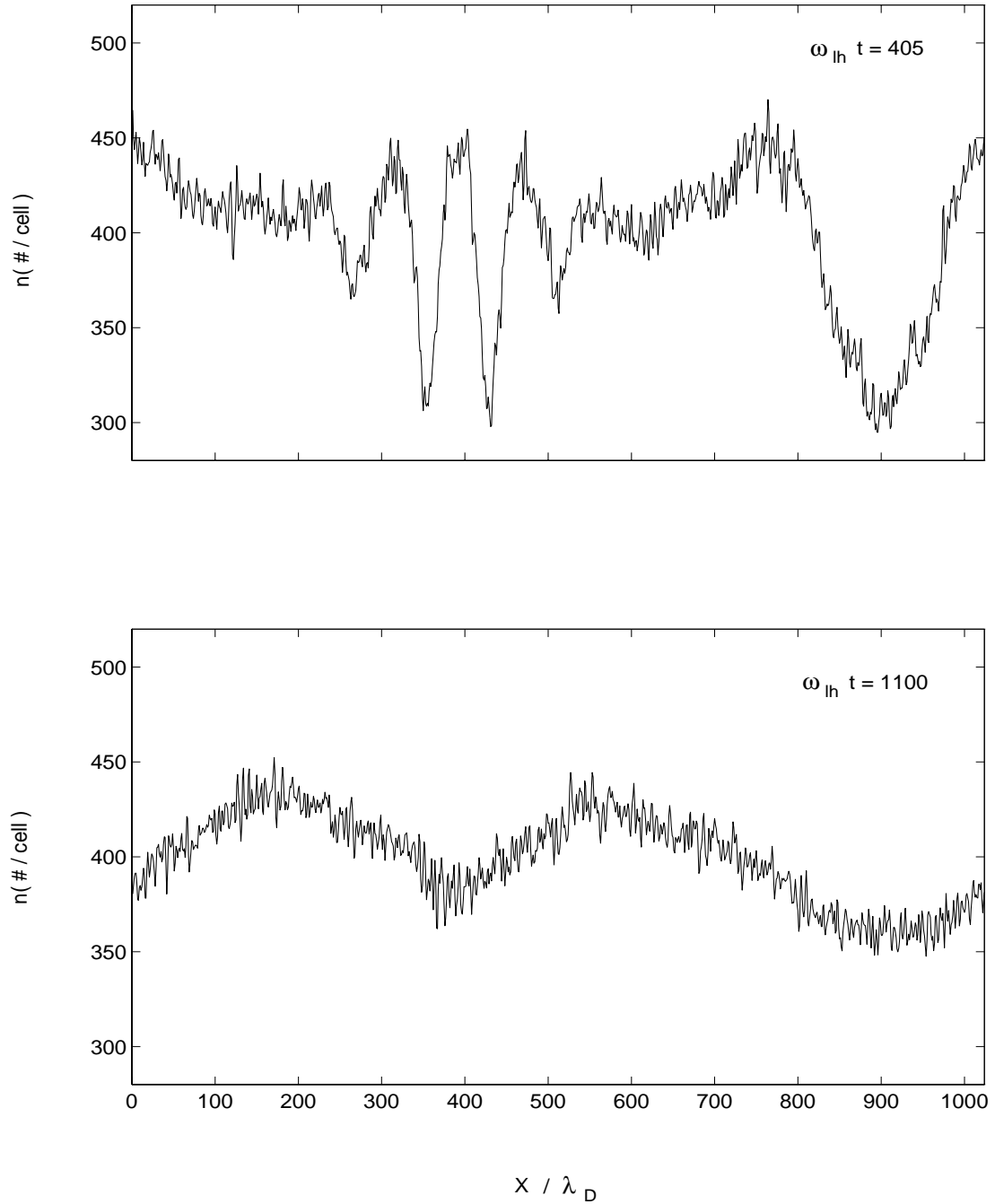


Figure 4.12: Simulation result showing the ion density and the development of density cavities in the simulation of the up-shifted sidebands.

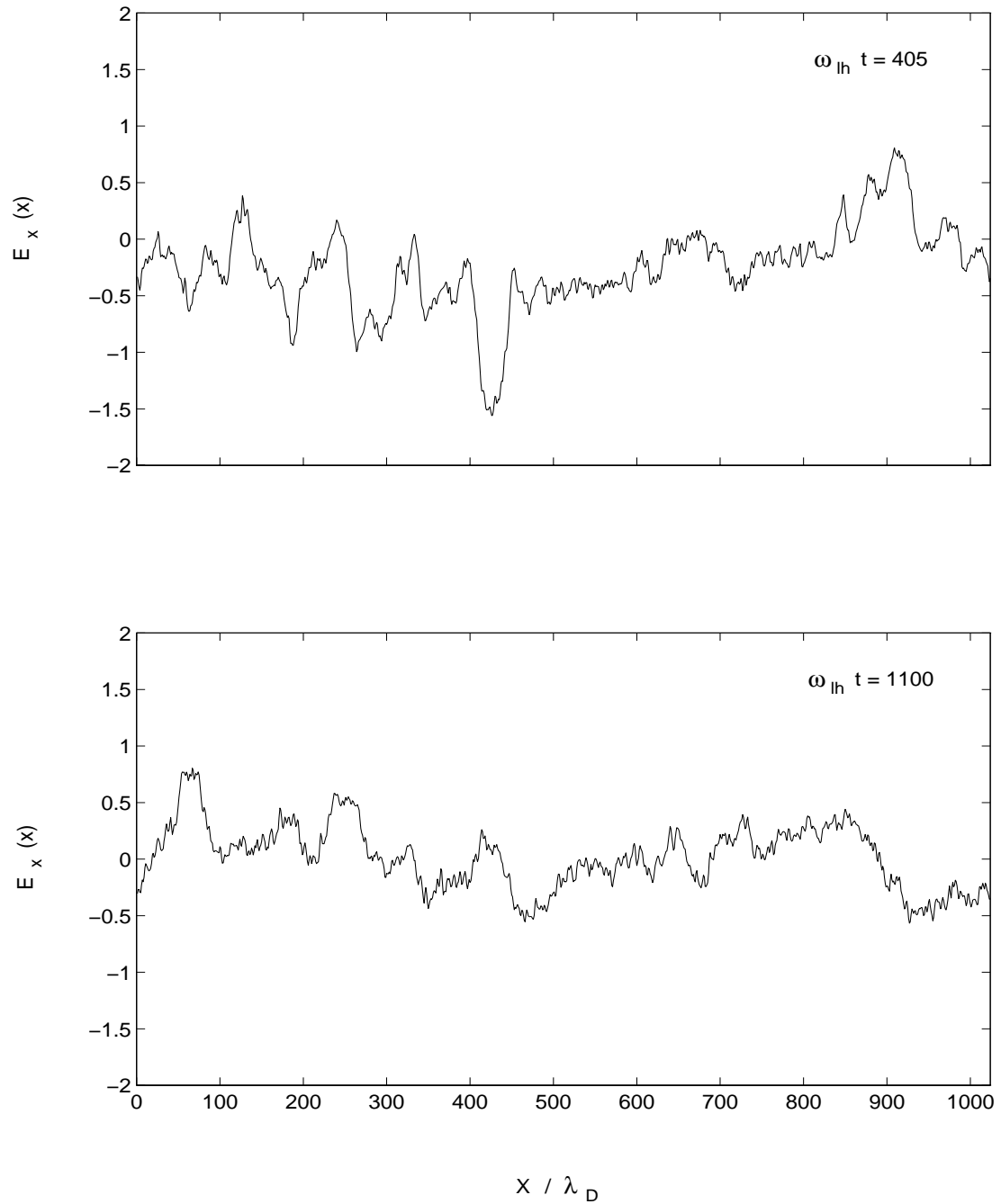
ELECTRIC FIELD

Figure 4.13: Simulation result showing the electric field strength in the simulation of the up-shifted sidebands.

Three simulation electric field power spectra in the linear growth rate regime of the four-wave process ($\omega_{lh}t < 1000$ in Figure(4.8)) were obtained to show the growing mechanism for both the up-shifted and down-shifted sidebands. The result is shown in Figure (4.16). It shows that both the up-shifted and down-shifted sidebands initially have a comparable growth rate which agrees with the theory of *Huang and Kuo*, [1994]. Figure (4.17) shows the time evolution of the peak amplitude for both the up-shifted and down-shifted sidebands. It shows that as the simulation reaches a steady state (corresponding to $\omega_{lh}t > 1000$), the peak amplitude of the down-shifted sideband drops significantly below that of the up-shifted sideband. Our explanation for that, is that the electron Bernstein mode (the down-shifted sideband) in the strong nonlinearity regime is cyclotron damped.

4.4 Cyclotron damping

When a particle moving along B_0 in a wave with finite k_z , parallel component of k to B_0 , has the right velocity, it sees a Doppler-shifted frequency $\omega - k_z v_z$ equal to $n\Omega_c$ and is therefore accelerated by the electric field E_\perp of the wave. Those particles with the right phase relative to E_\perp will gain energy and those with the wrong phase will lose energy. Since the energy change is the force times the distance, the faster accelerated particles will gain more per unit time than what the slower decelerated particles lose. Therefore the particles will have a net gain of the energy, on the average, at the expense of the wave energy; and the wave is damped.

4.5 Summary

In this chapter, a four-wave parametric instability process thought to be responsible for SEE broad up-shifted sideband spectral features was discussed using theoretical and numerical simulation models. Many theoretical results were presented, in which the heater frequency was stepped closer to the upper hybrid resonance frequency and the growth rate of the four-wave decay process was calculated. It was found that as ω_0 is stepped closer to ω_{uh} , the angle of maximum growth rate θ_{max} decreases at the same time the growth rate at this angle γ_{max} increases. It was also noted that as the heater frequency is moved closer to ω_{uh} , the four-wave process shifts to a higher frequency and to a shorter wavelength. The growth rate results were also useful in guiding the simulation results by providing us with the parameters for the four-wave process responsible for the up-shifted sidebands. We found good agreement between the predictions of the theoretical model and numerical simulations. The simulation electric field power spectrum showed a large amplitude up-shifted sideband and a

much smaller amplitude down-shifted sideband, similar to the experimental observations. The simulation electric field power spectrum was taken in the time interval where the electric field energy has reached steady state. It was found that if the electric field power spectrum was taken in the regime where the waves are still growing and have not reached a steady state, the up-shifted and down-shifted sidebands would start growing together with almost the same growth rate and the same relative amplitude.

The results we presented are very encouraging for having the potential of complementing the experimental observations and the theoretical analysis. The development of density irregularities, cavities and particle heating were also observed to be associated with the four-wave instability in our simulations.

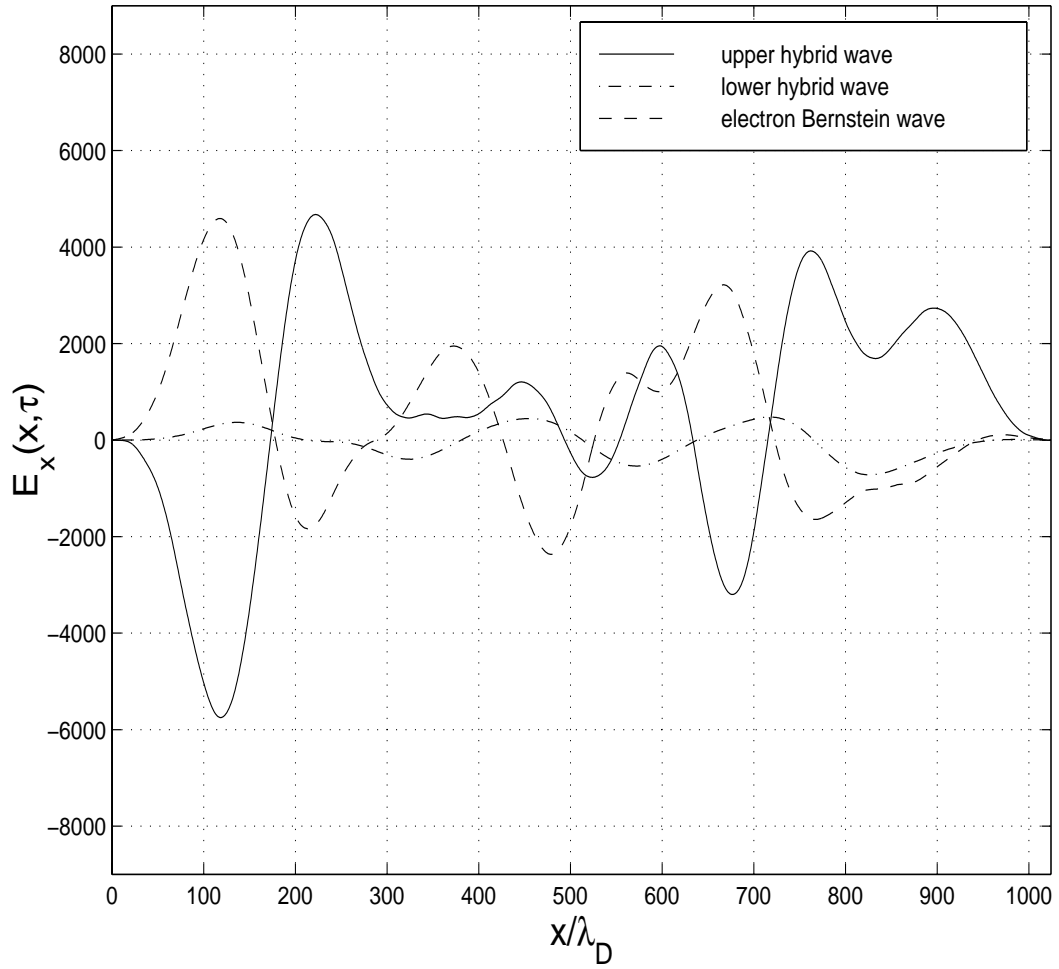


Figure 4.14: An interferogram verifying the wavenumber matching for the four-wave interaction process responsible for the up-shifted sideband shown in Figure (4.10) in the interval $500 < \omega_{\text{h}}t < 505$.

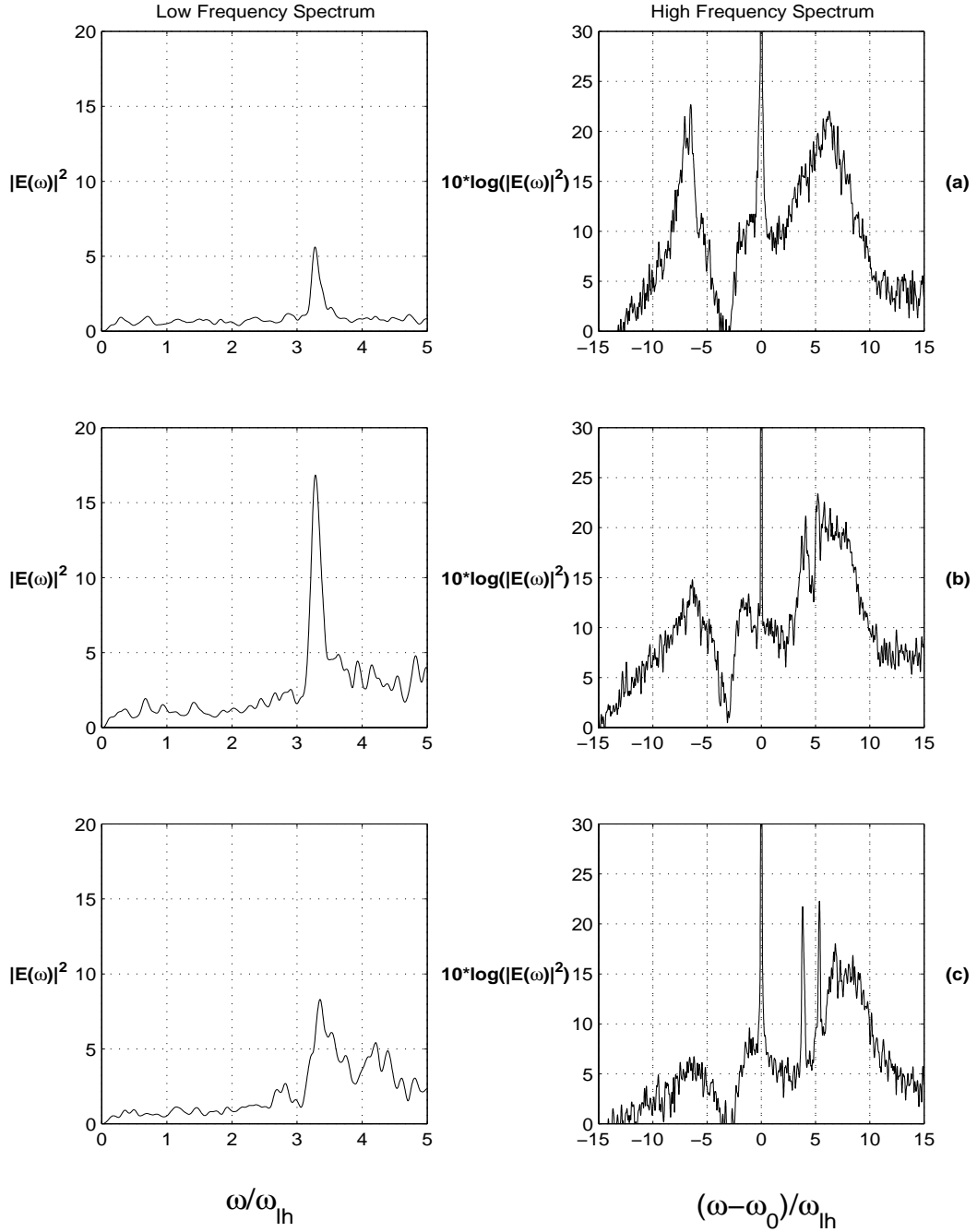


Figure 4.15: Simulation electric field power spectra showing time evolution of the broad up-shifted and broad down-shifted spectral features at different time instants for the cases (a) $0 < \omega_{lh}t < 1000$ (b) $1000 \leq \omega_{lh}t < 2000$ (c) $2000 \leq \omega_{lh}t < 3000$.

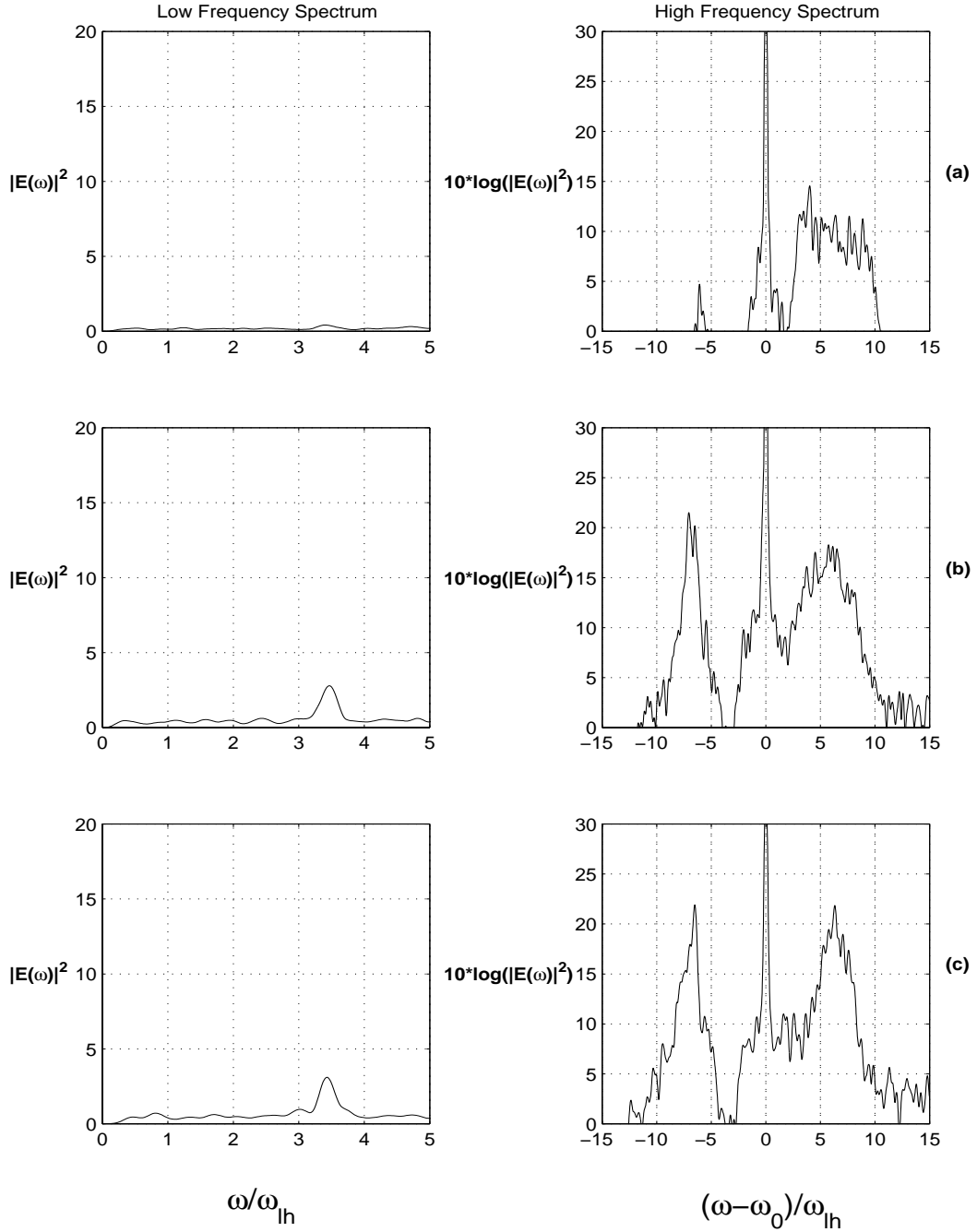


Figure 4.16: Simulation electric field power spectra showing time evolution of the broad up-shifted and broad down-shifted spectral features at different time instants for the cases (a) $0 < \omega_{lh}t < 300$ (b) $300 \leq \omega_{lh}t < 600$ (c) $600 \leq \omega_{lh}t < 900$.

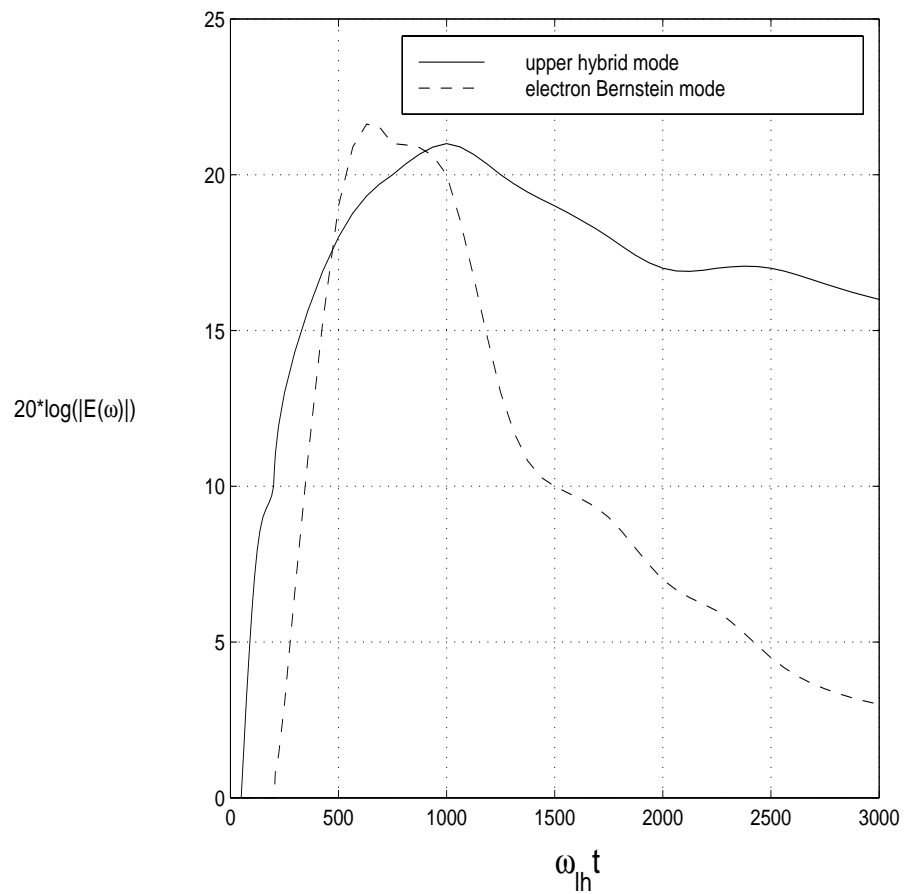


Figure 4.17: A result showing the time evolution of the peak amplitude of both the upper hybrid and electron Bernstein modes.

Chapter 5

Summary and Conclusions

In this work, parametric instability processes thought to be responsible for SEE sideband spectral features are discussed and analyzed using theoretical and electrostatic PIC simulation models. The decay instabilities considered include lower hybrid decay LHDI, ion cyclotron decay ICDI and the four-wave decay process proposed by *Huang and Kuo* [1994]. These decay instabilities have been proposed to produce the DM, DP and BUM spectral features respectively. The results we presented are very encouraging for having the potential of complementing the experimental observations and the theoretical analysis.

Theoretical predictions and numerical simulations were used to study the three-wave decay instability process thought to be responsible for the generation of the down-shifted sidebands, especially the lower hybrid decay instability LHDI and the ion cyclotron decay instability ICDI. The theoretical predictions were very successful for providing the angular regime, with respect with the direction perpendicular to the magnetic field, at which the sidebands develop as well as the frequency and wavenumber regimes of both the ICDI and the LHDI. It was also found that the ICDI was very sensitive to the temperature ratio T_e/T_i and the LHDI was essentially temperature independent. Looking at the simulation electric field power spectrum, it was found that the theory was very accurate in predicting the presence of the LHDI and ICDI at the appropriate regimes. It was also noted that, for the ICDI, as T_e/T_i was increased the down-shifted sideband becomes narrower in frequency as well as the sideband gets closer to the heater frequency, as predicted by the theory. Time evolution of both the LHDI and the ICDI was also investigated. It was noted that for both instabilities, the simulation electric field power spectrum did not vary much if we take the spectrum in the linear growth rate regime or after the electric field energy has reached a steady state. The theoretical predictions were also used to investigate the cascading of the LHDI and the ICDI. Particle heating and density irregularities were also observed to be associated with the three-wave instability in our simulations.

A four-wave parametric decay instability process thought to be responsible for SEE broad up-shifted sideband spectral features was also discussed using theoretical and numerical simulation models. Many theoretical results were presented, in which the heater frequency ω_0 was stepped closer to the upper hybrid resonance frequency ω_{uh} and the growth rate of the four-wave decay process was calculated. It was found that as ω_0 is stepped closer to ω_{uh} , the angle of maximum growth rate θ_{max} decreases, at the same time the growth rate at this angle γ_{max} increases. It was also noted that as the heater frequency is moved closer to ω_{uh} , the four-wave process shifts to a higher frequency and to a shorter wavelength. The growth rate results were also useful in guiding the simulation results by providing us with the parameters for the four-wave process responsible for the up-shifted sidebands. We found good agreement between the predictions of the theoretical model and numerical simulations. The simulation electric field power spectrum showed a large amplitude up-shifted sideband and a much smaller amplitude down-shifted sideband, consistent with the experimental observations. The simulation electric field power spectrum was taken in the time interval where the electric field energy has reached steady state. It was found that if the electric field power spectrum was taken in the regime where the waves are still growing and have not reached a steady state, the up-shifted and down-shifted sidebands would start growing together with almost the same growth rate and same relative amplitude. This result may be observed in actual experiments as time evolves. The development of density irregularities, cavities and particle heating were also observed to be associated with the four-wave instability in our simulations.

The results we presented are very encouraging for having the potential of complementing the experimental observations since it gave a detailed study of all the nonlinear processes that take place during the three-wave and the four-wave decay processes thought to be responsible for the down-shifted and up-shifted sidebands, respectively. These details may help to fully understand the physical mechanisms responsible for generation of these sidebands during ionospheric heating experiments. The theoretical predictions were also very useful in providing the angular regime with respect to the geomagnetic field at which these instabilities develop. The fact that these instabilities develop at a particular angular regime can be very useful for experimental observations. The effect of the temperature ratio T_e/T_i on the down-shifted sidebands is also an important result that may be observed during ionospheric heating experiments.

5.1 Future work

In this work, initial study of the relevant three-wave parametric decay instabilities with a one dimensional model was conducted. The model used has some advantage

since it only considers one angle of propagation with respect to the magnetic field. In this case, the two primary three-wave decay instabilities, the LHDI and the ICDI could be investigated independently since they are excited in different angle regimes, Figure (3.2). In reality, these two instabilities are expected to exist simultaneously when a spectrum of propagation angles with respect to the magnetic field is allowed. Nonlinear interactions between these two processes may produce important effects on the wave spectra in two dimensions. Future work may utilize a two-dimensional PIC model for this study. Detailed analysis of the nonlinear evolution of the two processes may be investigated in two-dimension as well as the relevance of nonlinear of nonlinear interactions on the spectrum of waves. Also, important effects of the proximity of ω_0 and ω_{uh} to the cyclotron harmonics may be investigated more thoroughly.

We have presented in this study preliminary results of the first attempt at numerically simulating the four-wave process thought to be responsible for the generation of the BUM spectral feature. Future work might involve further investigation of this process from a basic plasma stand point. Parametric studies of the four-wave decay equations may be performed to determine important parametric dependencies on T_e/T_i and the pump amplitude. A two dimensional model might also be utilized in this study as well.

In this study, we considered the case where $\omega_{uh} > n\Omega_{ce}$. Future work might consider studying the processes for the case where $\omega_{uh} < n\Omega_{ce}$. It may also consider the effect of other electron cyclotron harmonics.

The continuum is another prominent feature in the SEE spectrum. It was shown by *Mjølhus et al.* [1995] that Langmuir caviton collapse near the reflection height ($\omega_0 \simeq \omega_{pe}$). Recent observations of the continuum feature have shown that it exhibits important cyclotron harmonic effects [*Leyser et al.*, 1993; *Stubbe et al.* 1994]. The model of *Mjølhus et al.* [1995] did not include magnetic field and kinetic effects and therefore could not consider the production of the continuum feature near the upper hybrid resonance and cyclotron harmonics. Future work might provide an extension of the work of *Mjølhus et al.* [1995] in order to gain insight into the cyclotron harmonic effects on the continuum feature. The numerical model used in our study is well suited for such investigation. *Mjølhus et al.* [1995] have shown that the key parameter distinguishing the cavitating Langmuir turbulence from cascading turbulence is $\Delta\Omega(z) = \omega_0 - \omega_{pe}(z)$. when this parameter is small, a broad frequency spectrum is excited with many characteristics of the continuum. When $\Delta\Omega$ is larger, indicating that the pump frequency is larger than the local plasma frequency, a cascading spectrum exists. This corresponds to the regime of our investigation in this study for parametric decay instabilities when $\omega_0 > \omega_{uh}$. Future work might extend these concepts to the upper hybrid resonance layer where the role of the plasma frequency ω_0 may be replaced with the upper hybrid resonance frequency ω_{uh} . The effects of the proximity of ω_0 to the cyclotron harmonics might be investigated in detail.

Appendix A

Numerical calculations of the susceptibilities and solution of dispersion relations

A.1

In this appendix, it is required to express the susceptibilities χ_i and χ_e in unitless variables that are used by *Rönmark* [1982]. The susceptibilities can then be used to obtain expressions for the dispersion relations for either the three-wave interaction process [equation (3.1)] or the four-wave interaction process [equation (4.1)]. These dispersion relations are solved numerically using Newton's method to obtain the growth rate for the three-wave and four-wave processes using the FORTRAN code `THREEWAVE.f` and `FOURWAVE` subroutine respectively [appendix B,E]. Note that the derivatives of the susceptibilities are also needed to solve the dispersion relations for both the three-wave and four-wave processes since Newton's method requires the derivatives. Note that the susceptibilities for the ions are obtained assuming that the ions are unmagnetized in this case.

Starting with the susceptibilities for the ions [*Porkolab, 1974*] given by

$$\chi_i = \frac{1}{k^2 \lambda_{di}^2} \left\{ 1 + \zeta_{i0} \sum_{n=-\infty}^{\infty} \Lambda_n(b_i) Z(\zeta_{in}) \right\} \quad (\text{A.1})$$

where Z is the plasma dispersion function or the Fried Conte function, $b_i = (k_{\perp}^2 \rho_i^2)/2$, $\zeta_{in} = (\omega - n\Omega_i)/(k_{\parallel} v_{ti})$, $\zeta_{i0} = (\omega)/(k_{\parallel} v_{ti})$, $v_{te} = \sqrt{(2T_e)/(m_e)}$ and $v_{ti} = \sqrt{(2T_i)/(m_i)}$.

Thus, $v_{ti}/v_{te} = \sqrt{m_e T_i / m_i T_e}$. This yields to $b_i = (k_{\perp}^2 \rho_e^2) / 2(m_i T_i) / (m_e T_e)$. Substituting with all the previous in (A.1) yields

$$\chi_i = (k_{di}/k)^2 \left\{ 1 + \frac{\omega}{\Omega_e} \frac{\Omega_e}{v_{ti} k_{\parallel}} \sum_{n=-\infty}^{\infty} \Lambda_n \left(\frac{k_{\perp}^2 \rho_i^2}{2} \right) Z \left(\frac{(\omega/\Omega_e) - n(\Omega_i/\Omega_e)}{k_{\parallel}(v_{ti}/\Omega_e)} \right) \right\} \quad (\text{A.2})$$

Now, let us define the variables $\bar{\omega} = \omega/\Omega_e$, $\bar{\omega}_{pe} = \omega_{pe}/\Omega_e$. Note also that $\lambda = k^2 \rho_e^2 = k^2 (v_{te}^2 / \Omega_e^2)$. Substituting in (A.2) gives

$$\chi_i = (k_{di}/k)^2 \left\{ 1 + \frac{\bar{\omega}}{\rho_e k_{\parallel} \sqrt{m_e T_i / m_i T_e}} \sum_{n=-\infty}^{\infty} \Lambda_n \left(\frac{k_{\perp}^2 \rho_i^2}{2} (m_i T_i) / (m_e T_e) \right) Z \left(\frac{\bar{\omega} - n(m_e/m_i)}{k_{\parallel} \rho_e (m_e T_i) / (m_i T_e)} \right) \right\} \quad (\text{A.3})$$

from appendix A.2 we have

$$\sum_{n=-\infty}^{\infty} \Lambda_n(b_i) Z(\zeta_i n) = \sum_{m=1}^8 \frac{r_m k_{\parallel} \rho_i b_i}{Y^2} [R(Y, b_i) + Y/b_i] \quad (\text{A.4})$$

where the form of the function R of *Rönmark* [1982] is given by

$$R(\bar{\omega}, \lambda) = \sum_{n=-\infty}^{\infty} \frac{n^2 \lambda_n(\lambda)}{\lambda \bar{\omega} - n} \quad (\text{A.5})$$

In our case, $Y = \bar{\omega}(m_i/m_e) - C_m k_{\parallel} \rho_e \sqrt{(m_i T_i) / (m_e T_e)}$, where C_m 's are the poles of the Padé approximant. The subroutine RYLA in *Rönmark's* WHAMP code solves this function numerically for all $\bar{\omega}, \lambda$ space. Substituting with these results into (A.3) yields

$$\chi_i = \left(\frac{k_{di}}{k} \right)^2 \left\{ 1 + \frac{\bar{\omega}}{\rho_e k_{\parallel}} (m_i/m_e) \sum_{m=1}^8 r_m k_{\parallel} \rho_e (b_i/Y^2) (R(Y, b_i) + Y/b_i) \right\} \quad (\text{A.6})$$

note that $(k_{di}/k)^2 = (1/(\lambda_{di} k))^2 = (\sqrt{2} \omega_{pi} / (v_{ti} k))^2 = 2 \left((\omega_{pe} / \Omega_e) / (k v_{te} \sqrt{T_i / T_e}) \right)^2 = 2 \left(1/k (\bar{\omega}_{pe} / \rho_e) \sqrt{T_e / T_i} \right)^2 = 2 (T_e / T_i) (\bar{\omega}_{pe} / (\rho_e k))^2$. Substituting with the above expressions into (A.4) we get the final expression for the ions susceptibility.

$$\chi_i = 2\left(\frac{T_e}{T_i}\right)\left(\frac{\bar{\omega}_{pe}}{\rho_e k}\right)^2 \left\{ 1 + \frac{\bar{\omega}}{\rho_e k_{\parallel}} (m_i/m_e) \sum_{m=1}^8 r_m k_{\parallel} \rho_e (b_i/Y^2) (R(Y, b_i) + Y/b_i) \right\} \quad (\text{A.7})$$

An expression for the electrons susceptibility can be obtained in the same manner. As we mentioned earlier, these expressions for the susceptibilities are used to obtain the dispersion relation for both the three-wave and four wave interaction processes. These dispersion relations are solved numerically by using `THREEWAVE.f` fortran code and `FOURWAVE` subroutine, using Newton's method. As we mentioned earlier, the derivatives of the susceptibilities are also needed to solve the dispersion relations of both the three-wave and four-wave interaction processes. The expressions for the derivatives of the susceptibilities with respect to $\bar{\omega}$ are found easily from (A.7) and using the method of *Rönnmark* in the WHAMP code to find an expression for the derivative of the function R of *Rönnmark* [1982] with respect to $\bar{\omega}$.

A.2

In this appendix it is required to show that

$$\sum_{n=-\infty}^{\infty} \Lambda_n \left(\frac{k_{\perp}^2 \rho_e^2 m_i}{2 m_e} \right) Z \left(\frac{\bar{\omega} - n(m_e/m_i)}{k_{\parallel} \rho_e \sqrt{m_e/m_i}} \right) = \sum_{m=1}^8 \frac{r_m k_{\parallel} \rho_e \sqrt{m_i/m_e} b_i}{Y^2} (R(Y, b_i) + Y/b_i) \quad (\text{A.8})$$

Let $b_i = (m_i/m_e)(k_{\perp}^2 \rho_e^2)/2$. Note also that $Z(z) = \sum_{m=1}^8 r_m/(z - c_m)$, where r_m and c_m are the residues and poles of the padé approximant, respectively. Substituting in the left hand side of (A.8) we get

$$\begin{aligned} & \sum_{n=-\infty}^{\infty} \Lambda_n \left(\frac{k_{\perp}^2 \rho_e^2 m_i}{2 m_e} \right) Z \left(\frac{\bar{\omega} - n(m_e/m_i)}{k_{\parallel} \rho_e \sqrt{m_e/m_i}} \right) \\ &= \sum_{n=-\infty}^{\infty} \Lambda_n(b_i) \sum_{m=1}^8 \frac{r_m}{(\bar{\omega} - n(m_e/m_i))/(k_{\parallel} \rho_e \sqrt{m_e/m_i}) - c_m} \\ &= \sum_{n=-\infty}^{\infty} \Lambda_n(b_i) \sum_{m=1}^8 \frac{r_m k_{\parallel} \rho_e \sqrt{m_e/m_i}}{\bar{\omega} - n(m_e/m_i) - c_m k_{\parallel} \rho_e \sqrt{m_e/m_i}} \end{aligned} \quad (\text{A.9})$$

$$\begin{aligned}
&= \sum_{m=1}^8 r_m k_{\parallel} \rho_e \sqrt{m_e/m_i} \sum_{n=-\infty}^{\infty} \frac{\Lambda_n(b_i)}{\bar{\omega} - n(m_e/m_i) - c_m k_{\parallel} \rho_e \sqrt{m_e/m_i}} \\
&= \sum_{m=1}^8 r_m k_{\parallel} \rho_e \sqrt{m_e/m_i} \sum_{n=-\infty}^{\infty} \frac{\Lambda_n(b_i)(m_i/m_e)}{\bar{\omega}(m_i/m_e) - n - c_m k_{\parallel} \rho_e \sqrt{m_i/m_e}} \\
&= \sum_{m=1}^8 r_m k_{\parallel} \rho_e \sqrt{m_i/m_e} \sum_{n=-\infty}^{\infty} \frac{\Lambda_n(b_i)}{\bar{\omega}(m_i/m_e) - n - c_m k_{\parallel} \rho_e \sqrt{m_i/m_e}}
\end{aligned}$$

Let $Y = \bar{\omega}(m_i/m_e) - c_m k_{\parallel} \rho_e \sqrt{m_i/m_e}$, from appendix A.3, $\sum_{n=-\infty}^{\infty} \Lambda_n(b_i)/(Y - n) = 1/Y^2 \sum_{n=-\infty}^{\infty} (n^2 \Lambda_n(b_i))/(Y - n) + 1/Y$ thus,

$$\begin{aligned}
\sum_{n=-\infty}^{\infty} \Lambda_n\left(\frac{k_{\perp}^2 \rho_e^2 m_i}{2 m_e}\right) Z\left(\frac{\bar{\omega} - n(m_e/m_i)}{k_{\parallel} \rho_e \sqrt{m_e/m_i}}\right) &= \sum_{m=1}^8 r_m k_{\parallel} \rho_e \sqrt{m_i/m_e} \left(1/Y^2 \sum_{n=-\infty}^{\infty} \frac{n^2 \Lambda_n(b_i)}{Y - n} + 1/Y\right) \\
&= \sum_{m=1}^8 r_m k_{\parallel} \rho_e \sqrt{m_i/m_e} \left(b_i/Y^2 \sum_{n=-\infty}^{\infty} 1/b_i \frac{n^2 \Lambda_n(b_i)}{Y - n} + 1/Y\right) \\
&= \sum_{m=1}^8 \frac{r_m k_{\parallel} \rho_e \sqrt{m_i/m_e} b_i}{Y^2} \left(\sum_{n=-\infty}^{\infty} 1/b_i \frac{n^2 \Lambda_n(b_i)}{Y - n} + Y/b_i\right) \\
&= \sum_{m=1}^8 \frac{r_m k_{\parallel} \rho_e \sqrt{m_i/m_e} b_i}{Y^2} (R(Y, b_i) + Y/b_i)
\end{aligned}$$

Finally we prove that

$$\sum_{n=-\infty}^{\infty} \Lambda_n\left(\frac{k_{\perp}^2 \rho_e^2 m_i}{2 m_e}\right) Z\left(\frac{\bar{\omega} - n(m_e/m_i)}{k_{\parallel} \rho_e \sqrt{m_e/m_i}}\right) = \sum_{m=1}^8 \frac{r_m k_{\parallel} \rho_e \sqrt{m_i/m_e} b_i}{Y^2} (R(Y, b_i) + Y/b_i) \tag{A.10}$$

A.3

In this appendix it is required to show that

$$\sum_{n=-\infty}^{\infty} \frac{n\Lambda_n}{Y-n} = 1/Y \sum_{n=-\infty}^{\infty} \frac{n^2\Lambda_n}{Y-n}$$

note that

$$\sum_{n=-\infty}^{\infty} \frac{n\Lambda_n}{Y-n} + 1 = \sum_{n=-\infty}^{\infty} \left(\frac{n\Lambda_n}{Y-n} + \Lambda_n \right) \quad (\text{since } \sum_{n=-\infty}^{\infty} \Lambda_n = 1) \quad (\text{A.11})$$

so,

$$\sum_{n=-\infty}^{\infty} \frac{n\Lambda_n}{Y-n} + 1 = \sum_{n=-\infty}^{\infty} \left(\frac{n\Lambda_n}{Y-n} + \Lambda_n \frac{Y-n}{Y-n} \right) \quad (\text{A.12})$$

therefore,

$$\sum_{n=-\infty}^{\infty} \frac{n\Lambda_n}{Y-n} = Y \sum_{n=-\infty}^{\infty} \frac{n\Lambda_n}{Y-n} - 1 \quad (\text{A.13})$$

also,

$$\sum_{n=-\infty}^{\infty} \frac{n^2\Lambda_n}{Y-n} = - \sum_{n=-\infty}^{\infty} \left(\frac{(Y^2 - n^2)\Lambda_n}{Y-n} - Y^2 \frac{\Lambda_n}{Y-n} \right) \quad (\text{A.14})$$

$$= - \sum_{n=-\infty}^{\infty} \left[(Y+n)\Lambda_n - Y^2 \frac{\Lambda_n}{Y-n} \right]$$

$$= -Y + Y^2 \sum_{n=-\infty}^{\infty} \frac{\Lambda_n}{Y-n}$$

(since $\sum_{n=-\infty}^{\infty} n\Lambda_n = 0$, $\Lambda_n = \Lambda_{-n}$)

thus,

$$Y \sum_{n=-\infty}^{\infty} \frac{\Lambda_n}{Y-n} = \frac{1}{Y} \sum_{n=-\infty}^{\infty} \frac{n^2\Lambda_n}{Y-n} + 1 \quad (\text{A.15})$$

Substituting from (A.13) into (A.15) we get

$$\sum_{n=-\infty}^{\infty} \frac{n\Lambda_n}{Y-n} = 1/Y \sum_{n=-\infty}^{\infty} \frac{n^2\Lambda_n}{Y-n} \quad (\text{A.16})$$


```

    if(i.le.range) then

    do 11 j=1,maxit

    if(j.le.nbisect) then
    dwo=dw
    dw=0.5d0*(wh-wl)
    w = wl + dw
    else
    dwo=dw
    dw = f/df
    w = w - dw
    endif

    ws=w
    dws=dw

    if(aimag(ws).gt.dimag(w2)) then
    goto 1000
    endif

    if(cabs(dws).lt.1.e-6*cabs(ws)) go to 3
    call disp(w,kp2,kz,f,df)

    if(dreal(f).lt.0.0) then
    wl=w
    else
    wh=w
    endif

11  continue

    endif

c%%%%%%%%%%%%%%%%%%%%%%%%%%%%%%%%%%%%%%%%%%%%%%%%%%%%%%%%%%%%%%%%%%%%%%%%%

    if(i.gt.range) then

    do 511 j=1,maxit

    dwo=dw
    dw = f/df
    w = w - dw

    ws=w
    dws=dw

```


cccccccccccccccccccc The summation is done here for Xie and dXie ccccccc

$$\text{zetai} = (w + \text{jjj} * \text{etai}) * \text{sqrt}(\text{mime} * \text{TeTi}) / \text{km}$$

$$\text{zetai1} = \text{sqrt}(\text{mime} * \text{TeTi}) / \text{km}$$

$$\text{colis} = \text{jjj} * \text{etai} * \text{sqrt}(\text{mime} * \text{TeTi}) / \text{km}$$

DO 1 I=1,8

cc ELECTRONS ccccccccccccccccccc

$$Y(I) = w + \text{jjj} * \text{etae} - (C(I) * \text{kz})$$

$$v(I) = B(I) * \text{kz} * \text{bi} / Y(I) ** 2$$

$$Yi = Y(I)$$

call ryla(Yi,bi,rc)

$$\text{SUM} = v(I) * (rc(1,1) + (Y(I) / \text{bi}))$$

$$Zm = \text{SUM} + Zm$$

$$\text{SUM2} = v(I) * ((rc(2,1) / Y(I) + 1 / \text{bi}) - 2 * (rc(1,1) / Y(I) + (1 / \text{bi})))$$

$$\text{Zder} = \text{SUM2} + Zder$$

cc IONS ccccccccccccccccccccccc

$$\text{SUMi} = B(I) / (\text{zetai} - C(I))$$

$$Zmi = \text{SUMi} + Zmi$$

$$\text{SUMi2} = -B(I) * \text{zetai1} / (\text{zetai} - C(I)) ** 2$$

$$\text{Zderi} = \text{SUMi2} + Zderi$$

cc

1 CONTINUE

cc

$$A1 = 1 + \text{zetai} * Zmi$$


```

      SUBROUTINE RASY(Y,AL,RC)
C
C USE ASYMPTOTIC SERIES FOR SUFFICIENTLY LARGE KRHO
C
CCCCCCCCCCCCCCCCCCCCCCCCCCCCCCCCCCCCCCCCCCCCCCCCCCCCCCCCCCCCCCCC
C
      COMPLEX*16 Y,Y2,COT,P,PY,PP,PPY,PN,PYN,QN,QYN,RC(2,2)

      PI=3.14159265358979
      Y2=Y*Y
      COT=COS(PI*Y)/SIN(PI*Y)
*           1.E99 IS TOO BIG FOR S/370 HARDWARE. SET TO LARGEST
*           POSSIBLE FOR IBM MACHINES
*
      C=1.E99
      C = 7.2E35
      PN=-Y/AL
      PYN=PN
      A=1./(AL*SQRT(2.*PI*AL))
      QN=PI*Y2*COT*A
      QYN=QN*(2.-Y*PI*COT)-Y*PI**2*Y2*A
C
      P=PN+QN
      PY=PYN+QYN
      PP=-PN-1.5*QN
      PPY=-PYN-1.5*QYN
      AY=CDABS(Y)+2.
C
      DO 4 N=1,100
      M=N-1
      PYN=(PYN*(M*M-Y2)-2.*Y2*PN)/((2*M+1)*AL)
      PN =PN*(M*M-Y2)/((2*M+1)*AL)
      QYN=(QYN*((M+.5)**2-Y2)-2.*Y2*QN)/(2.*N*AL)
      QN =QN*((M+.5)**2-Y2)/(2.*N*AL)
      IF(M.LT.AY) GOTO 3
      C=N*(CDABS(PN)+CDABS(QN))
      IF(C.LE.1.E-7*ABS(PP)) GOTO 5
      IF(C.GE.T) GOTO 5
3  P  =P  + PN  + QN
   PY =PY + PYN + QYN
   PP =PP -(N + 1.)*PN -(N + 1.5)*QN
   PPY=PPY-(N + 1.)*PYN-(N + 1.5)*QYN
4  T=C
C
5  RC(1,1)=P + PN + QN
   RC(2,1)=PY+ PYN+ QYN
   RC(1,2)=PP+P
   RC(2,2)=PPY+PY
      RETURN
      END
C

```

```

CCCCCCCCCCCCCCCCCCCCCCCCCCCCCCCCCCCCCCCCCCCCCCCCCCCCCCCCCCCCCCCC
C
      SUBROUTINE RINT(YY,AL,RC)
C
C USE NUMERICAL INTEGRATION FOR KRHO ON THE ORDER OF 1
C
CCCCCCCCCCCCCCCCCCCCCCCCCCCCCCCCCCCCCCCCCCCCCCCCCCCCCCCCCCCCCCCC
C
      COMPLEX*16 RC(2,2),Y,YY,COT,D,EXF,F,H,O,P,R,RY,RP,RPY,S
      REAL*8 A(16), W(16)
C      ABSCISSAS FOR GAUSSIAN INTEGRATION
      DATA A/
D -.865631202387831d0, -.755404408355003d0, -.617876244402643d0,
D -.458016777657227d0, -.281603550779258d0, -.095012509837637d0,
D
D .989400934991649d0, .944575023073232d0,
D .865631202387831d0, .755404408355003d0, .617876244402643d0,
D .458016777657227d0, .281603550779258d0, .095012509837637d0/,
D W /
D .027152459411754d0, .062253523938647d0,
D .095158511682492d0, .124628971255533d0, .149595988816576d0,
D .169156519395002d0, .182603415044923d0, .189450610455068d0,
D
D .027152459411754d0, .062253523938647d0,
D .095158511682492d0, .124628971255533d0, .149595988816576d0,
D .169156519395002d0, .182603415044923d0, .189450610455068d0/,
D PI/3.14159265358979d0/
C
      CALL ZEROC2( RC, 1, 2, 1, 2 )
      IF(REAL(YY).LT.0.) THEN
          Y=-YY
          SIG=-1.
      ELSE
          Y=YY
          SIG=1.
      END IF
      YA=DIMAG(Y)
      YR=REAL(Y)
      UL=PI-2.8*Y/(36.+Y)
      COT=COS(PI*Y)/SIN(PI*Y)
      D=PI*(1.+COT**2)
      C=YR/AL
      XO=LOG(C+SQRT(1.+C**2))
C
      DO 10 I=1,16
      X=UL/2.*(1.+A(I))
      Z=SIN(X)
      C=COS(X)
      G=YR/AL*X/Z
      T=SQRT(1.+G**2)
      B=LOG(G+T)
      G=(1./X-C/Z)*G/T
      T=AL*(T*C-1.)

```

```

Z=EXP(X*YA)
C=.5*(Z+1./Z)
S=(0.,.5)*(Z-1./Z)
F=COT+G
H=1.-G*COT
EXF=EXP(T-Y*B)
O=B*C+X*S
P=X*C-B*S
XY=X*YR
R=(F*C+H*S)*EXF
RY=(F*O-H*P+D*(C-G*S))*EXF
RP=((F*T-H*XY)*C+(H*T+F*XY)*S)*EXF
RPY=(F*(T*O-XY*P)-H*(T*P+XY*O)+((T+XY*G)*C-(G*T-XY)*S)*D)*EXF
C
X=XO/2.*(1.+A(I))
Z=EXP(X)
C=(Z+1./Z)/2.-1.
P=EXP(AL*C-Y*X)
RC(1,1)=RC(1,1)+W(I)*(UL*R+XO*P)
RC(2,1)=RC(2,1)-W(I)*(UL*RY+XO*X*P)
RC(1,2)=RC(1,2)+W(I)*(UL*RP+XO*AL*C*P)
RC(2,2)=RC(2,2)-W(I)*(UL*RPY+XO*AL*X*C*P)
10 CONTINUE
C
O=Y/AL
P=Y**2/2.
RC(1,1)=O*(Y*RC(1,1)/2.-1.)*SIG
RC(2,1)=2.*RC(1,1)+O*(P*RC(2,1)+1.)*SIG
RC(1,2)=Y*O*RC(1,2)/2.*SIG
RC(2,2)=2.*RC(1,2)+O*P*RC(2,2)*SIG
END
C
CCCCCCCCCCCCCCCCCCCCCCCCCCCCCCCCCCCCCCCCCCCCCCCCCCCCCCCCCCCCCCCC
C
SUBROUTINE RTAY(Y,AL,RC)
C
C USE TAYLOR SERIES FOR SUFFICIENTLY SMALL KRHO
C
CCCCCCCCCCCCCCCCCCCCCCCCCCCCCCCCCCCCCCCCCCCCCCCCCCCCCCCCCCCCCCCC
C
COMPLEX*16 Y,Y2,RC(2,2),PN,PYN,COT

Y2=Y*Y
10 PN=Y/(Y2-1.)
PYN=-Y*(Y2+1.)/(Y2-1. )**2
RC(1,1)=PN
RC(1,2)=PN
RC(2,1)=PYN
RC(2,2)=PYN
C

```


Appendix C

A description of the 1D numerical electrostatic simulation model

C.1 Simulation model

In this section, we briefly discuss the Particle-In-Cell (PIC) electrostatic plasma simulation model used in this study [Birdsall and Langdon 1991]. A one-dimensional PIC simulation model was used in our study. We will consider discussing the model briefly. Note that the PIC simulation model was used in this study since it includes kinetic modes such as Bernstein modes which are thought to play an important role in producing SEE. It also allows for detailed study of nonlinear evolution. The one-dimensional model assumes one spatial dimension (x) and three velocities (v_x , v_y and v_z). The whole plasma length (l) is equally divided into a number of grid cells (ng) which is required to be an integer power of two since FFT techniques are used. Thus, there are $ng+1$ grid points. We generally use the index i to denote particles and the index j to denote grid cells or grid points. Figure C.1 gives a view how the 1-D geometry is divided. The parameter dx is the grid spacing and is equal to l/ng .

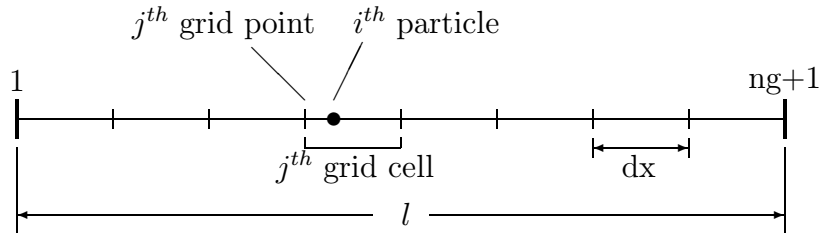


Figure C.1: Discretization of the plasma length and naming of grids and particles.

The algorithm we used is straightforward. The computational cycle is shown in

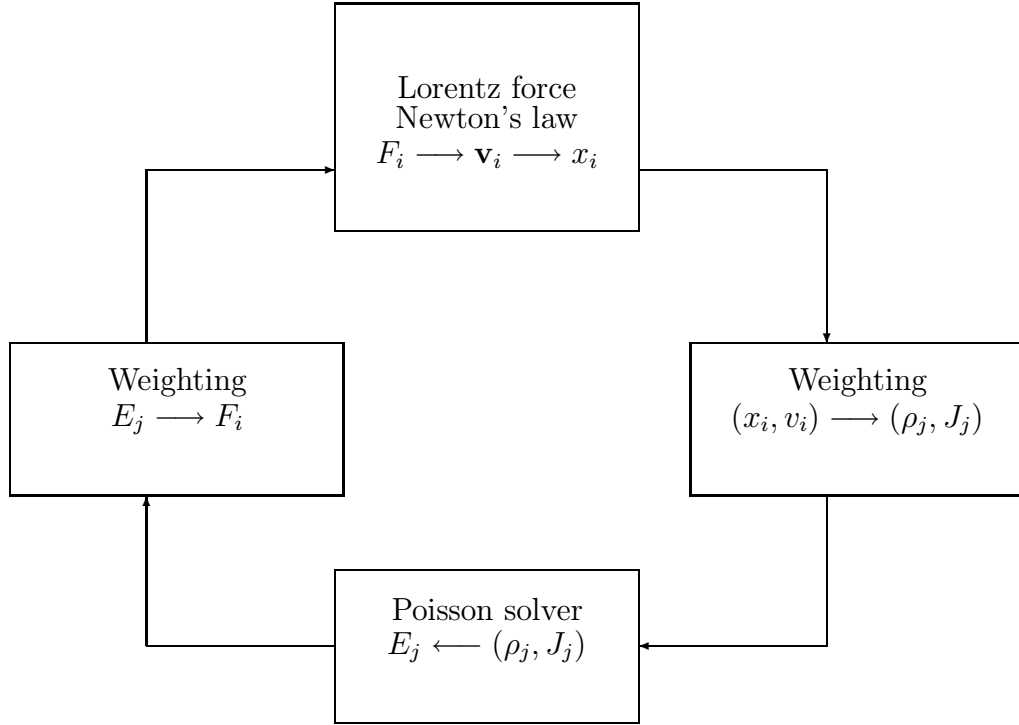


Figure C.2: A typical computational cycle for the particle simulation model.

Figure C.2. The three equations that are used in the computational loop are

Newton's second law

$$\mathbf{F} = m \frac{d\mathbf{v}}{dt} \quad \mathbf{v} = \frac{d\mathbf{x}}{dt} \quad (\text{C.1})$$

The Lorentz force equation

$$\mathbf{F} = q(\mathbf{E} + \mathbf{v} \times \mathbf{B}) \quad (\text{C.2})$$

and Poisson's equation

$$\nabla^2 \phi = -\frac{\rho}{\epsilon_0} \quad (\text{C.3})$$

Note that for the one-dimensional simulation model the only dimension is the x-direction. However, the velocities other than x-direction certainly have contribution

to the force acting on particles through the Lorentz force equation. Therefore, we have to keep more than one velocity when the background magnetic field is nonzero. The first two equations are solved numerically using the center difference method, while the Poisson's equation is solved by Fast Fourier Transform (FFT). Note that for the four-wave decay instability we have doubled the number of particles in the simulation box, since this instability requires the simulation to run for a long number of time steps, which increases the fluctuation level in the system, for the instability to develop. Increasing the number of particles in the system would have an effect when averaging over the particles in each grid cell, which will cause a decrease in the fluctuation level in this case.

C.2 Approximations

C.2.1 The use of an artificial mass ratio in our simulations

In our 1-D electrostatic Particle In Cell simulation code an artificial electrons to ions mass ratio m_e/m_i was used. The main reason for that is to allow the simulations to run at a reasonable amount of CPU time. Since a small mass ratio favors a faster growth rate of the parametric instability. At the same time, this will allow for a meaningful frequency separation between the plasma frequencies ω_{pe}, ω_{pi} , the cyclotron frequencies Ω_{ce}, Ω_{ci} as well as a wide frequency separation between the pump frequency and the sidebands. This will also allow for the existence of the usual low frequency and high frequency plasma frequency wave modes.

C.2.2 The effect of electron-neutral collisions in the simulation of Stimulated Electromagnetic Emission SEE

In our simulation model no collisions between the electrons and neutrals were considered. There are two effects upon including collisions in our simulation model. The first is the electric field threshold. Since having collisions between the electrons and the neutrals will cause some energy to be dissipated due to this collision and thus a larger electric field amplitude (threshold) will be required to drive the development of the parametric instability responsible for the SEE. Note also that having a collisional system will cause the growth rate of the instability to decrease and thus increases the amount of CPU time required for the instability to develop. So, since no collision effects were included in our simulations this will have the effect of having a threshold field of zero. So, any applied electric field amplitude will cause the instability to take place, neglecting numerical limitations. The second effect that collisions may

add to the simulations is thermal nonlinearity due to the collisions between the two species. This effect has been discussed by *Huang and Kuo*, [1994]; *Dysthe et al.*, [1983]; *Lee and Kuo* [1983]. The effect of thermal nonlinearity is due to the thermal forces taking place due to the velocity dependence on the collision frequency between the electrons and the neutrals γ_{en} . The thermal nonlinearity was discussed by *Huang and Kuo*, [1994] and *Dysthe et al.*, [1983] when discussing the oscillating two stream instability OTSI. They have suggested that the heater excited field aligned density irregularities in the high latitude ionosphere are excited through thermal instability. Therefore, a thermal oscillating two stream instability OTSI leading to parametric excitation of electron Bernstein/upper hybrid waves together with purely growing density irregularities by the HF heater wave was their suggested mechanism for the process.

Appendix D

TRANSFORM.m program listing

This program written in MATLAB calculates the FFT of the time sequence obtained from the ES1 simulation program and centers the pump frequency around zero frequency. The listing for TRANSFORM.m follows:

```
%%*****%%
%%          This version has the length of the sequence specified by the %%
%%          user, both the initial and final points of the sequence. %%
%%          This volume has also the advantage of giving the file %%
%%          name as an entry in our program %%
%%          a second harmonic feature is added %%
%%          Also, a log scale option is added %%
%%*****%%

clear;
for l=1:2300
v=-10;
for m=1:10
v=v+1;
xI(l,m)=v;
end;
yI(l)=1;
end;

for l=1:80
v=-5;
for m=1:10
v=v+1;
xII(l,m)=v;
end;
yII(l)=1;
end;
```

```

for l=1:40
v=-5;
for m=1:10
v=v+1;
xIII(l,m)=v;
end;
l1=l/40;
yIII(l)=l1;
end;

for l=1:400
v=0;
for m=1:10
v=v+1.0;
xIV(l,m)=v;
end;
yIV(l)=l/10;
end;

*%%%%%%%%%%%% Input the pump frequency and w_lh in here %%%%%%%%%%

fpump=input('please enter the pump frequency: ');
wlh =input('please enter the lower hybrid frequency: ');

counter=1;
N11=1;

input('*****');
input('*           Please input the following parameters           *');
input('*           Press ENTER key after each entry           *');
input('*****');

while ((fpump == 0 ) | (wlh == 0 )) | ((fpump == '' ) | (wlh == '' )),
counter=counter+1;
if(counter >2) input('* Invalid parameter value, please re-enter your
parameters');
end;
fpump=input('* The pump frequency is = ');
wlh =input('* The lower hybrid frequency = ');
end;

input('*****');

input('Which kind of filtering window you want to use.....!!');
input('a. Hanning window (default)');
input('b. Hamming window          ');

```

```

input('c. Triangular window      ');
input('d. Rectangular window     ');
input('e. No filtering            ');
select=input('You choose..... ', 's');
W      =input('The window length = ');

input('*****');

dt = 0.03188;

if select=='a'
fil=hanning(W);
i=1;
end;

if select=='b'
fil=hamming(W);
i=2;
end;

if select=='c'
fil=triang(W);
i=3;
end;

if select=='d'
fil=boxcar(W);
i=4;
end;

if select=='e'
fil=hanning(1);
i=5;
end;

if (select ~='a') & (select ~='b') & (select ~='c') & (select ~='d') & (select
~='e')
fil=hanning(3);
i=6;
end;

*%%%%%%%%%%%% read the input file %%%%%%%%%%%%%%

name=input('Please enter the input file name (no extension): ', 's');
ext =input('Now input the file extension: ', 's');

```

```

input('*****');
data=[name '.' ext];
datak=[name];
eval(['load ' data]);
x=eval(datak);
N=length(x);

*%%%%%%%%%% Specify the sequence length %%%%%%%%%%

for i=1:6

N11=input('The first point in the sequence is: ');
N =input('The end point of the sequence(the default is the vector length) : ');

input('*****');

if N=='
    N=length(x);
end;

if N11=='
    N11=0;
end;

*%%%%%%%%%% DO the FFT and Scaling %%%%%%%%%%

n=1:N-N11;

if (N11 == 0)
ve=x(N11+1:N);
vl=length(ve);
X=fft(ve(1:vl));
end;

if (N11 ~= 0)
ve=x(N11:N);
vl=length(ve);
X= fft(ve(1:vl-1));
end;

N=N-N11;
[maximum,index] = max(X(1:N/2));
X=(abs(X(1:N))).^2;
X1=conv(X,fil);

p=n/N*pi*2;
p1=index*2*pi/N;
scale=p/p1*fpump;

```

```
scale1=(scale-fpump)/wlh;
maximum1=(abs(maximum))^2;
```

```
%%%%%%%%%%%%%%%%%%%%%%%%%%%%%%%%%%%%%%%%%%%%%%%%%%%%%%%%%%%%%%%%%%%%%%%% Plot the High frequency portion %%%%%%%%%%
%%%%%%%%%%%%%%%%%%%%%%%%%%%%%%%%%%%%%%%%%%%%%%%%%%%%%%%%%%%%%%%%%%%%%%%% the first harmonic %%%%%%%%%%
```

```
N1=N;
subplot(2,2,2);
X1=(maximum1/max(X1))*X1;
plot(scale1,X1(1:N)/N1);
%axis([-3 3 0 1.1*max(X1(1:N)/N1)])
axis([-40 40 0 1.5])
```

```
axis('square');
grid;
title('High frequency');
xlabel('(w-wo)/wlh');
ylabel('|E(w)|^2');
```

```
%%%%%%%%%%%%%%%%%%%%%%%%%%%%%%%%%%%%%%%%%%%%%%%%%%%%%%%%%%%%%%%%%%%%%%%% Plot the First harmonic in log scale %%%%%%%%%%
```

```
subplot(2,2,3);
plot(scale1,10*log10(X1(1:N)/N1),xII,yII,':');
axis([-40 40 -40 0])
```

```
axis('square');
grid;
title('HF Log Scale');
xlabel('(w-wo)/wlh');
ylabel('10*log |E(w)|^2');
```

```
%%%%%%%%%%%%%%%%%%%%%%%%%%%%%%%%%%%%%%%%%%%%%%%%%%%%%%%%%%%%%%%%%%%%%%%% Plot the High frequency portion %%%%%%%%%%
%%%%%%%%%%%%%%%%%%%%%%%%%%%%%%%%%%%%%%%%%%%%%%%%%%%%%%%%%%%%%%%%%%%%%%%% the second harmonic %%%%%%%%%%
```

```
scale2=(scale-2*fpump)/wlh;
subplot(2,2,4);
plot(scale2,X1(1:N)/N1,xIII,yIII,':');
axis([-10 10 0 0.3])
axis('square');
grid;
title('Second Harmonic');
xlabel('(w-2wo)/wlh');
ylabel('|E(w)|^2');
```

```
**%%%%%%%%%%%%%%%%%%%%%%%%%%%%%%%%%%%%%%%%%%%%%%%%%%%%%%%%%%%%%%%%%%%%%%%% Plot the low hybrid waves %%%%%%%%%%
```

```
scale3=((scale1*wlh)+fpump)/wlh;
```



```

N2=2*N

do ii=1,N2
TAX(ii)=ii
enddo

do ij=1,N
TAXX(ii)=ij
enddo

do it=1,L
XAX(it)=it
enddo

cccccccccccccccccccc READ THE DATA %%%%%%%%%%%%%%

DO ii=1,LN
  read(18,*) interferog(ii)
ENDDO

do 10 i=1,L
do 10 j=1,N2

if(j.le.N) x(j,i)=0.0

if(j.gt.N) then
x(j,i)=interferog((j-(N+1))*L+i)
endif

10  continue

c dt =0.032

cccccccccccccccccccc Write the Sin Function for XCORR cccccccc

do iii=1,N2

CS(iii)=sin(0.25*(350000+iii)*0.2)

enddo

```

cccccccccccccccccccc Cross Correlation ccccccccccccccccccc

```

do 9999 ix=1,L

      do it=1,N2
            TEMP(it)=x(it,ix)
      ENDDO

do 9999 itau=1,N

      do it1=1,N2-1
            TEMP(it1)=TEMP(it1+1)
      ENDDO

      TEMP(N2)=0.0

      corr(itau)=0.0

      do it2=N+1,N2
            corr(itau)=corr(itau)+CS(it2)*TEMP(it2)
      ENDDO

            interferov(itau,ix)=corr(itau)

9999      continue

c%%%%%%%%%%%%%%%%%%%%%%%%%%%%%%%%%%%%%%%%%%%%%%%%%%%%%%%%%%%%%%%%%%%%%%%% PLOT %%%%%%%%%%%%%%%%%%%%%%%%%%%%%%%%%%%%%%%%%%%%%%%%%%%%%%%%%%%%%%%%%%%%%%%%%
cccccccccccccccccccccccccccccccccccccccccccccccccccccccccccccc
c                                                                 c
c          Plot results with NCAR graphics                        c
c                                                                 c
cccccccccccccccccccccccccccccccccccccccccccccccccccccccccccccc

do 122  ij2=1,L

TEMP2(ij2)=interferov(1,ij2)

```

```

TEMP4(ij2)=interferov(2,ij2)

TEMP5(ij2)=interferov(10,ij2)

TEMP6(ij2)=interferov(50,ij2)

TEMP7(ij2)=interferov(100,ij2)

TEMP8(ij2)=interferov(500,ij2)
122 TEMP9(ij2)=interferov(1000,ij2)

    do 123  ij3=1,N2

123   TEMP3(ij3)=interferov(ij3,3)

        do iv=1,L
        write (20,*)interferov(500,iv)
        enddo

    call OPNGKS

    call agsetf('X/MAXIMUM.', 2000.0)
    call agsetf('X/MINIMUM.', 0.0)
    call agsetf('Y/MAXIMUM.', 3.0)
    call agsetf('Y/MINIMUM.', -3.0)
    call anotat('X$', 'E(x)$', 0,0,0,0)
    call ezxy(TAX,CS,N2-1, 'SINUSOID$')

    call agsetf('X/MAXIMUM.', 2000.0)
    call agsetf('X/MINIMUM.', 0.0)
    call agsetf('Y/MAXIMUM.', 150.0)
    call agsetf('Y/MINIMUM.', -150.0)
    call anotat('T$', 'E(x)$', 0,0,0,0)
    call ezxy(TAX,TEMP3,N2-1, 'X-CORRELATION$')

    call agsetf('X/MAXIMUM.', 1024.0)
    call agsetf('X/MINIMUM.', 0.0)
    call agsetf('Y/MAXIMUM.', 150.0)
    call agsetf('Y/MINIMUM.', -150.0)
    call anotat('X$', '|E(x)|^2$', 0,0,0,0)
    call ezxy(XAX,TEMP4,L-1, 'INTERFEROGRAM 2$')

    call agsetf('X/MAXIMUM.', 1024.0)
    call agsetf('X/MINIMUM.', 0.0)

```

```
call agsetf('Y/MAXIMUM.', 150.0)
call agsetf('Y/MINIMUM.', -150.0)
call anotat('X$', '|E(x)|^2$', 0,0,0,0)
call ezxy(XAX,TEMP5,L-1,'INTERFEROGRAM 10$')

call agsetf('X/MAXIMUM.', 1024.0)
call agsetf('X/MINIMUM.', 0.0)
call agsetf('Y/MAXIMUM.', 150.0)
call agsetf('Y/MINIMUM.', -150.0)
call anotat('X$', '|E(x)|^2$', 0,0,0,0)
call ezxy(XAX,TEMP6,L-1,'INTERFEROGRAM 50$')

call agsetf('X/MAXIMUM.', 1024.0)
call agsetf('X/MINIMUM.', 0.0)
call agsetf('Y/MAXIMUM.', 250.0)
call agsetf('Y/MINIMUM.', -250.0)
call anotat('X$', '|E(x)|^2$', 0,0,0,0)
call ezxy(XAX,TEMP7,L-1,'INTERFEROGRAM 100$')

call agsetf('X/MAXIMUM.', 1024.0)
call agsetf('X/MINIMUM.', 0.0)
call agsetf('Y/MAXIMUM.', 350.0)
call agsetf('Y/MINIMUM.', -350.0)
call anotat('X$', '|E(x)|^2$', 0,0,0,0)
call ezxy(XAX,TEMP8,L-1,'INTERFEROGRAM 500$')

call agsetf('X/MAXIMUM.', 1024.0)
call agsetf('X/MINIMUM.', 0.0)
call agsetf('Y/MAXIMUM.', 450.0)
call agsetf('Y/MINIMUM.', -450.0)
call anotat('X$', '|E(x)|^2$', 0,0,0,0)
call ezxy(XAX,TEMP9,L-1,'INTERFEROGRAM 1000$')

call CLSGKS
stop
end
```

References

- Birdsall, Charles K., and A. Bruce Langdon, *Plasma Physics Via Computer Simulation*, Adam Hilger, New York, 1991.
- Chen, Francis F., *Introduction to Plasma Physics and Controlled Fusion*, Volume 1, Plenum Press, New York, 1984.
- Collin, Robert E., *Antennas and Radio Wave Propagation*, McGraw-Hill, New York, 1985.
- Dythe K.B., E. Mjølhus, H. L. Pecseli, and Rypdal K., A thermal oscillating two-stream instability, *Phys. Fluids*, *26*, 146, 1983.
- Fejer, J. A., and Yu-Yun Kuo, Structure in the nonlinear saturation spectrum of parametric instabilities, *Phys. Fluids*, *16*, 1490, 1973.
- Huang, J. and S. P. Kuo, A generation mechanism for the Downshifted Peak in stimulated electromagnetic emission spectrum, *J. Geophys. Res.*, *100*, 21433, 1995.
- Huang, J. and S.P. Kuo, A theoretical model for the Broad Up-Shifted maximum in stimulated electromagnetic emission spectrum, *J. Geophys. Res.*, *99*, 19569, 1994.
- Hussein, A.A. and W.A. Scales, Simulation Studies of Parametric Decay Instability Processes Associated with Ionospheric Stimulated Radiation, *Radio Science*, in press, 1997.
- Ichimaru S., *Basic principles of plasma physics: a statistical approach*, W. A. Benjamin, Mass., 1973.
- Isham B.C., *Chirped incoherent scatter radar observations of the HF-modified ionosphere*, Dissertation, Cornell University, 1991.
- Kruer W.L., *The physics of laser plasma interactions*, Addison-Wesley, 1988.
- Lee M. C. and S.P. Kuo, Excitation of upper-hybrid waves by a thermal parametric instability, *J. Plasma Phys.*, *30*, 463, 1983.
- Leyser, T.B., B. Thidé, H. Derblom, A. Hedberg and B. Lundborg, Stimulated electromagnetic emission near electron cyclotron harmonics in the ionosphere, *Phys. Rev. Lett.*, *63*, 1145, 1989.
- Leyser, T.B., B. Thidé, M. Wadenvik, E. Veszelei, V.L. Frolov, S.M. Grach and G.P. Komrakov, Down-shifted maximum features in stimulated electromagnetic spectra, *J. Geophys. Res.*, *99*, 19555, 1994.
- Mjølhus, E., A. Hanssen, and D.F. DuBois, Radiation from electromagnetically driven Langmuir turbulence, *J. Geophys. Res.*, *100*, 17527, 1995.
- Murtaza, G. and P.K Shukla, Nonlinear generation of electromagnetic waves in a magnetoplasma, *J. Plasma Phys.*, *31*, 423, 1984.
- Nicholson D.R., *Introduction to plasma theory*, John Wiley & Sons, 1983.

- Perkins, F. W., C. Oberman, and E. J. Valeo, Parametric instabilities and ionospheric modification, *J. Geophys. Res.*, *79*, 1478, 1974.
- Porkolab, M., Parametric instabilities in a magnetic field and possible applications to heating of plasmas, *J. Nuclear fusion*, *12*, 329, 1972.
- Rönnmark K., Computation of dielectric tensor of a Maxwellian plasma, *Plasma Phys.*, *25*, 699, 1983.
- Scales, W.A., K.T. Cheng and S. Srivastava, Simulation studies of processes associated with stimulated electromagnetic emission in the ionosphere, *J. Atmos. Terr. Phys.*, in press, 1996.
- Stenflo, L. and P.K. Shukla, Generation of radiation by upper-hybrid waves in non-uniform plasmas, *Planet. Space Sci.*, *40*, 473, 1992.
- Stix T.X., *Waves in plasmas*, American Institute of Physics, 1992.
- Stubbe, P., H. Hopka, B. Thidé, and H. Derblom, Stimulated electromagnetic emission: A new technique to study the parametric decay instability in the ionosphere, *J. Geophys. Res.*, *89*, 7523, 1984.
- Stubbe, P., A. Stocker, F. Honary, T.R. Robinson and T.B. Jones, Stimulated electromagnetic emissions and anomalous hf wave absorption near electron gyroharmonics, *J. Geophys. Res.*, *99*, 6233, 1994.
- Thidé B. and A. Hedberg *First observations of stimulated electromagnetic emission at Arecibo*, *Geophys. Res. Lett.*, *16*, 369, 1989.
- Thidé, B., H. Kopka and P. Stubbe, Observations of stimulated scattering of a strong high frequency radio wave in the ionosphere, *Phys. Rev. Lett.*, *49*, 1561, 1982.
- Zhou, H.L., J. Huang and S.P. Kuo, Cascading of upper hybrid/electron Bernstein wave in the ionospheric heating experiments, *Phys. Plasmas*, *1*, 3044, 1994.

Vita

Ahmed Hussein was born in Radford, Virginia in 1969. In 1972 he went back to his mother land, Egypt where he got his B.Sc in Electronics and Telecommunications Engineering with a distinction with honor grade (July 1991). In October 1991, he joined the M.Sc program at the same university and completed his M.Sc course work in May 1992 as first in class. Following the M.Sc course work he joined the computer networks group at the Electronics Research Institute and continued his M.Sc research work in the area of integration of voice and data in TCP/IP local environments. During the same time he joined the software development team at IBM corporation as a part time software programmer where he helped develop and test the SearchManager/360 client server software package. In December 1993 he was accepted as a Ph.D student at Virginia Tech where he was privileged to work under the supervision of Dr. Wayne Scales in the area of numerical simulation of ionospheric propagation phenomenon. Ahmed's areas of interest are electromagnetics, radio wave propagation, plasma physics, numerical techniques, telecommunications, simulation and modeling.